

POLITECNICO DI TORINO

Dottorato di Ricerca in Ingegneria Elettronica e delle Comunicazioni
XXVI Ciclo

Ph. D. Thesis

**X-band mini weather radar network
and other wireless sensor networks
for environmental monitoring**



Supervisor

Dr. Riccardo Notarpietro

Ph. D. Student:

Silvano Bertoldo

Co-supervisor

Prof. Giovanni Perona

Acknowledgments

Thanks to Andrea, Andrea, Claudio, Davide, Eliana, Emilia, Giampaolo, Giusy, Giovanni, Jury, Lorenzo, Lorenzo, Manuela, Marco, Marco, Marco, Riccardo, Oscar, Paolo, Sajid, Saverio, Stefano, Stefano.

Thanks to Mamma, Papà, Alessandra.

Thanks to Giosiana.

Table of Contents

Table of figures	pag. 4
Acronyms	pag. 11
Abstract	pag. 13
Introduction	pag. 14
PART 1	pag. 17
1. Rainfall measurement and radar meteorology	pag. 18
1.1 Different tools to monitor and measure rain	pag. 18
1.1.1 Rain gauges networks	19
1.1.2 Long range radars	21
1.1.3 Short range radars	24
1.1.4 Satellites	25
1.2 Radar meteorology	pag. 30
2. The X-band mini weather radar network	pag. 33
2.1 The X-band mini weather radar description	pag. 33
2.1.1 Technical description of X-band mini weather radar components	36
2.2 The radar constant	pag. 42
2.2.1 Radar constant evaluation	43
2.3 X-band mini weather radar signal processing	pag. 45
2.3.1 Standard signal processing at machine level	45
2.3.2 Standard signal processing at server level	49
2.3.1 Advanced signal processing at machine level	50
2.4 The meteoradar network	pag. 58
2.4.1 The meteoradar FTP archive	58
2.4.2 Radar map name	58
2.4.3 The database of the meteoradar network	59
2.4.4 The meteoradar network services	62
2.4.5 Free Android© App	63
3. Use of ground clutter echoes to monitor the X-band mini weather radar stability	pag. 64
3.1 Clutter definitions	pag. 64
3.1.1 Surface clutter	65

Table of Contents

3.1.2	<i>Volume clutter</i>	67
3.1.3	<i>Clutter for X-band mini weather radar</i>	67
3.2	Use of Ground Clutter Echoes to monitor the radar stability	pag. 68
3.2.1	<i>RCA (Relative Calibration Adjustment) Algorithm</i>	69
3.2.2	<i>X-band mini weather radar ground clutter echoes</i>	71
3.3	Definition of indicators to control the X-band mini weather radar stability	pag. 72
	and experimental results	
3.3.1	<i>Evaluation of different indicators</i>	73
3.3.2	<i>More detailed analysis on clutter maps and characterization of the radar receiver filter using ground clutter echoes</i>	76
3.4	A standalone application to monitor the radar stability using ground clutter echoes	pag. 83
3.4.1	<i>Clutter maps acquisition module</i>	84
3.4.2	<i>Processing module</i>	84
4.	Quantitative Precipitation Estimation (QPE)	pag. 86
4.1	Introduction to QPE	pag. 86
4.2	QPE with radars installed in Sicily Region	pag. 88
4.2.1	<i>QPE evaluation based on the comparison between hourly radar and gauge rainfall amounts</i>	88
4.2.2	<i>QPE for the Palermo radar</i>	89
4.2.3	<i>Wet versus dry hours discrimination according to radar echoes using the gauge as reference</i>	92
4.2.4	<i>QPE for the Bisacquino (PA) radar</i>	93
4.2.5	<i>QPE Summary in terms of Bias and Scatter in dB for Palermo and Bisacquino (PA)</i>	96
4.3	QPE with radar installed in Turin	pag. 97
4.3.1	<i>CALibration and VALidation procedure (CAL/VAL)</i>	98
4.3.2	<i>CAL/VAL procedure results</i>	100
4.4	Some conclusion about QPE	pag. 103
5.	Use of X-band mini weather radar: qualitative case studies	pag. 104
5.1	Detecting precipitation inside narrow valley	pag. 104
5.2	Detecting extreme rainfall events	pag. 108
5.3	Detecting rain fields in rapid movement	pag. 111
PART 2		pag. 113
6.	DGPS Wireless Sensor Network for landslide monitoring	pag. 114

Table of Contents

6.1 Introduction	pag. 114
6.2 Landslides monitoring phases	pag. 114
6.3 WSN description	pag. 119
6.3.1 General description	119
6.3.2 Electronic board hardware description	120
6.3.3 PC to control the network and process data	124
6.3.4 Remote server	125
6.4 Firmware and software implementation	pag. 126
6.4.1 General WSN firmware description	126
6.4.2 Control PC: software to control the WSN, receive and store data	129
6.5 Implemented services and to the data on the remote server	pag. 131
6.6 Test results	pag. 134
6.6.1 Experimental installation	134
6.6.2 Coordinates systems	137
6.6.3 Results	138
6.6.4 Conclusions	140
7. Other application of Wireless Sensor Networks	pag. 141
7.1 WSN as anti theft alarm system for photovoltaic panel	pag. 141
7.1.1 WSN general description	142
7.1.2 WSN designed hardware	143
7.1.3 Ad-hoc communication protocol	146
7.1.4 Alarm detection procedure	149
7.1.5 Processing software on the control PC	149
7.1.6 Sensors calibration	151
7.2 WSN for smart gas metering	pag. 152
7.2.1 General description of the grid for smart gas metering	153
7.2.2 Sensor node description	154
7.2.3 Reading pulses from gas meter equipments	156
7.2.4 Storing pulse on local memory	156
7.2.5 The communication protocol	156
7.2.6 Error handling	158
7.2.7 Central node description	158
7.2.8 Test results	161
7.2.9 Simulation of the network operational behavior	163
Bibliography	pag. 167

List of figures and tables

Introduction

Figures

Figure I.	Institutions, companies, partners involved during the Ph. D. program.	pag. 16
-----------	-----------------------------------------------------------------------	---------

Chapter 1

Figures

Figure 1.1	The ARPA Piemonte rain gauges network (Italy).	pag. 20
Figure 1.2	The SIAS rain gauges network (Italy).	21
Figure 1.3	NEXRAD (USA).	23
Figure 1.4	The radar network of MeteoSwiss (Switzerland).	23
Figure 1.5	The Canadian Weather radar network (Canada).	24
Figure 1.6	TRMM instrumentation.	26
Figure 1.7	Example of TRMM satellite image.	27
Figure 1.8	GPM satellite constellation.	28
Figure 1.9	Example of Meteosat 0 degree Visualised Products Multi-Sensor Precipitation Estimate (EUMETSAT, http://oiswww.eumetsat.org/IPPS/html/MSG/PRODUCTS/MPE).	30

Chapter 2

Figures

Figure 2.1	X-band mini weather radar	pag. 33
Figure 2.2	Basic block radar diagram.	35
Figure 2.3	Flexy waveguide.	37
Figure 2.4	Spectrum analyzer screenshot.	38
Figure 2.5	Horizontal plane radiation pattern measured by GIOMAR s.p.a. and plotted using MATLAB®.	40
Figure 2.6	Vertical plane radiation pattern measured by GIOMAR s.p.a. and plotted using MATLAB®.	41
Figure 2.7	Flow diagram of the radar signal processing strategy on the radar control pc.	45
Figure 2.8	Example of grayscale .png images acquired by the radar installed	48

	in Turin in clear sky days without clutter filter (on the left) and by the radar installed in Palermo during a heavy rainfall event (on the right).	
Figure 2.9	Processing steps at server.	49
Figure 2.10	Example of radar configuration file.	50
Figure 2.11	Effect of the parameters clutter-f with respect to the standard signal processing operations.	51
Figure 2.12	Example of active radar web server. The example is related to the radar installation made together with the University of Palermo.	52
Figure 2.13	of clutter filter enabled and disabled. The maps are related to the radar installed in Turin.	52
Figure 2.14	Acquisition of polar maps with respect to the standard signal processing operations.	54
Figure 2.15	Example of polar map acquired by the advanced radar control software. The maps are related to the radar installed in Turin.	55
Figure 2.16	The meteoradar network with the pictures of the active installation (2014).	57
Figure 2.17	Example of FTP archive. It is possible to note different directory related radar directories to archive radar maps (highlighted in green), directories for elder maps (highlighted in blue) and working directories (not highlighted).	58
Figure 2.18	E/R scheme of the mini weather radar network database.	59
Figure 2.19	Example of instantaneous rain map.	62
Figure 2.20	Previous day cumulated rain.	63
Figure 2.21	Screenshot and logo of the Android© App Meteoradar-IT.	63

Tables

Table 2.1	X-band mini weather radar characteristics.	pag. 36
Table 2.2	Flexy waveguide characteristics.	37
Table 2.3	Antenna technical specifications.	38
Table 2.4	Parameters for radar constant evaluation.	43

Chapter 3

Figures

Figure 3.1	Example of Grazing Angle for space borne radar.	pag. 65
Figure 3.2	Grazing angle.	66

List of figures and tables

Figure 3.3	Different type of clutter for X-band mini weather radar.	67
Figure 3.4	Example of instantaneous clutter map observed by the Turin radar.	68
Figure 3.5	Comparison of two daily PDFs/CDFs from August 2003. The horizontal dashed line represents the 95th percentile of the CDFs. Failure of the CDF curves to converge at the upper percentiles of the reflectivity is an indication of a calibration shift (D. S. Silberstein, 2008).	70
Figure 3.6	Comparison of two daily PDFs/CDFs from October 2001. The horizontal dashed line represents the 95th percentile of the CDFs. Distinctly different meteorological conditions exist on the two dates displayed, yet the CDF curves converge at the upper percentiles of the reflectivity, indicative of stable radar calibration (D. S. Silberstein, 2008).	70
Figure 3.7	Example of clutter map acquired with the X-band mini radar installed in Turin and superimposed on a cartographic system.	72
Figure 3.8	CDF for different values of filter configuration code (on the left) and different statistical indicators (on the right).	75
Figure 3.9	DN of an example of Cartesian radar clutter map acquired by the radar in Turin.	77
Figure 3.10	Transformation in received power (dBm) of an example of Cartesian radar clutter maps acquired by the radar in Turin	77
Figure 3.11	Example of Cartesian radar clutter maps acquired by the radar in Turin compensated for the attenuation due to the distance.	78
Figure 3.12	Clutter areas for Turin radar in both polar and Cartesian radar map.	78
Figure 3.13	Variation of the clutter power 90th percentile indicator in function of the receiver filter code value. Urban/Hill/Mountainous Clutter types are shown using blue/red/green color codes.	80
Figure 3.14	CDFs for receiver filter code value from 160 to 210.	81
Figure 3.15	CDFs for receiver filter code value from 210 to 255.	81
Figure 3.16	Mean and median for different clutter types with respect to different encoder values.	82

Tables

Table 3.1	Clutter echoes power distribution for different types of clutter.	pag. 79
-----------	-------------------------------------------------------------------	---------

Chapter 4

Figures

Figure 4.1	Differences between rain gauges and radar.	pag. 87
Figure 4.2	Volume of the radar cell in function of the distance from the radar.	87
Figure 4.3	Digital Elevation Map of Sicily showing two different domains (pixel size is 90 m); the blue triangle shows the mini radar site next to Palermo down town. The red triangle shows the location of the most reasonable rain gauge in terms of range and radar visibility; this gauge (Altofonte, PA) has been used for the QPE evaluation.	90
Figure 4.4	Vertical section of the terrain profile from the Palermo radar site to the Altofonte (PA) gauge. The blue lines indicate the boundaries of the radar antenna HPBW.	91
Figure 4.5	Scatter plot of 48 hours with Altofonte gauge amounts larger or equal than 0.4 mm/h and the corresponding Palermo radar estimates. The scale is linear and the maximum value is set to 10 mm/h.	92
Figure 4.6	DEM of the western part of Sicily showing the Bisacquino (PA) radar site (red triangle) and the Giuliana (PA) rain gauge location (blue triangle).	93
Figure 4.7	Vertical section of the terrain profile from the Bisacquino (PA) radar site to the Giuliana (PA) gauge. The blue lines indicate the boundaries of the radar antenna HPBW.	94
Figure 4.8	Scatter plot of 37 hours with Giuliana (PA) gauge amounts larger or equal than 0.4 mm/h and the corresponding Bisacquino (PA) radar estimates. It is worth noting that in this case the maximum value of the linear scale for the scatter plot is 20 mm/h.	95
Figure 4.9	Example of a daily cumulated clutter map observed by the Turin radar with superimposed the positions of rain gauges used for the QPE analysis.	98
Figure 4.10	Rain cumulated related to 28th November 2012 BEFORE the application of the BA coefficient. Radar of Turin.	101
Figure 4.11	Rain cumulated related to 28th November 2012 AFTER the application of the BA coefficient. Radar of Turin.	101

List of figures and tables

Figure 4.12	Scatter plot BEFORE the application of the BA coefficient. Radar of Turin.	102
Figure 4.13	Scatter plot AFTER the application of the BA coefficient. Radar of Turin.	102

Tables

Table 4.1	Palermo radar coordinates.	pag. 90
Table 4.2	Contingency table between the Palermo radar estimates and the Altofonte (PA) rain gauge measurements.	93
Table 4.3	Bisacquino (PA) radar coordinates.	93
Table 4.4	Contingency table between the Bisacquino (PA) radar estimates and the Giuliana (PA) rain gauge measurements.	95
Table 4.5	QPE evaluation summary in terms of Bias for three mini-radar sites.	96
Table 4.6	QPE evaluation summary in terms of scatter for Palermo and Bisacquino (PA) radar.	97
Table 4.7	Turin radar coordinates.	97
Table 4.8	VAL results for the Turin case. For each gauge, statistical indicators before (first row) and after (second row) the Bulk Adjustment procedure are shown.	100
Table 4.9	Statistical indicators evaluated for VAL sub-sets.	103

Chapter 5

Figures

Figure 5.1	Digital Elevation Model of the North-Western part of Italy.	pag. 105
Figure 5.2	24-hour cumulative rainfall amounts in the western Alps as seen by the Swiss weather radar network (from 12 UTC of November 4 to 12 UTC of November 5, 2011).	106
Figure 5.3	24-hour cumulative rainfall amounts in the north-western part of Italy as seen by X-band mini weather radar located near the town of Aosta (from 12 UTC of November 4 to 12 UTC of November 5, 2011)	107
Figure 5.4	Hourly accumulated rain in Sicily, 11th February 2011.	108
Figure 5.5	Intense creep of water inside the town of Montelepre (PA).	110

Tables

Table 5.1	Hourly rain accumulation map between 4.00 CET to 9.00 UTC, 18th February 2011.	pag. 109
Table 5.2	Radar maps acquired by the radar in Palermo during the late afternoon of 18th February 2011.	111

Chapter 6

Figures

Figure 6.1	WSN multipurpose board.	pag. 115
Figure 6.2	Different elements of the system to monitor the landslides, which include also the WSN.	118
Figure 6.3	Star topology of the WSN for landslide monitoring.	119
Figure 6.4	Block diagram of the WSN board.	120
Figure 6.5	Accelerometer specifications (extract from datasheet).	122
Figure 6.6	Network transaction. Broadcast Inquiring.	127
Figure 6.7	Network transaction. Data Request.	127
Figure 6.8	Principle of real time operating system.	128
Figure 6.9	Time diagram of the activities of the remote server	132
Figure 6.10	Example of a landslide represented over a common cartographic system.	133
Figure 6.11	Graphs web page during the test phase.	133
Figure 6.12	Report page of the web site during the test phase.	134
Figure 6.13	Antenna of the permanent station FOND (the receiver is inside the building of Fondazione Montagna Sicura).	135
Figure 6.14	Experimental installation of the first GPS network node GP01.	136
Figure 6.15	Experimental installation of the first GPS network node GP02.	137
Figure 6.16	Relation between ECEF and ENU coordinates systems.	138
Figure 6.17	ECEF coordinates daily mean measurements: 3D-plot.	139

Tables

Table 6.1	Landslide monitoring phase, landslide threshold speeds and admitted failures of the WSN.	pag. 117
Table 6.2	RS232 cable length according to Texas Instruments	124
Table 6.3	Differences in the measurements of the baseline between two consecutive days.	138
Table 6.4	ECEF coordinates daily mean measurements.	139

Table 6.5	Difference between the mean values of two consecutive days.	140
-----------	-------------------------------------------------------------	-----

Chapter 7

Figures

Figure 7.1	Sensor board used in the WSN designed as anti-theft alarm system for PV Panel.	pag. 144
Figure 7.2	Example of a protocol transaction without alarm detection.	148
Figure 7.3	Example of a protocol transaction when a board detects an alarm.	148
Figure 7.4	Realized electronic board for gas smart grid nodes.	155
Figure 7.5	Example of common gas metering system. The black box is the commercial pulse transmitter which is connected to the sensor board of the smart grid shown in Figure 7.4	156
Figure 7.6	Example of web interface. It reports the information about each network node. In the reported situation node 5 is no longer connected to the smart grid.	160
Figure 7.7	Example of web interface. It reports the last information reported in the log file.	160
Figure 7.8	Entity-Relationship scheme for central node database.	161
Figure 7.9	Smart grid node during the massive stress test connected to commercial pulse generator which will be connected to the gas meter in a real application.	162

Tables

Table 7.1	WSN packet structure.	pag. 147
Table 7.2	Calibration procedure results for a test board: offset values	152
Table 7.3	Calibration procedure results for a test board: sensitivity values.	152
Table 7.4	Percentage of correctly received packets from each node and managed by the entire smart.	162
Table 7.5	Actions performed during the simulation of the WSN operational behavior.	163

List of Acronyms

3DRC	3D Research Corporation
ACK	Acknowledgment
AP	Access Point
ARPA	Azienda Regionale Protezione Ambientale
CDF	Cumulative Distribution Function
CINFAI	Consorzio Interuniversitario per la Fisica delle Atmosfere e delle Idrosfere
CNES	Centre National d'Études Spatiales
CW	Continuous Wave
DEM	Digital Elevation Model
DET	Department of Electronics and Telecommunications
DGPS	Differential Global Positioning System
DN	Digital Number
DPR	Dual-frequency Precipitation Radar
DSD	Drop Size Distribution
ECEF	Earth Centered Earth Fixed
ECM	Electronic Countermeasure
ENU	East - North - Up
EUMETSAT	Organization for the Exploitation of Meteorological Satellites
EST	Envisens Technologies s.r.l.
FAR	False Alarm Rate
FTP	File Transfer Protocol
GMI	Global Precipitation Measurement Microwave Imager
GNSS	Global Navigation Satellite System
GPM	Global Precipitation Measurement
GPRS	General Packet Radio Service
GPS	Global Positioning System
HPBW	Half Power Beam Width
ICT	Information and Communication Technology
IR	Infrared
ISRO	Indian Space Research Organization
LAN	Local Area Network
LDO	Low Drop Out

List of Acronyms

LOS	Line Of Sight
M-BUS	Meter Bus
MCU	Micro Controller Unit
MPE	Multi-sensors Precipitation Estimate
NOAA	National Oceanic and Atmospheric Administration
QPE	Quantitative Precipitation Estimation
PCB	Printed Circuit Board
PDF	Probability Distribution Function
POD	Probability Of Detection
PR	Precipitation Radar
PRF	Pulse Repetition Frequency
PRI	Pulse Repetition Interval
PV	Photovoltaic
RCA	Relative Calibration Adjustment
RCS	Radar Cross Section
RINEX	Receiver Independent Exchange Format
RSG	Remote Sensing Group
SIAS	Servizio Informativo Agrometeorologico Siciliano
SCR	Signal to Clutter Ratio
S-MODE	Stationary Mode
SNR	Signal to Noise Ratio
SSH	Secure Shell
TMI	TRMM Microwave Imager
TRMM	Tropical Rainfall Measuring Mission
UMTS	Universal Mobile Telecommunication System
WM-BUS	Wireless Meter Bus
WSN	Wireless Sensor Network

Abstract

The main section of the present Ph. D. thesis is related to X-band radars. Since 2005 the Remote Sensing Group of Department of Electronics and Telecommunications of Politecnico di Torino developed an X-band mini weather radar as a standalone sensor to measure rain. Some early results have been presented until 2011 showing the proper functioning and it has been decided to realize an experimental and operative integrated network of X-band radar devoted to rain measurement. The network structure deployed during the Ph. D. period is presented, together with the analysis, the study and the realizations of some operative services, calibration procedures (including Quantitative Precipitation Estimation, QPE) and software and applications developed for the institutions which support the network realizations.. The design of an innovative and low cost method to check the radar stability and proper functioning is presented: by simply acquiring a large number of ground clutter echoes during clear sky days and computing some analysis, it is shown it is possible to identify some statistical indicators that allow users and radar operators to know if the radar equipments suffered some degradations of failure.

The second part of the thesis is dedicated to Wireless Sensor Networks (WSNs). After a study on WSN technologies for environmental monitoring, a first developed prototypal DGPS network is presented. Using the same multipurpose node designed for such network (or its updated releases with very small differences) and varying only their firmware, other two prototypal and fully operative WSNs are described. The designed choices are described for what concern both hardware and software.

Introduction

The present Ph. D. thesis is the result of the Ph. D. works and researches made with the Remote Sensing Group (RSG) of the Department of Electronics and Telecommunications (DET) at Politecnico di Torino and Envisens Technologies s.r.l. spinoff of Politecnico di Torino.

The work is divided in two main parts: the first is related to a mini weather radar network realizations and to the improvement of the functionalities of the mini weather radars. The second is related to Wireless Sensor Networks (WSNs), with particular focus to WSNs for environmental monitoring. Both the activities are basically devoted to environmental monitoring and protection.

The frequency of high intensity rainfall events is steadily increasing in the Mediterranean area and specially in the hilly and mountainous parts of Italy and they may cause floods (even within a very short time, the so called *flash floods*) and landslides. In these situations, to efficiently monitor rivers flow, floods and landslides an unrealistic extremely dense rain gauge network should be needed, due to the nature of the localized rain events of limited extension and the size of the river basins of interest. In this context the short range radar network described in this work is a good and useful solution to improve the environmental protection. It can also be used as a support for farmers who need to know the amount of water fallen and for civil protection purposes in urban areas. The **Chapters form 1 to 5** are all devoted to the

analysis, the studies, and the presentations of new tools and algorithms related to the mini weather radars.

The monitoring of landslides and glaciers have been always a hard task for people devoted to environmental monitoring because it is necessary to work in harsh environment and often with extreme weather conditions. The standard equipments needed for monitoring operation are often too expensive. This thesis presents a simple low cost DGPS network which has been realized as a tool to monitor landslide (**Chapter 6**).

In order to reduce the overall cost, the DGPS network basic electronic board have been realized as a multipurpose board. **Chapter 7** presents two other WSNs developed with the same multipurpose board (and with its evolution with reduces sizes) but for completely different purposes: a WSN as antitheft alarm system and a WSN as a smart gas meter system. These two networks are realized by only varying the firmware of the nodes of the network and using different sensors with respect to the WSN devoted to landslide monitoring, but the electronic boards is the same.

All the activities related to weather radar and rainfall estimation are part of the main project of the Ph. D. program, called “Monitoraggio Radar Ambientale”, which is part of a cooperative program co-founded by Regione Piemonte called “Alta Sperimentazione in Apprendistato” which include some co-founded Ph. D. program.

Aim of the program is mainly twofold:

- to offer to the Ph. D student the possibility to work with high level technologies offered by a company.
- to attend high level formation activities offered from both Politecnico di Torino and also from other institutions, thanks to additional funds provided by Regione Piemonte.

The present work has been made in collaboration with Envisens Technologies s.r.l. (EST). EST has been established in 2006 as a spin-off of Politecnico di Torino and inherit experience in academic and applied research of the RSG leaded by Prof. Giovanni Perona at Politecnico di Torino. EST operates in innovative technological solution engineering in the framework of environmental and safety applications, with

particular focus on sensors and simulations, including prototyping, paying attention to low cost solutions and multipurpose electronic realizations. The Ph. D. activities are completely identified within the company profile.

All the activities have been made within different research projects with both EST and Politecnico di Torino and other different partners as:

- CINFAI (Consorzio Interuniversitario Nazionale per la Fisica delle Atmosfere e delle Idrosfere);
- Protezione Civile della Provincia Regionale di Palermo, Italy;
- CRA (Consiglio per la Ricerca e la Sperimentazione in Agricoltura), Italy;
- Department of Geography Hebrew University of Jerusalem, Israel;
- ANKENERGIA s.r.l., Italy;
- Piceno GAS s.r.l., Italy;



Figure I. Institutions, companies, partners involved during the Ph. D. program.

PART 1

X band mini weather radar network

1.

Rainfall measurement and radar meteorology

1.1 Different tools to monitor and measure rain

Accurate observation of precipitations in terms of intensity and location is important for many applications: hydro-geological risk management, hydroelectric power, road maintenance, emergency planning, and tourism are only some examples of a wider number of fields.

The most traditional method of measuring and observing rainfall using rain gauges is the less expensive but only provides punctual measurements on the ground. Other instruments such as disdrometers and microwave links provide more insight in the microstructure and the spatial average of precipitation. However, these instruments cannot capture the spatial variability of rainfall over large areas such as river catchments. Moreover they are too specific and they cannot be used by simple technicians and operators of institution responsible for environmental monitoring and natural hazard prevention, like for instance, Civil Protection volunteers, who often do not have the required skills to use them.

Most common C-band and S-band long range radar systems can offer an immediate way for measuring precipitation over a certain area but often their time and space resolutions are poor, especially if they are used over complex orography regions where their beam are often partially shielded by relieves, and where their performance

must often be improved by some post processing techniques and long training period. X-band mini radar systems are proposed as a solution to monitor and observe rain events with a good resolution in space and time at, last but not least, low costs. They can be used standalone to monitoring and observing rainfall events as well as they can be a useful integration for already existing network devoted to monitoring rain.

1.1.1 Rain gauge networks

Direct measurement of rainfall at ground level can only be achieved using the common rain-gauges. However, even if modern rain-gauges are capable of providing rainfall rate in real time and with very high resolution in time, the spatial variability of rainfall is still difficult to characterize^{1,2}.

Two major factors determine the evaluation and design of a rain gauge network: the density and locations of the rain-gauges. The choices depend on the dominant rain types and the goals to be achieved with the network. Just as an example, for flood mitigation purposes, which is the most required aim by institutions responsible for natural hazard prevention, the interpolation of rainfall at locations where no gauge is present is needed. A high density network is therefore necessary in order to perform a good interpolation. For water resources planning, instead, a low density rain-gauge network can be enough to observe long duration rainfall events.

The design of an efficient rain gauge network becomes more difficult in complex orography regions. Such environments are in fact characterized by high spatial variability of physical parameters, hard environmental and weather conditions: placing a rain gauge within a small distance from another cannot be sufficient to control a specific area: distances of few hundreds of meters may mean changing valley.

Many approaches to optimal selection of rainfall gauges taking into account their number and their location to yield greater accuracy of areal rainfall estimation have

¹ G. J. Ciach, *Local random errors in tipping-bucket rain gauge measurements*, Journal of Atmospheric and Oceanic Technology, Vol. 20, No. 5, 2003, pp. 752 – 759.

² G. J. Ciach and W. F. Krajewski, *Analysis and modeling of spatial correlation structure of small scale rainfall in Central Oklahoma*, Advances in Water Resources, Vol. 29, No. 10, 2006, pp. 1450 – 1463

been proposed in the scientific literature³. However each of them obviously requires the placement of a certain number of instruments and the realization of a rain gauge network could be very expensive.

Last but not least even with a well designed rain gauge network, no areal rainfall measurements are provided without a post processing algorithm to interpolate data. Interpolation does not always provide for sufficiently precise rainfall areal values.

Two examples of rain gauges network used in the present work are:

- The rain gauge network of ARPA (Azienda Regionale per la Protezione Ambientale) Piemonte, in Piedmont, Italy.



Figure 1.1 The ARPA Piemonte rain gauges network (Italy).

- The rain Gauge network provided by SIAS (Servizio Informativo Agrometeorologico Siciliano), in Sicily, Italy.

³ K.-S. Cheng, Y.-C. Lin and J.-J. Liou, *Rain-gauge network evaluation and augmentation using geostatistics*, Hydrological Processes, Vol. 22, No. 14, 2008, pp. 2554 – 2564.

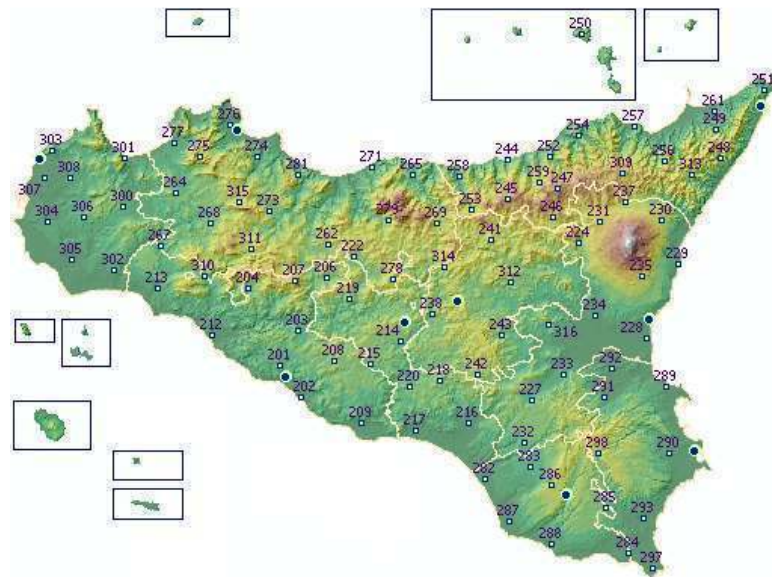


Figure 1.2 The SIAS rain gauges network (Italy).

1.1.2 Long range radars

It is also possible to estimate rainfall amount and observe rain events evolution using long range ground based radars.

However radar systems can see the hydrometeors aloft, while we would need to know what is arriving at ground level. They give a measure of the amount of water presents inside a volume above a projected area at ground level. Obstacles, as well as earth curvature, lead to a limited horizon, allowing to see precipitation at variable height, often too far from the ground. All these difficulties increase rapidly with range from the radar location. The situation becomes obviously much more difficult in mountainous terrain, where weather echoes can only be detected at high altitudes because of beam shielding by relieves: terrain blockage combined with the small amount of precipitation during cold seasons causes inadequate radar coverage to measure precipitations especially in narrow valleys⁴.

⁴ M. Gabella and G. Perona, *Simulation of the orographic influence on weather radar using a geometric-optics approach*, Journal of Atmospheric and Oceanic Technology, Vol. 15, 1998, pp. 1485 – 1494.

The agreement between radar and surface precipitation estimates generally decrease with increasing radar range⁵. Increasing radar sampling volume and the height of the radar beam above the ground at far ranges may increase the probability that precipitation observed aloft (which may be made by snow, ice, rain drops...), is different from the one reaching the ground. This is due to evaporation, advection and vertical air motion.

Furthermore it has to be consider that precipitation is often too variable for the “coarse” resolution of long-range radars. The spatial variability of natural precipitation is so large that the radar beam is not always capable to resolve it. The under-sampling problem become increasingly severe with increasing ranges because the radar backscattering volume increases with the square of the range; therefore, at greater ranges, small but intense features of the precipitation system are blurred. This problem is known as “non-homogeneous beam filling”. Some studies confirming the range dependence of long range radar behavior has been done using TRMM data^{6,7}.

At longer range another problem well known by radar meteorologist, tightly joined with the non homogeneous beam filling is the “beam overshooting”. It is due to the decrease of vertical resolution with range and by the variability of the particles that filled the pulse, thus amplifying the influence of the horizon and Earth’s curvature. It may cause no back scattering echoes even in presence of precipitation.

When very high temporal resolution is required long range radars cannot be used. In fact the time interval between map production is often too large for real time monitoring operation. Common interval of 5 minutes could be not enough to observe and track the movements of very fast rainfall cells. It is not possible to significantly

⁵ J. W. Wilson and E. A. Brandles, *Radar measurement of rainfall – A summary*, Bulletin American Meteorological Society, Vol. 60, No. 9, 1979, pp. 1048 – 1078.

⁶M. Gabella, J. Joss, S. Michaelides and G. Perona, *Range adjustment for ground-based radar, derived with the spaceborne TRMM precipitation radar*, IEEE Transaction on Geosciences and Remote Sensing, Vol. 44, No. 1, 2006, pp. 126 – 133.

⁷M. Gabella, E. Morin, R. and R. Notarpietro, *Using TRMM spaceborne radar as a reference for compensating ground-based radar range degradation: methodology verification based on rain gauges in Israel*, Journal of Geophysical Research, Vol. 16, D02144, 2011.

shorten this time because of the large observation area and the relative long time of computing and antenna motion.

Some examples of famous long weather radar network are the following:

- NEXRAD: the USA radar network



Figure 1.3. NEXRAD (USA).

- The radar network of MeteoSwiss

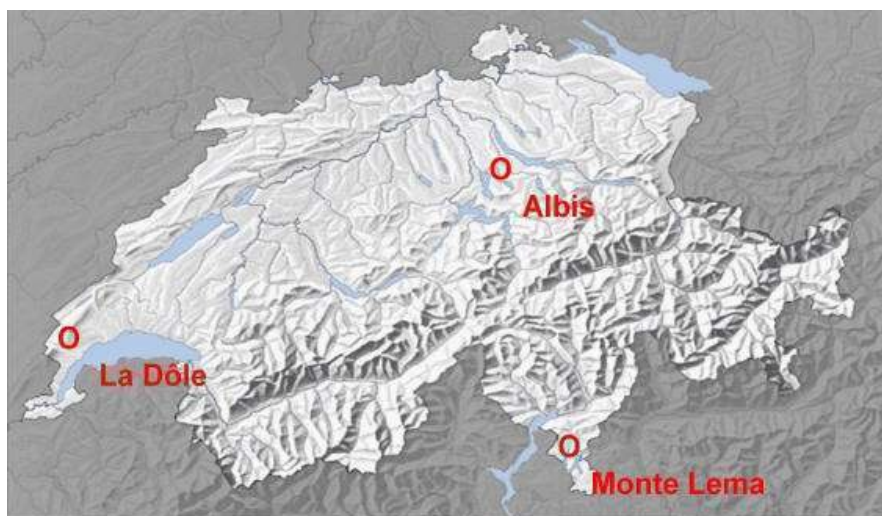


Figure 1.4. The radar network of MeteoSwiss (Switzerland).

1.1.4 Satellite

1.1.4.1 Experimental mission TRMM⁸

The Tropical Rainfall Measuring Mission (TRMM) is a joint mission between NASA and the Japan Aerospace Exploration Agency (JAXA) designed to measure rainfall for weather and climate research.

TRMM is a research satellite designed to improve our understanding of the distribution and variability of precipitation within the tropics as part of the water cycle in the current climate system. By covering the tropical and sub-tropical regions of the Earth, TRMM provides much needed information on rainfall and its associated heat release that helps to power the global atmospheric circulation that shapes both weather and climate. In coordination with other satellites in NASA's Earth Observing System, TRMM provides important precipitation information using several space-borne instruments to increase our understanding of the interactions between water vapor, clouds, and precipitation, that are central to regulating Earth's climate.

One of the great challenges facing mankind in the 21st century is the threat of global climate change due to increased levels of carbon dioxide and other greenhouse gasses in the atmosphere. The energy balance of the global atmosphere shows that only about one fourth of the energy needed to drive the global atmospheric circulation comes from direct solar energy. The other three fourths of the energy is transferred to the atmosphere by evaporating water - mainly from the ocean. As the water vapor rises from the surface, it carries with it the energy it takes to turn liquid water into water vapor - the "Latent Heat of Evaporation". Most of this latent heat is released into the atmosphere in huge equatorial cloud clusters when the vapor condenses to form cloud- and raindrops. The latent heat energy contained in the clouds cannot be seen or measured directly. Rainfall, however, is the product of the release of this energy, and rainfall can be measured. Responsible for three quarters of the energy that drives the global atmospheric circulation, tropical rainfall can be said to drive the 'Climate Machine.' Unfortunately, there are still uncertainties of as high as 50% in the amount of tropical rainfall. Unless we can better define the amount of rainfall and the energy

⁸ <http://trmm.gsfc.nasa.gov/>

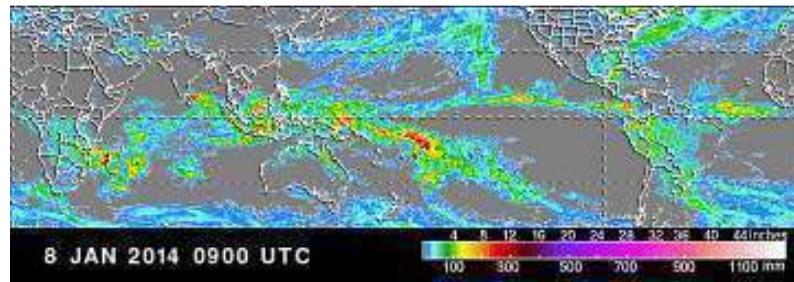


Figure 1.7. Example of TRMM satellite image

1.1.4.2 Experimental mission GPM⁹

The Global Precipitation Measurement (GPM) mission is an international network of satellites that provide the next-generation global observations of rain and snow.

Building upon the success of the Tropical Rainfall Measuring Mission, the GPM concept centers on the deployment of a “Core” satellite carrying an advanced radar / radiometer system to measure precipitation from space and serve as a reference standard to unify precipitation measurements from a constellation of research and operational satellites. Through improved measurements of precipitation globally, the GPM mission will help to advance our understanding of Earth's water and energy cycle, improve forecasting of extreme events that cause natural hazards and disasters, and extend current capabilities in using accurate and timely information of precipitation to directly benefit society. GPM, initiated by NASA and the Japan Aerospace Exploration Agency (JAXA) as a global successor to TRMM, comprises a consortium of international space agencies, including the Centre National d'Études Spatiales (CNES), the Indian Space Research Organization (ISRO), the National Oceanic and Atmospheric Administration (NOAA), the European Organization for the Exploitation of Meteorological Satellites (EUMETSAT), and others. The GPM Core Observatory is scheduled for launch this year, in early 2014.

The GPM Core Observatory design is an extension of TRMM's highly successful rain-sensing package, which focused primarily on heavy to moderate rain over tropical and subtropical oceans. Since light rain and falling snow account for significant fractions of precipitation occurrences in middle and high latitudes, a key

⁹ <http://pmm.nasa.gov/GPM>

advancement of GPM over TRMM is the extended capability to measure light rain (< 0.5 mm hr⁻¹), solid precipitation and the microphysical properties of precipitating particles. This capability drives the designs of both the active and passive microwave instruments on GPM. The Core Observatory will then act as a reference standard for the precipitation estimates acquired by the GPM constellation of sensors.

The GPM Core Observatory will carry the first space-borne Ku/Ka-band Dual-frequency Precipitation Radar (DPR) and a multi-channel GPM Microwave Imager (GMI). The DPR instrument, which will provide three dimensional measurements of precipitation structure over 78 and 152 mile (125 and 245 km) swaths, consists of a Ka-band precipitation radar (KaPR) operating at 35.5 GHz and a Ku-band precipitation radar (KuPR) operating at 13.6 GHz. Relative to the TRMM precipitation radar, the DPR is more sensitive to light rain rates and snowfall. In addition, simultaneous measurements by the overlapping of Ka/Ku-bands of the DPR can provide new information on particle drop size distributions over moderate precipitation intensities. In addition, by providing new microphysical measurements from the DPR to complement cloud and aerosol observations, GPM is expected to provide further insights into how precipitation processes may be affected by human activities.

The GMI instrument is a conical-scanning multi-channel microwave radiometer covering a swath of 550 miles (885 km) with thirteen channels ranging in frequency from 10 GHz to 183 GHz. The GMI uses a set of frequencies that have been optimized over the past two decades to retrieve heavy, moderate and light precipitation using the polarization difference at each channel as an indicator of the optical thickness and water content.



Figure 1.8. GPM satellite constellation.

1.1.4.3 Multi-sensor Precipitation Estimation from Satellite

The Multi-sensor Precipitation Estimate (MPE) from satellite is an instantaneous rain rate product which is derived from the IR-data of the geo-stationary satellites by continuous re-calibration of the algorithm with rain-rate data from polar orbiting microwave sensors.

In principle the MPE techniques can be applied when different type of sensors cooperate together in order to obtain a good Quantitative Precipitation Estimation (QPE). A detailed analysis of QPE though MPE techniques is not reported here but there are a lot of papers in the scientific landscape documenting that. However it is important to point out that there are meteorological satellites that use MPE to give a rain estimation as an operational service (e.g. provided by EUMETSAT¹⁰), which is different from the experimental mission TRMM and GPM briefly described above.

¹⁰ <http://www.eumetsat.int/website/home/index.html>

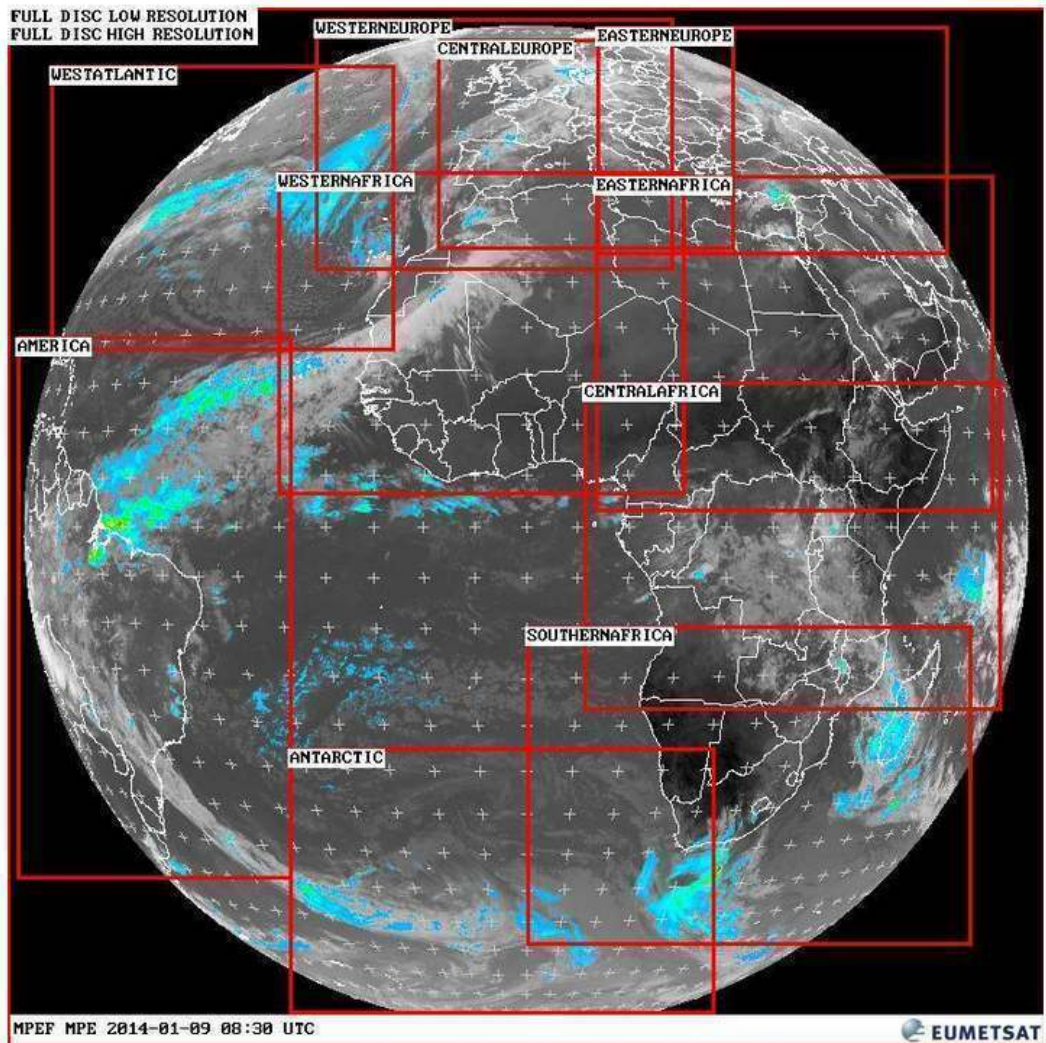


Figure 1.9. Example of Meteosat 0 degree Visualised Products Multi-Sensor Precipitation Estimate (EUMETSAT, <http://oiswww.eumetsat.org/IPPS/html/MSG/PRODUCTS/MPE>).

1.2 Radar meteorology

Since most of the following chapters are related to short range X-band radar, it is important to briefly point out how it is possible to measure the rain using an instrument that was originally invented to detect object in the space.

The backscattered power caused by rain drops is, unfortunately, only indirectly linked to the rain rate, R ($[R] = \text{mm/h}$). The backscattered power caused by the hydrometeors and detected by the radar is, in fact, directly proportional to the radar reflectivity factor, Z . A fundamental quantity for precise assessment of both Z and R is

the Drop Size Distribution (DSD), $N(D)$, which is defined as the number of rain drops per unit volume in the diameter interval δD , i.e. between the diameter D and $D+\delta D$. The radar reflectivity factor, Z , is defined as the 6th moment of the DSD, namely:

$$Z = \int_0^{\infty} N(D)D^6 dD \quad (\text{eqn. 1.1})$$

In radar meteorology, it is common to use the dimensions of mm for drop diameter, D , and to consider the summation (integral) to take place over a unit volume of 1 m^3 . Therefore, the conventional unit of Z is in mm^6/m^3 . For the assessment of rain rate, another fundamental quantity is needed: the terminal drops fall velocity as a function of the diameter, $v(D)$. Since it is common to use $[v] = \text{m/s}$, then the relationship is:

$$R = 6 \cdot 10^{-4} \cdot \pi \int_0^{\infty} N(D)D^3 v(D) dD \quad (\text{eqn. 1.2})$$

If precipitating hydrometeors in the radar backscattering volume were all spherical raindrops (which is to note that is almost never the real case) and the DSD could be described to a good approximation by an exponential DSD, then a simple power-law would relate Z to R .

The first ever exponential DSD presented in a peer-reviewed paper and probably the most quoted is the Marshall – Palmer (M-P) distribution. The power law derived using the exponential fit proposed in the famous paper by Marshall and Palmer¹¹ in 1948 is:

$$Z=296 \cdot R^{1.47} \quad (\text{eqn. 1.3})$$

Considering the equation 1.3, the radar reflectivity Z is related to the rainfall amount R with a simple power law such as $Z=aR^b$, where a and b are numerical coefficient chosen on the basis of empirical experiments and analytic studies.

¹¹J. S. Marshall and W. M. Palmer, *The distribution of raindrops with size*, Journal of Meteorology, Vol. 5, pp. 165 – 166, 1948.

Quantitative Precipitation Estimation using radars is difficult because of different types of rain and different climatic conditions and the possible choices of such a and b coefficients is a hard task. To have an idea, 69 different Z - R relationships are discussed in a book of 1973¹².

For instance, Rosenfeld¹³ in 1993 proposed the equation with $a=250$ and $b=1.2$; it was initially proposed for tropical rain but it is usable also for intense and persistent rain not only in tropical regions.

In Italy it is usually used to use the following Z - R relationship to derive the variable of interest, R , from the geophysical observable, Z , which is detected by the meteorological radar:

$$Z = 316 \cdot R^{1.5} \quad (\text{eqn. 1.4})$$

Such values have been retrieved by Doelling¹⁴ et al. using seven years of measurements in central Europe.

¹² L. J. Battan, *Radar Observation of the atmosphere*, University of Chicago Press, Chicago, 1973

¹³D. Rosenfeld, D. B. Wolff and D. Atlas, *General probability matched relations between radar reflectivity and rain rate*, Journal of Applied Meteorology, Vol. 32, No. 1, pp. 50 – 72, 1993.

¹⁴Doelling, I. G., J. Joss, and J. Riedl, *Systematic variations of Z-R relationships from drop size distributions measured in Northern Germany during seven years*, Atmospheric Research., Vol. 48, pp. 635-649, 1998

2.

The X-band mini weather radar and the meteoradar network

2.1 X-band mini weather radar description

X-band mini radars (**Figure 2.1**) have been designed by the Remote Sensing Group (RSG) of Polytechnic of Turin together with the a local unit of Consorzio Interuniversitario per la Fisica delle Atmosfere e delle Idrosfere, (CINFAI) and Envisens Technologies s.r.l. (EST).



Figure 2.1. X-band mini weather radar.

Their realization started from early ideation stages during the FORALPS (“Meteo-hydrological Forecast and Observations for improved water Resource management in the ALPS”) project in 2004. First important results are reported in a paper presented at a conference in 2005¹.

The first fully operational network of mini radar was set up in 2011 with the installations in Italy of 5 experimental mini radar, 4 of them in the Sicily Region² and one of them in the Aosta Valley. At the end of 2013 the network is made up of 8 radar systems: the first one was installed in Turin town (2010), one is installed in the Aosta Valley (2011), one near Foggia, in the South of Italy (2012), one in the town of Palermo in Sicily Region (2012), two in Israel in collaboration with the Hebrew University of Jerusalem (2012), one near Nizza Monferrato in Piedmont Region (2012) and one in Parma, North Italy (2013). The network will be described in details in the following with all its developed functionalities.

In recent years, X-band meteorological radar networks are beginning to appear in an even more massive way; see for example, the CASA radars, very well described in a recent review article published on Bulletin of the American Meteorological Society³, where an extensive bibliography concerning X-band radars and technologies is reported, or another recent work presented in ERAD 2010 by F. Marzano⁴.

¹ R. Notarpietro, M. Zambotto, M. Gabella, S. Turso and G. Perona, *The radar ombrometer: a portable, low-cost, short-range, X band radar for rain estimation within valleys*, VOLTAIRE final conference joint with the 7th European Conference on Application of Meteorology (ECAM7) and the European Meteorological Society Meeting (EMS05), Utrecht, The Netherlands, September 12th – 16th, 2005.

² S. Bertoldo, C. Lucianaz, O. Rorato, M. Allegretti, A. Prato, G. Perona, *An operative X-band mini radar network to monitor rainfall events with high time and space resolution*, Engineering, Technology & Applied Science Research, Vol. 2, No. 4, 2012, pp. 246-250, ISSN: 1792-8036.

³ D. McLaughlin, D. Pepyne, B. Philips, J. Kurose, M. Zink, D. Westbrook, E. Lyons, E. Knapp, A. Hopf, A. Defonzo, R. Contreras, T. Djaferis, E. Insanic, S. Frasier, V. Chandrasekar, F. Junyent, N. Bharadwaj, Y. Wang, Y. Liu, B. Dolan, K. Droegemeier, J. Brotzge, M. Xue, K. Kloesel, K. Brewster, F. Carr, S. Cruz-Pol, K. Hondl, P. Kollias, *Short-Wavelength Technology and the Potential For Distributed Networks of Small Radar Systems*, Bull. Am. Meteorol. Soc., Vol. 90, pp. 1797-1817, 2009.

⁴ Marzano F. S., Picciotti E., Cinque G., Montopoli M., Bernardini L. 1a, Giuliani G., Anagnostou E., Anagnostou M., Fessas Y., Volpi A., Telleschi A., Kalogiros J., Cazac V., Pace R., Sanna F., *HydroRad project: integrating X-band mini-radar networks and hydro-meteorological forecast models in Moldova territory*, ERAD 2010 - The sixth European conference on radar in meteorology and hydrology, Sibiu, Romania, September 6th - 10th 2010.

Each X-band mini weather radar developed by RSG of Polytechnic of Turin are certainly simpler: they are exclusively devoted to rain measurements, they are a low cost system and does not require special needs for installation. In particular, it does not require particular maintenance and the possibility to be remotely controlled with software updates, make such radar able to conveniently cover limited areas without dramatic impacts on the environment, and without the need of strong logistic support.

All the electronic equipments (antenna, radiofrequency unit, data processing unit, communication unit for data transmission and remote control, power unit) are placed inside the radome which is less than 2 m high and less than 1 m wide; it may be secured to any flat surface and it only needs to be connected to a power supply. All the software required to operate the dedicated applications is open source in order to allow a great reliability and flexibility in the configuration and full control of active processes and packages, as well as low costs.

The radar system is built by un-coherent pulsed non Doppler radar, exploiting only the vertical polarization. It transmits 400 ns pulses (PRF: 800 Hz) characterized by a peak power of 10 kW (maximum range was set to 30 km), and it is equipped with a fixed elevation parabolic antenna (34 dB gain, 3.6° Half Power Beam Width, HPBW) usually tilted of about 2.5° above the horizontal plane.

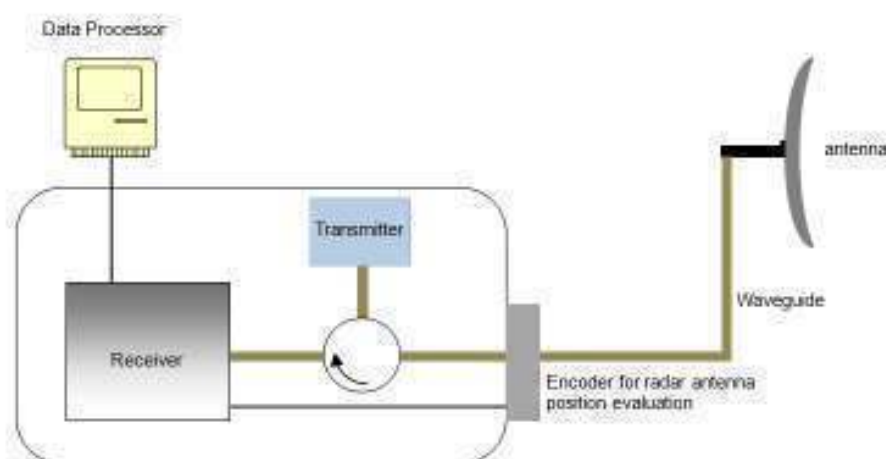


Figure 2.2. Basic block radar diagram.

The X-band radar is capable to produce an image map each 1 minute with a “virtual” resolution of 60 m within a range of 30 km. Obviously only the physical range resolution is of the same order (approximately 90 m) while the range resolution is much larger (at 30 Km range it is approximately 1500 m). The range of 30 km allows to avoid some problems connected with atmospheric effects obtaining more stable back scattering echoes. A series of anti-clutter filters are also applied in order to recover, as far as possible, rain signature even in presence of clutter.

The radar maps produced by the X band mini radar unit are transmitted to the server via a GPRS communication network (other communication systems are also allowed, if already present in the installation site). In the server, radar maps are managed by a specific processing software which allows to compute precipitation maps.

2.1.1 Technical description of X-band mini weather radar components

Table 2.1 reports the main characteristics of the X-band mini weather radar systems, while the following paragraphs reports some detailed descriptions of each component of the radar system, as shown in **Figure 2.2** are reported.

Table 2.1. X-band mini weather radar characteristics

Transmitter	
<i>Peak power</i>	10 kW
<i>Pulse length</i>	600 ns
<i>Transmitted frequency</i>	(9410 ± 30) MHz
<i>Pulse Repetition Frequency (PRF)</i>	800 Hz
<i>Modulator</i>	Solid state
Receiver	
<i>Receiver type</i>	Logarithmic, solid state
<i>Dynamic range</i>	From 0 to -100 dBm
<i>Intermediate Frequency (IF)</i>	60 MHz
<i>Receiver filter bandwidth</i>	(20 ± 2) MHz
Other specifications	
<i>Front end</i>	Microwave integrated circuit
<i>Noise figure</i>	< 3.5 dB
<i>Duplexer</i>	Ferrite circulator with state solid diode limiter
<i>Antenna rotation speed</i>	(22 ± 2) r. p. m.
<i>Power</i>	24 Vdc

2.1.1.1 Flexible waveguide description

The rotating joint (part of the RF generator) is connected to a flexible waveguide that introduce an additional loss of 0.3 dB.

Table 2.2. Flexy waveguide characteristics

<i>Waveguide type</i>	Flexy WR90
<i>Length</i>	1 m
<i>Waveguide losses</i>	0.3 dB



Figure 2.3. Flexy waveguide.

2.1.1.2 Waveguide transition

The waveguide chain ends with the WR90 – WR75 transition to match with the WR75 antenna flange. The total losses due to the entire waveguide chain (flexible waveguide plus transition) are equal to (0.4 ± 0.1) dB.

2.1.1.3 Magnetron characterization

The magnetron transmits at the frequency of about $9.410 \text{ GHz} \pm 30\text{MHz}$ due to the manufacturing process. The exact frequency is measured in laboratory and all frequency filters are tuned via software. Measurements made in laboratories shows that the magnetron frequency derive is about 150 KHz/K. It means that a $10 \text{ }^\circ\text{C}$ (or K) temperature variation change the magnetron frequency of 1.5 MHz.



Figure 2.4. Spectrum analyzer screenshot.

Some measurements have been performed in order to verify the stability of the magnetron. The radar has been turned on for two entire days, and a spectrum analyzer set in max hold has been used. In this way it was possible to note that the magnetron has a frequency drift of 1 MHz (Figure 2.4).

2.1.1.4 Antenna technical specifications

The radar is equipped with a parabolic antenna produced by GIOMAR, model GPH06.

Table 2.3. Antenna technical specifications

Diameter	60 cm
F/D	0.35
DEP	10.7 cm
Focal length	21 cm
Adjustment of polarization	360°
Material	Anodized aluminium
Thickness	3 mm
Setting of fine bearings on the horizontal plane	± 7°
Setting of fine bearings on the vertical plane	± 7°
Operational temperature	- 40 °C – 60 °C

The following figures represent the radiation pattern both in the horizontal plane and in vertical plane at the central frequency $f = 10.5$ GHz. In the mini weather applications the antenna is used at about 9.4 GHz, slightly off from the central band for which it was designed implying a reduction of the nominal gain reported on the technical specifications.

It is to note that the Half Power Beam Width of the antenna is 3.6° both in horizontal and in vertical plane.

2. The X-band mini weather radar and the meteoradar network

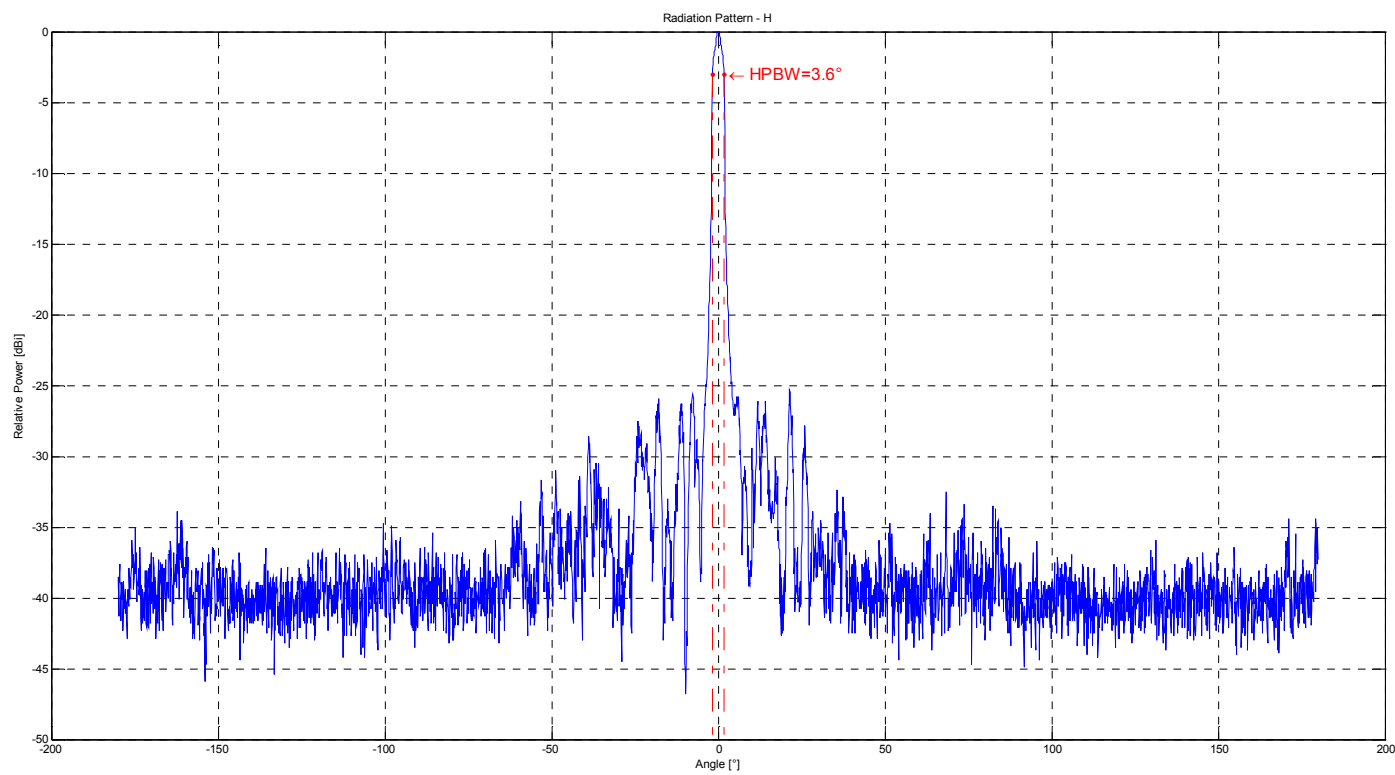


Figure 2.5. Horizontal plane radiation pattern measured by GIOMAR s.p.a. and plotted using MATLAB©.

2. The X-band mini weather radar and the meteoradar network

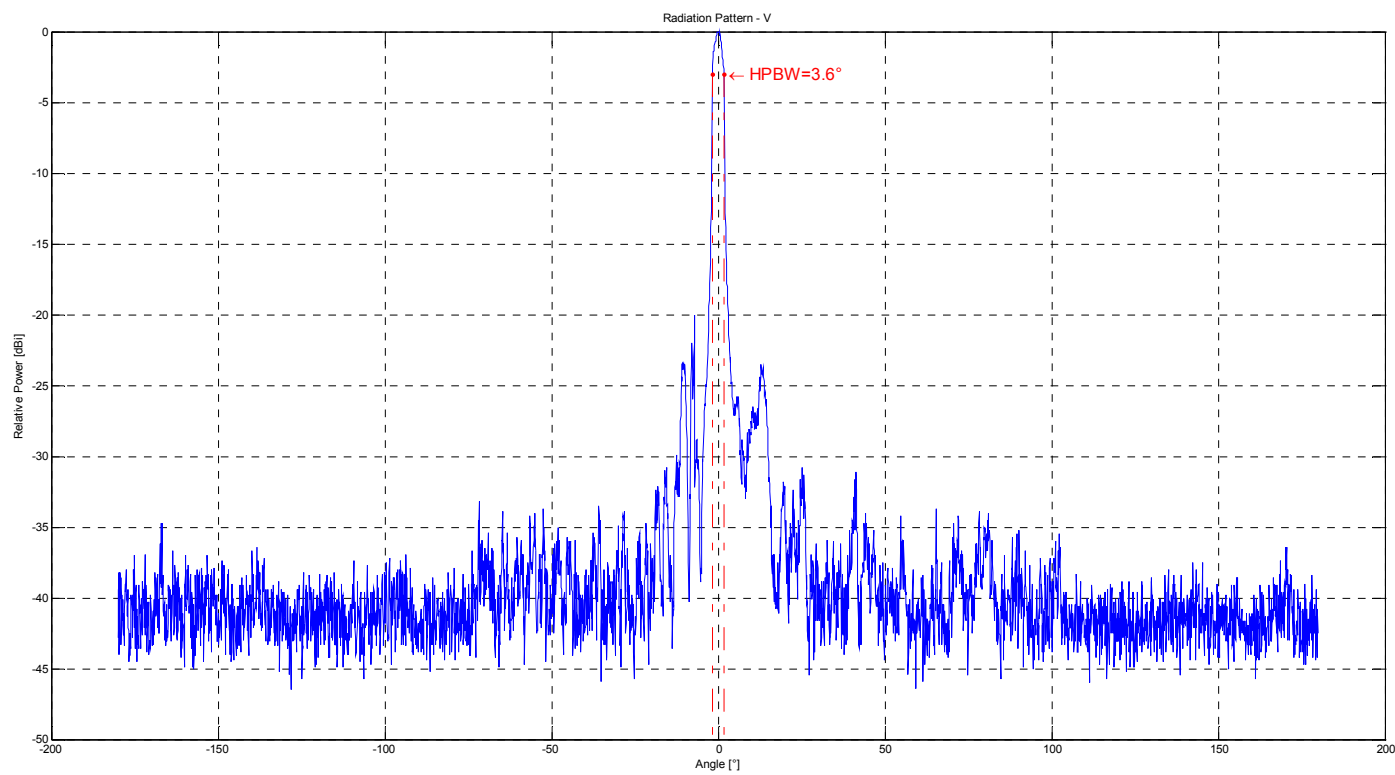


Figure 2.6. Vertical plane radiation pattern measured by GIOMAR s.p.a. and plotted using MATLAB©.

2.2 The radar constant

A pulsed radar transmits a sequence of short electromagnetic pulses and estimates the range to a target by measuring the time the signal takes from the radar to the target and return back to the radar.

Transmitted pulsed width is indicated by τ (generally less than one μs) and its repetition frequency is indicated with f_r or PRF (Pulse Repetition Frequency), typically of the order of hundreds of Hertz.

$$T_s = \frac{1}{f_r} \quad (\text{eqn. 2.1})$$

The transmitted signal of a pulsed radar is represented in the following Figure 2.7, where T_s is the Pulse Repetition Interval (PRI), as in eqn. 2.1:

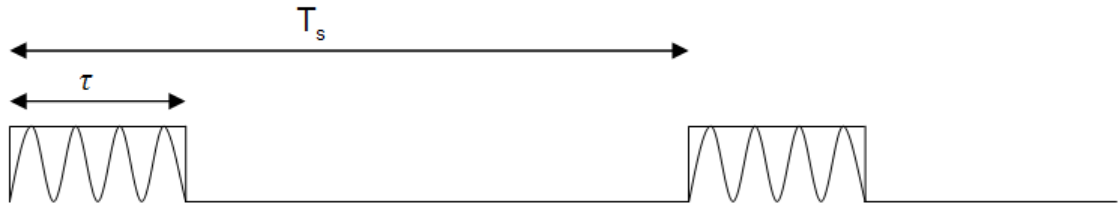


Figure 2.7. Transmitted signal of a pulsed radar

The pulse modulates the carrier frequency which is normally about some GHz. For not modulated pulsed radars, the range resolution (the minimum distance two targets must have to be separately detected) is:

$$\Delta r = \frac{c\tau}{2} \quad (\text{eqn. 2.2})$$

Considering a volumetric scatter caused by hydrometeors, the power received by the radar can be estimated considering the following equation.

$$P_r = \left(\frac{P_t \pi^3 G_0^2 \theta_{3dB}^2 \phi_{3dB} c \tau}{\lambda^2 1024 \ln 2} \right) L^2 |K|^2 \frac{Z}{r^2} \quad (\text{eqn. 2.3})$$

In this equation G_0 is the maximum antenna gain, θ_{3dB} and ϕ_{3dB} are the half power beam width characterizing the antenna radiation pattern, c is the speed of light in vacuum, τ is the pulse length, λ is the wavelength, L is an attenuation factor depending on atmospheric losses along the radar-target path, K is a constant depending from the dielectric properties of hydrometeors, r is the radar-target range and Z is the radar reflectivity factor.

Summarizing, the radar equation can be written in terms of Z , r and of a constant ($kost$) which takes into account all the radar system parameters:

$$P_r = \frac{kost}{r^2} \cdot Z \quad (\text{eqn. 2.4})$$

2.2.1 Radar constant evaluation

In this eqn 2.3 Z is expressed in [m^6/m^3], r in [m] and P_r in [W]. Therefore the constant $kost_1$ which includes all the radar system parameters is expressed in [W/m].

Table 2.4. Parameters for radar constant evaluation

P_t	10 kW
$ K ^2$	0,93
$\theta_{3dB} = \Phi_{3dB}$	62.8 mrad (3.6°)
G_0	34 dB
τ	400 ns
c	$3 \cdot 10^8$ m/s
f	9.41 GHz
λ	0.0319 m
$A_{txrx dB}$	2.2 dB
L	not considered

Using the parameters shown in the previous table and since Z is normally defined using the logarithmic scale as:

$$Z_{[dBZ]} = 10 \cdot \log_{10} Z_{[mm^6m^{-3}]} \quad (\text{eqn. 2.5})$$

while the received power is normally defined in [dBm] and the range in [km], the final form of the radar equation for the radar becomes:

$$P_{r,[mW]} = 10^{-21} \frac{k \sigma t_1}{r_{[km]}^2} \cdot Z_{[mm^6m^{-3}]} \quad (\text{eqn. 2.6})$$

or, alternatively,

$$P_{r,[dBm]} = -89.2 + Z_{[dBZ]} - 20 \cdot \log_{10} r_{[km]} \quad (\text{eqn. 2.7})$$

It is also necessary to consider the radar system losses. In order to evaluate them, we assumed that the same losses characterize the signal propagation from the transmitter (magnetron) to the antenna (A_{tx}) and from the antenna to the receiver (A_{rx}). Such losses include circulator (A_{circ}), waveguide (A_{wg}) and connections (A_{agg}) losses. Accordingly to the measurements made and the formal data sheet of the receiver provided by the manufacturer, the total losses in the transmitter-antenna or antenna-receiver “channel” are the following:

$$A_{tx} = A_{rx} = A_{circ} + A_{wg} + A_{agg} = (0.5 + 0.4 + 0.2) = 1.1 (\pm 0.1) \text{ dB} \quad (\text{eqn. 2.8})$$

Considering also the total transmission and reception losses $A_{txrx,dB} = 2 A_{tx,dB}$ the equation becomes:

$$P_{r,[dBm]} = -91.4 + Z_{[dBZ]} - 20 \cdot \log_{10} r_{[km]} \quad (\text{eqn. 2.9})$$

2.3 X-band mini weather radar signal processing

The development of the radar control software started in 2004 and is always in progress. In 2010 – 2011 it has been completely modified. The previous software, realized in C and compiled under Windows© Operating Systems, have been substituted with a C code for both control the radar and the data acquisition compiled under a Linux environment, in order to keep the entire system take advantage of the large amount of open source libraries available for free on the web.

The present complete radar signal processing (including the user software) is divided into two different chains. The first one considers all the operations implemented on the “on-board” software at the machine level, while the second one considers all the operations made before the final data storage and web visualization

2.3.1 Standard signal processing at machine level

The signal processing performed by the on-board software at the machine level can be divided into the following different blocks. **Figure 2.7** shows a conceptual sketch: each block is described in the following sections.

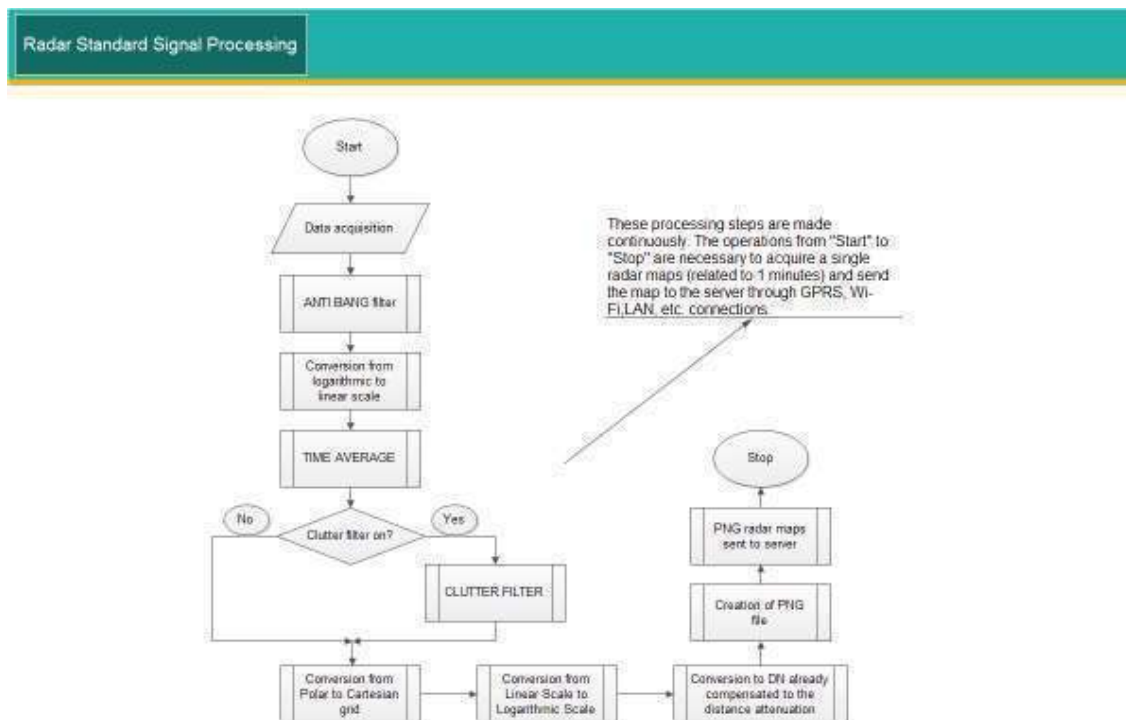


Figure 2.7. Flow diagram of the radar signal processing strategy on the radar control pc.

2.3.1.1 Data acquisition

For each antenna turn, the radar encoder acquires data from 4096 azimuth values and 2048 range values. Since the radar antenna makes 22 turns for minute, one entire horizontal plane scan (with an angular resolution of 3.6°) is accomplished in about 3 seconds. Strictly speaking, being the PRF equals to 800 Hz, only 2400 pulses are sent to scan the entire horizontal plan (the azimuth values not covered, are filled in with the last measurement available). This 4096 x 2048 matrix contains DN values.

The information of the received power P_r is given in output by the receiver in terms of Digital Numbers (DN), which are basically the output of the 8 bit sampling performed by the Analog-to-Digital converter. DN and the logarithm of P_r are linearly related. Considering a P_r range of $-100 \text{ dBm} \div 0 \text{ dBm}$, which corresponds to the DN range $0 \div 255$, the conversion rule to be applied is the following.

$$\text{DN} = (100 + P_r^{[\text{dBm}]}) \cdot 2.55 \quad (\text{eqn. 2.10})$$

2.3.1.2 “Anti-bang” filter

This filter is necessary to eliminate all the interferences caused by other radar systems working in the same bandwidth of the radar. The acquired 4096 x 2048 DN matrix is scanned considering each azimuth (row). If a high DN is found in a certain range-bin, its value is replaced with the averaged value of the surroundings azimuths (at the same range). This filter is always active and cannot be turned off.

2.3.1.3 Conversion to linear scale

The 4096 x 2048 DN matrix is converted into power values in mW, using the well known relationship in eqn. 2.10.

2.3.1.4 Time average

All the raw data (on a linear scale) acquired for each antenna revolution are averaged on a one minute time bases. Therefore, for each minute, a matrix of 4096 azimuth (rows)

and 2048 range (columns) values is available. This matrix actually contains received power (in mW) from each radar bin.

2.3.1.5 Anti-clutter filter

Raw data are pre-processed using the anti-clutter filter. The algorithm, numerically analyzes each range-bin and dynamically cleans its content if it is supposed to be contaminated by echoes coming from terrain (*ground clutter*). This algorithm was tested for several different case studies and performed quite well. The default delivery includes this preprocessing step. However, the filter can be deactivated or raw pre-filtered data can be made available on request using the advanced radar signal processing mode.

2.3.1.6 Conversion from polar to Cartesian grid.

The 4096 azimuth x 2048 range time averaged power (measured in mW) polar image is now converted into a 1024 x 1024 Cartesian pixel grid. Each Cartesian pixel contains the spatial average of all the values of the polar pixels included in the Cartesian one. This map represents a circular 30 km radius radar area coverage, with a virtual resolution of 60 m x 60 m.

2.3.1.7 Conversion from linear scale to logarithmic scale and to DN.

Time and space averaged values contained in the 1024 x 1024 Cartesian map are here converted into logarithmic scale. Moreover a compensation with the distance is applied in this step.

Considering eqn. 2.9 each pixel now contains the direct information on Radar Reflectivity factor Z :

$$x = P_{r,[dBm]} + 20 \cdot \log_{10} r_{[km]} = Z_{[dBZ]} - 91.4 \quad (\text{eqn. 2.11})$$

The corresponding image is further converted into DN (using the usual conversion rule):

$$\text{data} = (100 + x) \cdot 2.55 \quad (\text{eqn. 2.12})$$

(where x is the numerical content of each pixel) and the final radar image is created.

The image is created in a grayscale .png format on 8 bits with alpha channel. It allows to have a 256 levels range (from 0 to 255), exactly as the DN given as output from the radar receiver, and a good compression in order to do not generate a lot of useless traffic data between the radar and the server without loss information⁵ (**Figure 2.8**).



Figure 2.8. Example of grayscale .png images acquired by the radar installed in Turin in clear sky days without clutter filter (on the left) and by the radar installed in Palermo during a heavy rainfall event (on the right).

⁵ *Portable Network Graphics (PNG)* is a raster graphics file format that supports lossless data compression. PNG was created as an improved, non-patented replacement for Graphics Interchange Format (GIF), and is the most used lossless image compression format on the Internet. PNG supports different palette-based images (with palettes of 24-bit RGB or 32-bit RGBA colors), grayscale images (with or without alpha channel), and full-color non-palette-based RGB[A] images (with or without alpha channel). PNG was designed for transferring images on the Internet, not for professional-quality print graphics. PNG uses a 2-stage compression process: pre-compression: filtering (prediction), compression: *DEFLATE*. PNG uses a non-patented lossless data compression method known as *DEFLATE*, which is the same algorithm used in the more famous *ZLIB* compression library (Wikipedia).

2.1.3.8 Storage of the radar image into the server

Each image is then sent to the server, exploiting the internet (through LAN or GPRS) connection.

2.3.2 Standard signal processing at server level

The processing steps applied to each 1024 x 1024 Cartesian radar image (.png) at the server level are represented in the **Figure 2.9** and describe in the following.

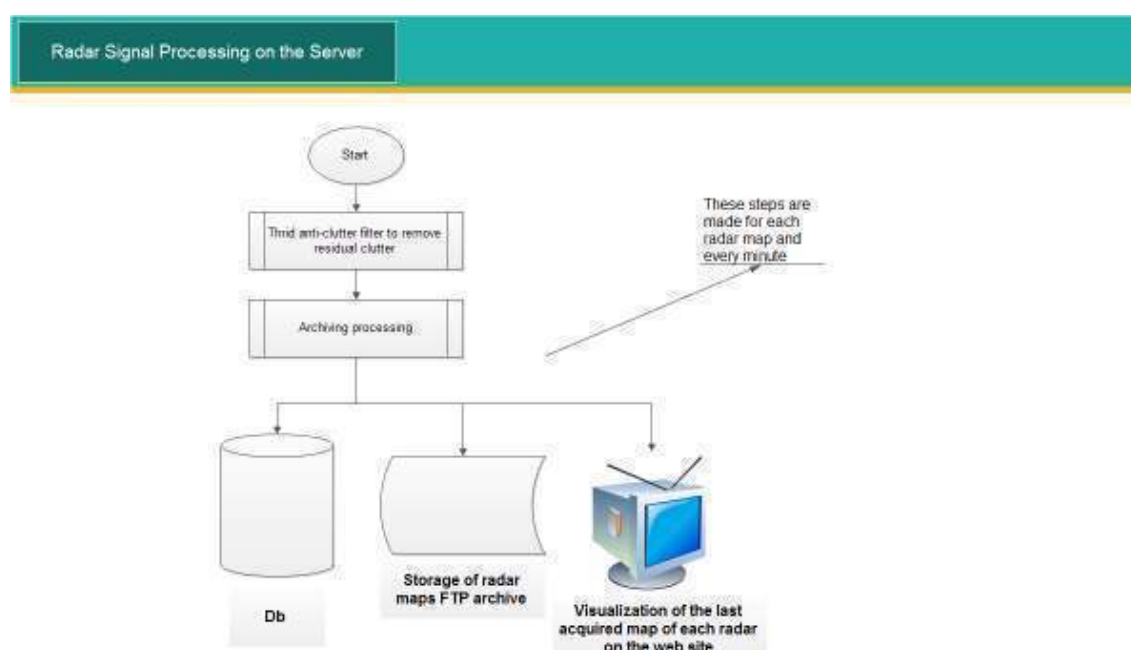


Figure 2.9. Processing steps at server.

2.3.2.1 Third Anti-clutter filter

A further step of the anti-clutter filter processing developed by Envisens Technologies s.r.l. is applied at this stage. This step can be deactivated or raw data can be made available on request.

2.3.2.2 File storage into the radar archive and to the radar database

At this point the radar image is definitively stored both on the radar FTP archive and pm a ad-hoc designed database. The image is now available to the user. In order to extract

the Radar Reflectivity factor from each pixel of the 1024 x 1024 .png image, its content should be converted exploiting the eqn. 2.11 and the eqn. 2.12.

Reflectivity factor Z in dBZ can be obtained simply adding 91.4 to the converted x value. This value will be further discussed in the following paragraphs because it depends on the radar systems and its calibrations

2.3.2.3 Delivery of a temporary file for the web visualization.

A temporary file is generated, it is converted into Rainfall Rate R (in mm/h) exploiting the Marshall and Palmer equation and some correction factors (this equation is discussed in the **chapter 1** and further consideration and studies, in particular about correction factors, will be presented in **chapter 4**):

$$Z_{[mm^6m^{-3}]} = 316 \cdot R^{1.5} \quad (\text{eqn. 2.12})$$

The map is sent to the web site for its final visualization where a common palette is used to color the temporary file with the rain rate map.

2.3.3 Advanced signal processing at machine level

The standard signal processing can be modified by authorized users in order to implement some advanced features of the system.

Each advanced feature can be controlled through the configuration file reported in **Figure 2.10** or through other advance “users” defined on the elaboration unit of the radar system.

```
acp-delta 2090
site-name upa01est2135
clutter-f 1
server-web 1
```

Figure 2.10. Example of radar configuration file.

Example reported in **Figure 2.10** shows the default values of the configuration file. In particular, the parameter *clutter-f* set to “1” means that all the clutter filters are active. The *server-web* set to “1” means that the web server installed on the radar control pc (usually it is Apache 2) is active and it is possible to look at the radar maps by simply connecting to the radar dedicated address using a simple browser (**Figure 2.12**). It is usually active in the most recent version of the radar control software but can be disabled, for instance, if some particular and specific data security and confidentiality are needed.

The parameter *clutter-f* can also be set to “0” in order to disable all the clutter filter on the radar maps. This feature is particular useful during the installation and configuration phases. It is useful for calibration purposes, system orientation towards the northern direction, control of the radar stability (more details in **Chapter 3**), research operations. **Figure 2.11** shows an example of two maps acquired by the same radar: in the first one the clutter echoes have been filtered out, while in the second all the clutter filter are turned off. Both the images have been acquired in clear sky days.

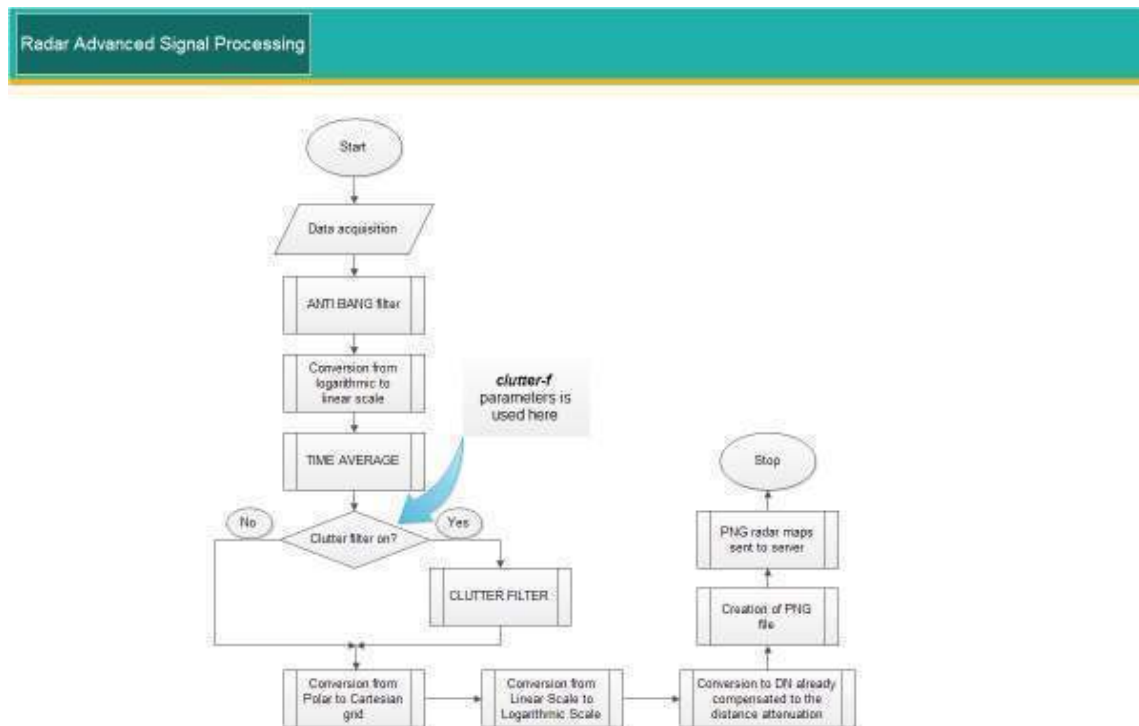


Figure 2.11. Effect of the parameters clutter-f with respect to the standard signal processing operations.

2. The X-band mini weather radar and the meteoradar network

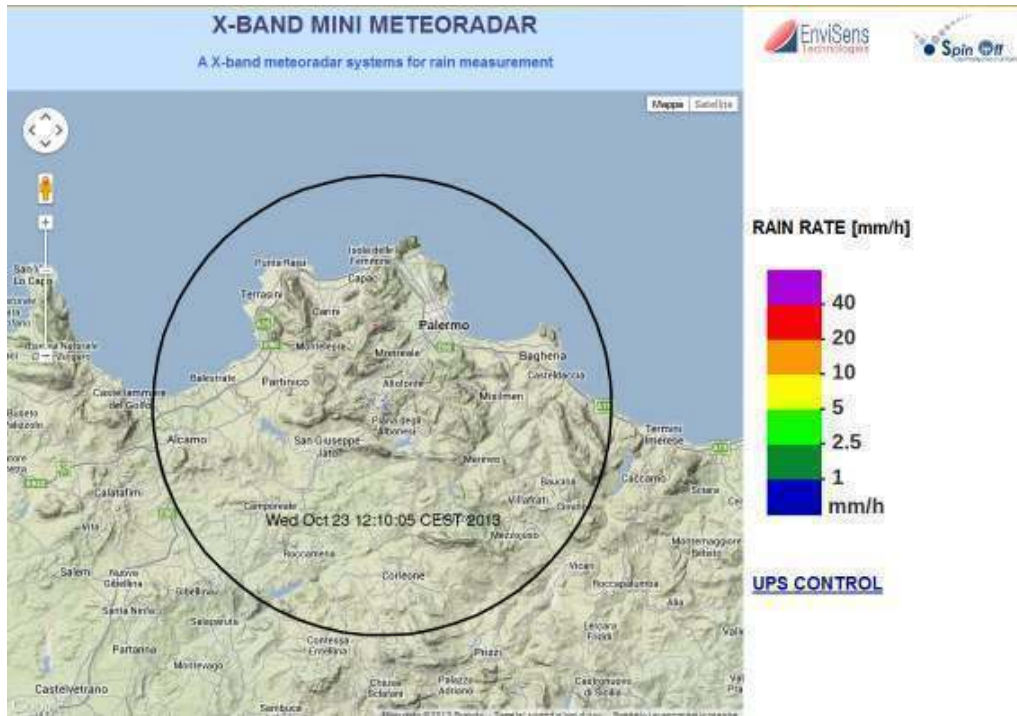


Figure 2.12. Example of active radar web server.

The example is related to the radar installation made together with the University of Palermo.

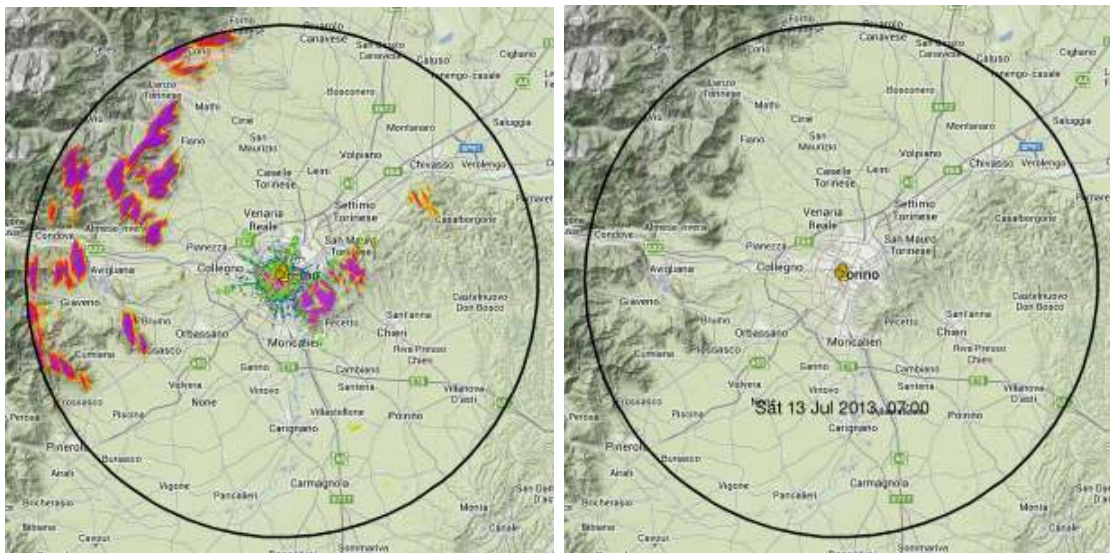


Figure 2.13. Effect of clutter filter enabled and disabled. The maps are related to the radar installed in Turin.

There are two other parameters in the radar configuration file which are used to system orientation towards the northern direction (*acp-delta*) and to set the name of the

installation (*site-name*). They are set during the installation phases and not modified if no modifications occurred.

By connecting as authorized user to the radar control pc (the credential are different for each radar) it is possible to activate the acquisition of the radar maps in polar format. The polar format acquisition can be run in parallel with the standard acquisition of Cartesian maps, and the acquired maps, used mainly for research purposes, can be stored on board or sent to a server exploiting the radar network connection.

A radar polar map is a matrix of 4096 rows and 2048 columns (**Figure 2.15**). Each row represent an encoder position values and each row a radar bin with an apparent resolution of 15 m. It is to note that the first row of the matrix does not correspond to the North, but to the direction corresponding to the 0 value of the radar positioning encoder. To point the radar polar maps to the North it is necessary to know *the acp-delta* parameter written in the configuration file.

The polar map is encoded on a 256 grayscale .png image (exactly as for Cartesian maps) where each pixel represent a matrix value in order to compress its content exploiting the redundancy of pixels with the same value.

Radar polar maps acquisition can be turned on or off depending on the user needs. They are used mainly for research purposes and they are without any clutter filtering operation, in order to keep their data as raw as possible.

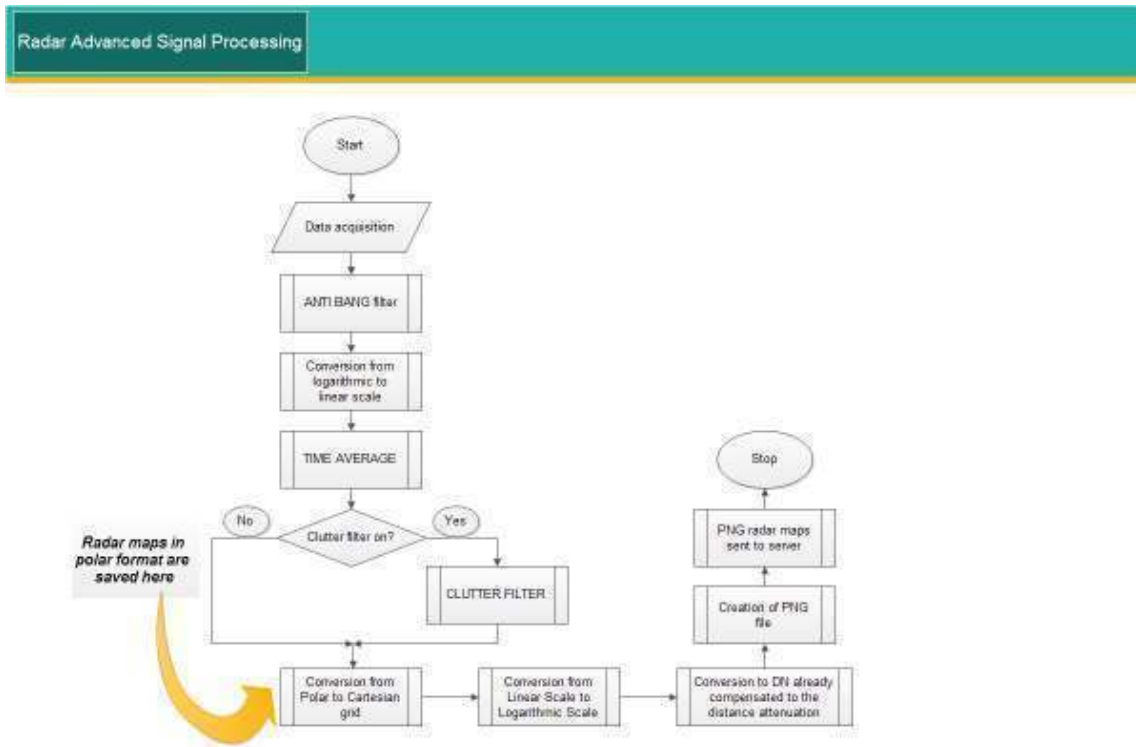


Figure 2.14. Acquisition of polar maps with respect to the standard signal processing operations.



Figure 2.15. Example of polar map acquired by the advanced radar control software.
The maps are related to the radar installed in Turin.

2.4 The meteoradar network

Although some experimental installations of early prototypes of X-band mini were done starting from 2007 and the very first operational installation was made with the radar on the roof of Politecnico di Torino in 2008-2009, the first fully operational network of a number of mini radars was set up starting from 2010.

During October 2010, the first network of 4 mini weather radar network was created with 4 radars installed in Sicily, Italy and it is described in a publication of S. Bertoldo et. al.⁶.

Since 2010, different installation and de-installation have been made and now the mini weather radar network it is made up by 8 radar systems (the network is entirely shown in **Figure 2.16**):

- one installed in Turin town (2010):
- one is installed in the Aosta Valley (2011)
- one near Foggia, in the South of Italy (2012)
- one in the town of Palermo in Sicily Region (2012)
- two in Israel in collaboration with the Hebrew University of Jerusalem (2012),
- one near Nizza Monferrato in Piedmont Region (2013)
- one in Parma in collaboration with Parma Calcio, North Italy (2013).

As described in the **section 2.3.2** the radar maps are sent from each radar to the central server: the radar network has a star topology.

On the server the maps are stored both as single png file in a well defined directories tree and on a database ad hoc designed for the radar applications. The directory tree is necessary because the server allow to specific authorized users the FTP access to download radar maps, while the database allow to compute specific operation and develop specific applications and services described in the following.

⁶See footnote 2.

2. The X-band mini weather radar and the meteoradar network

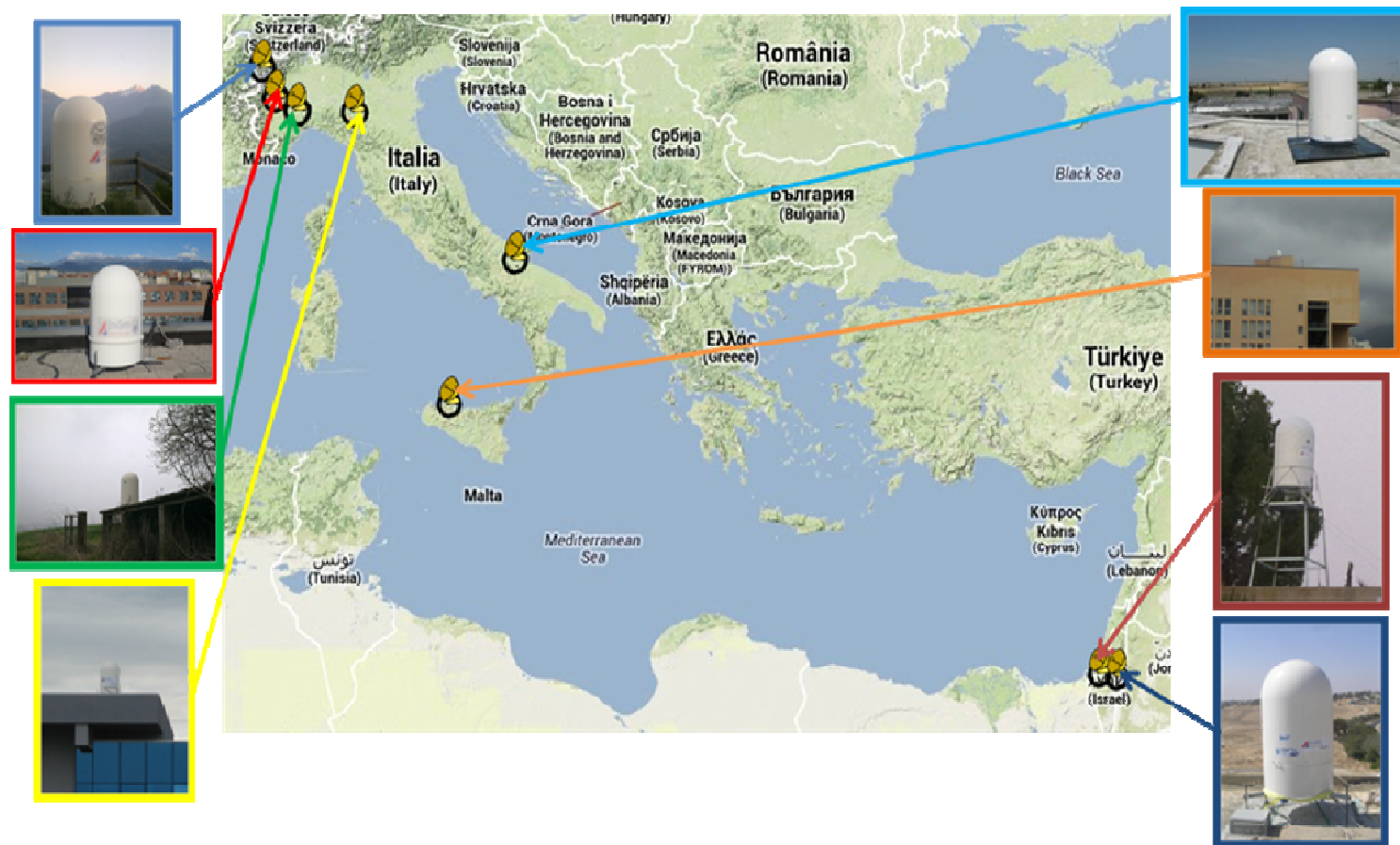


Figure 2.16. The meteoradar network with the pictures of the active installation (2014).

2.4.1 The meteoradar FTP archive

The FTP archive is made up by a series of directories, each one devoted to store the maps coming from a single radar. There are also some directories related to store older radar maps in order to avoid a too much large number of file stored in a single directory. By simply connecting to the meteoradar network server and enter in the directory related to the desired period of time it is possible do select and download a certain number of radar maps (Figure 2.17).

Nome	Est.	Dimens.	Data/Ora	Attr.
[.]		<DIR>	01/01/1601 02:00—	
[aos02est 11]		<DIR>	23/10/2013 14:43-755	
[archivist.d]		<DIR>	30/05/2013 12:53-755	
[data_ago_ott_2013]		<DIR>	08/10/2013 13:13-755	
[data_apr_ago_2012]		<DIR>	24/07/2013 13:31-755	
[data_dec_2012_apr_2013]		<DIR>	22/04/2013 00:00-755	
[data_mag_lug_2013]		<DIR>	22/07/2013 09:40-755	
[data_sett_nov_2012]		<DIR>	12/12/2012 00:00-755	
[incoming]		<DIR>	23/10/2013 14:43-755	
[isr01est 18]		<DIR>	23/10/2013 14:43-755	
[isr02est 20]		<DIR>	23/10/2013 14:43-755	
[logfilecumulate]		<DIR>	23/07/2013 22:07-755	
[maintenance]		<DIR>	25/07/2013 08:06-755	
[mask]		<DIR>	15/02/2012 00:00-755	
[noinsert]		<DIR>	28/09/2013 21:59-755	
[nzz01est 22]		<DIR>	22/10/2013 19:10-755	
[pgl01est 19]		<DIR>	08/10/2013 13:12-755	
[prm01est 23]		<DIR>	23/10/2013 14:43-755	
[Radars]		<DIR>	29/07/2013 12:16-755	
[tor01est 10]		<DIR>	23/10/2013 14:43-755	
[upa01est 21]		<DIR>	23/10/2013 14:43-755	
[zone]		<DIR>	06/07/2011 00:00-755	

Figure 2.17. Example of FTP archive. It is possible to note different directory related radar directories to archive radar maps (highlighted in green), directories for elder maps (highlighted in blue) and working directories (not highlighted).

2.4.2 Radar map name

Each radar maps has a specific name which include some information about the site of radar installation and date and time of acquisition. Such name is set up on the control pc on each radar using the information written in the configuration file. This choice allow the processing software on the server to store the maps on the specific directory and to correctly archive them on the database.

An example of name of radar map is: *pal02est13252011-02-22_15:14:04.png*.

It contains:

- The name of the radar (*pal02est13*). The name contains information about the site (the first five characters, *pal02*) and the radar unit (the characters from 6 to 10, *est13*). It is necessary to correctly archive the maps in the database.
- Two character representing the elevation of the antenna (*25* means, 2.5° above the horizontal plane).
- The date of acquisition (in the format yyyy-mm-dd, *2011-02-22*).
- The underscore “_” character.
- The time of acquisition (in the format hh:mm:ss, *15:14:04*).

2.4.3 The database of the meteoradar network

The radar database structure is very simple and it is reported in the following Entity – Relationship (E/R) scheme.

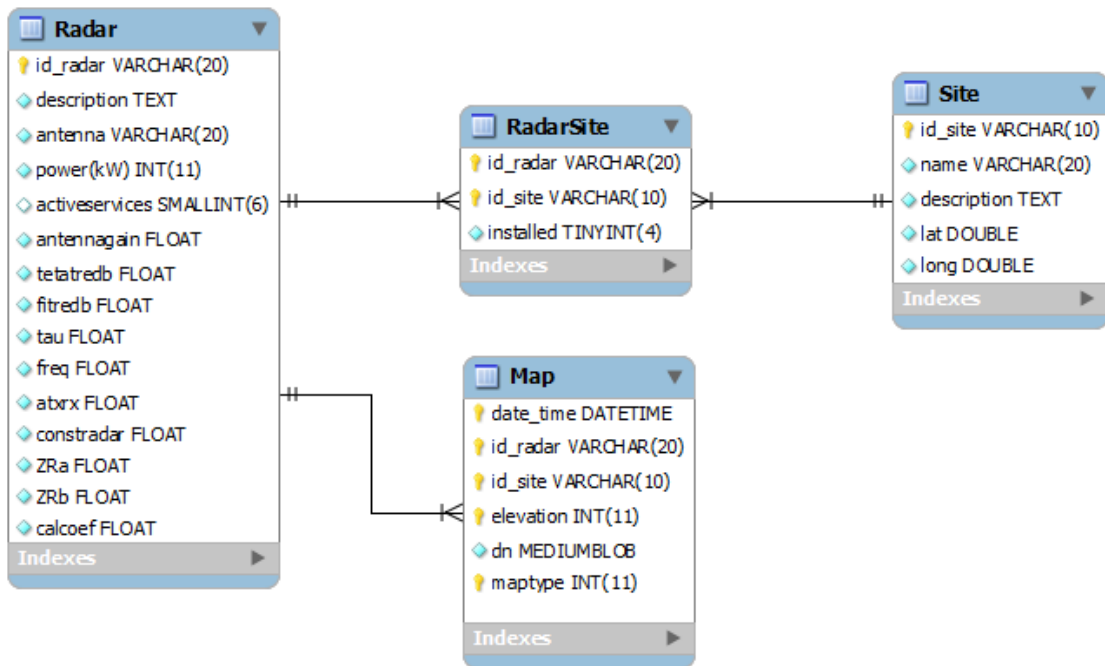


Figure 2.18. E/R scheme of the mini weather radar network database.

The database structure joins the simplicity with the functionality avoiding difficult database operations. It allows to implement the most of the services needed for the mini

weather radar network and, if necessary, can be modified by simply “alter table operations” on the tables without altering the operational services.

The tables of the database are described in the following together with their fields.

2.4.3.1 Radar table

The *Radar* table contains all the information about a single radar unit. The fields of the table contains the following information.

- *Id_radar*: it is the primary key of the table and identify a single radar unit with all its characteristics.
- *Description*: description of the radar unit including some practical information of installation.
- *Antenna*: it contains some information about the antenna used in a single radar unity.
- *Power*: the transmitted power.
- *Activeservices*: if it is set to “1” means that the radar unit has the services and the application active on the web site. A certain installation can be operative but the services may be disabled for contractual reasons.
- *Antennagain*: it is the gain of the antenna of the radar unit.
- *Tetatredb*: it represents the Half Power Beam Width (HPBW) of the antenna used in the radar unit. The HPBW is assumed to be the same both in horizontal and in vertical plane.
- *Tau*: it is the pulse duration (in nanoseconds).
- *Freq*: it contains the real frequency in GHz, measured for a specific radar unit.
- *Atrx*: it contains the information about the measured attenuation inside the radar system.
- *Constradar*: it is the radar constant evaluated with the previous parameters.
- *ZRa*: it is the *a* coefficient of the Z-R (or Marshall and Palmer) equation used to estimate the rain in a specific installation.

- *ZRb*: it is the *b* coefficient of the Z-R equation used to estimate the rain in a specific installation.
- *Calcoeff*: it contains the calibration coefficient, usually due to the calibration using the rain gauges, but also considering other losses not measured but present in the radar system.

2.4.3.2 *Site table*

The *Site* table contains all the information about a single site of installation where one or more radar can be installed. The fields of the table contains the following information.

- *Id_site*: it is the primary key of the table and univocally identifies a specific site of installation of radar units.
- *Name*: it is the name of the site; it usually corresponds to the name of the town or the place where the radar is installed.
- *Description*: it contains some more information about the site.
- *Lat*: the latitude (in decimal degree) of the site.
- *Long*: the longitude (in decimal degree) of the site.

2.4.3.3 *RadarSite table*

The *RadarSite* table is a “relation table” and comes from the relation N:M between the tables *Radar* and *Site*. In fact a single radar unit could be, in principle used for different installations, in different time periods, and the same site could host more than on radar installations, obviously considering different period. The fields of the table contains the following information.

- *Id_radar*: it contains, as foreign key, the id of the radar.
- *Id_site*: it contains, as foreign key, the id of the site.
- *Installed*: if it is set to “1”, means that a certain radar is installed on a specific site, and the installation is operative.

The fields *id_radar* and *id_site* together are also, together, the primary key of the table.

2.4.3.4 Map table

The *Map* tables contains all the radar maps acquired by each installations, together with the associated information (site, radar, date and time of acquisition). The fields of the table contains the following information.

- *date_time*: date and time of acquisition of a specific radar map.
- *id_radar*: code of the radar which acquire the map.
- *id_site*: site of installation of the radar which acquire the map.
- *elevation*: elevation of the antenna at which the radar map has been acquired.
- *DN*: it contains the radar maps in .png format
- *Maptype*: it indicates the type of the radar map stored in the record The maps can be acquired by the radar and related to a single minute, or cumulated rain maps. This field is not used, in the current version of the database and it was thought for future developments.

2.4.4 The meteoradar network services

The meteoradar network offer to users some specific realized services. In particular the developed services are the followings and all the operations necessary to run them are run in background and scheduled at certain time intervals on the server.

- Instantaneous rain maps related to the last minute.

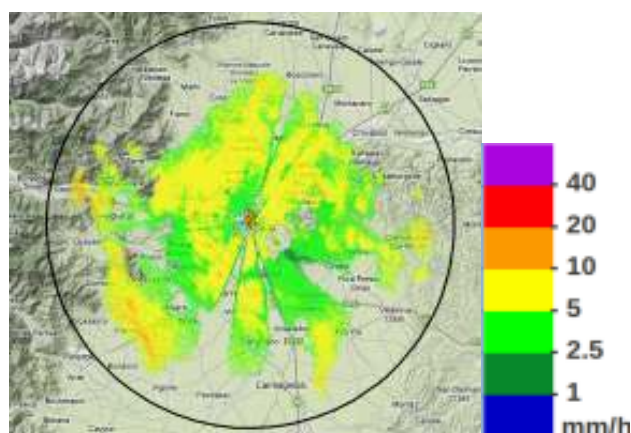


Figure 2.19. Example of instantaneous rain map.

- Last hour cumulated rain.
- Last 6 hours cumulated rain.
- Last 12 hours cumulated rain.
- The previous day cumulated rain.

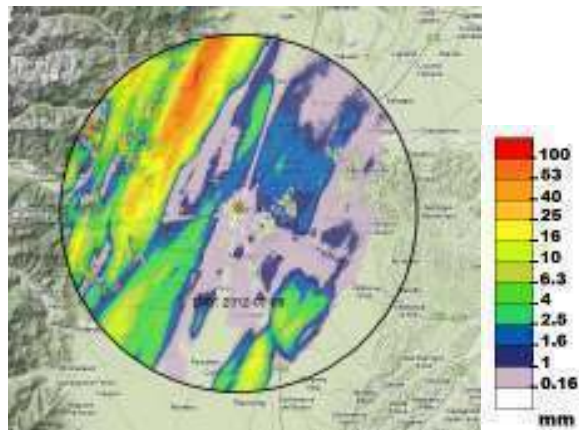


Figure 2.20. Previous day cumulated rain.

- Evolution of precipitations in the last 15 minutes.

2.4.5 Free Android© App

A free Android© app is available for free on Google store© which allow users to access all the meteoradar network services by a smartphone. The application is called Meteoradar-IT.

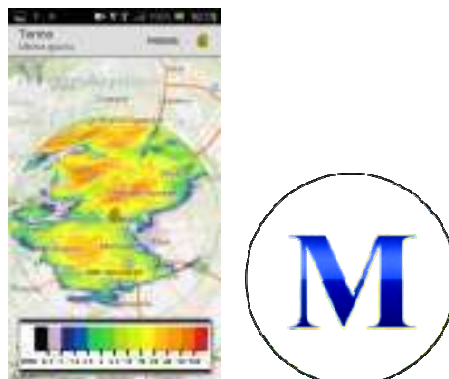


Figure 2.21. Screenshot and logo of the Android© App Meteoradar-IT.

3.

Use of ground clutter echoes to monitor the X-band mini weather radar stability

3.1 Clutter definitions

Clutter is a term used to describe any object that may generate unwanted radar returns that may interfere with normal radar operations. By this definition, what is considered clutter for a certain type of radar can be useful signal for other radars and vice-versa. For instance, X-band radar applications could be for both the detection of ships on the sea and estimation of rain. The two applications “exchange” what is considered clutter and what is useful signal.

Parasitic returns that enter the radar through the antenna’s main lobe are called main lobe clutter; otherwise they are called side lobe clutter. Clutter can be classified into two main categories: surface clutter and airborne or volume clutter. Surface clutter includes trees, vegetation, ground terrain, man-made structures, and sea surface (sea clutter). Volume clutter normally has a large extent (size) and includes chaff, rain, birds, and insects. Surface clutter changes from one area to another, while volume clutter may be more predictable. Surface clutter is the most interesting for what concern weather radar because it must be filtered out if you want to collect echoes coming from rain fields, while it can be used for calibration purposes if it is not filtered out and if its echoes are acquired in clear sky days.

Clutter echoes are random and have thermal noise-like characteristics because the individual clutter components (called scatterers) have random phases and amplitudes. In many cases, the clutter signal level is much higher than the receiver noise level. Thus, the radar's ability to detect targets embedded in high clutter background depends on the Signal-to-Clutter Ratio (SCR) rather than the Signal to Noise Ratio (SNR). White noise normally introduces the same amount of noise power across all radar range bins, while clutter power may vary within a single range bin. Clutter Radar Cross Section (RCS) can be defined as the equivalent radar cross section attributed to reflections from a clutter area.

The average clutter RCS is given by

$$\sigma_c = \sigma^0 A_c \quad (\text{eqn. 3.1})$$

where σ^0 is the clutter scattering coefficient, a dimensionless quantity that is often expressed in dB..

3.1.1 Surface Clutter

Surface clutter includes both land, mountains, hill and sea clutter, and is often called area clutter. It is also a major concern for ground-based radars when searching for targets at low grazing angles. The grazing angle is the angle from the surface of the earth to the main axis of the illuminating beam, as illustrated in **Figure 3.1**.

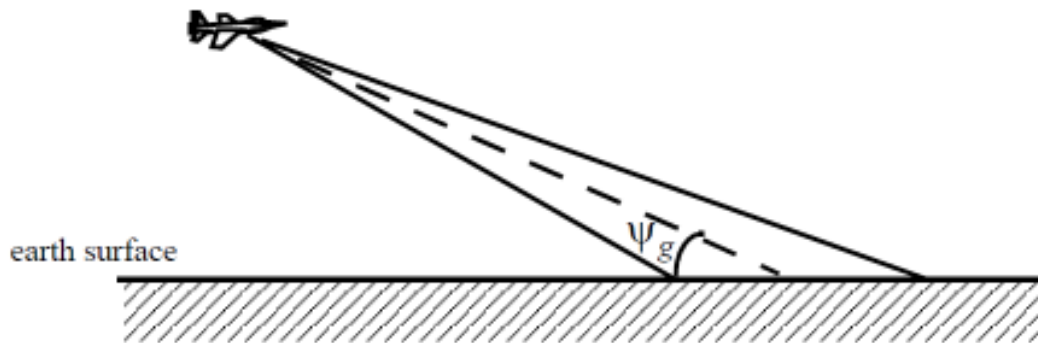


Figure 3.1 Example of Grazing Angle for space borne radar.

Three factors affect the amount of clutter in the radar beam. They are the grazing angle, surface roughness, and the radar wavelength. Typically, the clutter scattering coefficient is larger for smaller wavelengths. **Figure 3.2** shows a sketch describing the dependency of on the grazing angle. Three regions are identified; they are the low grazing angle region, flat or plateau region, and the high grazing angle region.

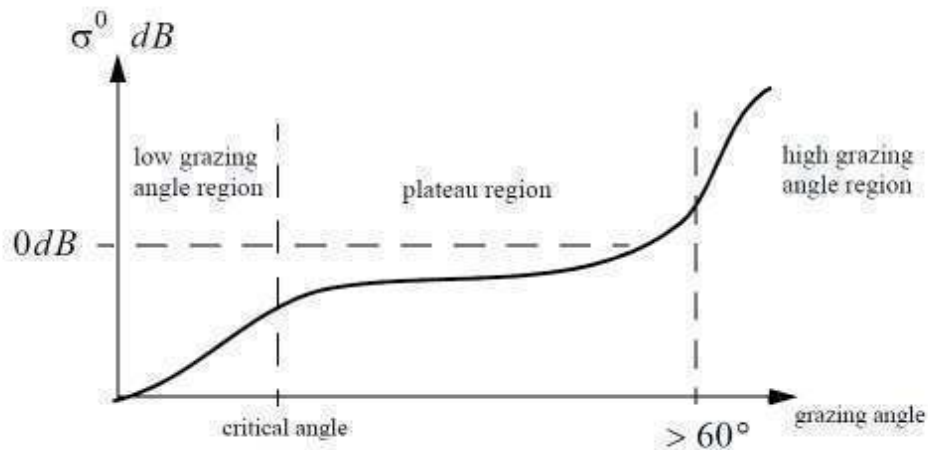


Figure 3.2 Grazing angle.

Clutter at low grazing angles is often referred to as diffuse clutter, where there are a large number of clutter returns in the radar beam (non-coherent reflections). In the flat region the dependency of on the grazing angle is minimal. Clutter in the high grazing angle region is more specular (coherent reflections) and the diffuse clutter components disappear. In this region the smooth surfaces have larger than rough surfaces, opposite of the low grazing angle region.

For what concern X-band band weather radar the type of clutter more present in the radar beam, which should be filtered out is the one coming from high grazing angle region. In fact it is the clutter coming from hills and mountains surrounding the radar installations.

3.1.2 Volume Clutter

Volume clutter has large extents and includes rain (weather), chaff, birds, and insects. The volume clutter coefficient is normally expressed in square meters (RCS per resolution volume). Birds, insects, and other flying particles are often referred to as angle clutter or biological clutter.

As mentioned earlier, chaff is used as an Electronic Countermeasure (ECM) technique by hostile forces. It consists of a large number of dipole reflectors with large RCS values. Historically, chaff was made of aluminum foil; however, in recent years most chaff is made of the more rigid fiberglass with conductive coating. The maximum chaff RCS occurs when the dipole length is one half the radar wavelength. Weather or rain clutter is easier to suppress than chaff, since rain droplets can be viewed as perfect small spheres.

It is to consider that for X-band mini weather radar volume clutter is not very important. In fact it is devoted to detect echoes coming from rain and not to suppress them.

3.1.3 Clutter for X-band mini weather radar

The clutter for X-band mini weather radars used in the meteoradar network can be due to urban areas, and mountain and hills in the surroundings of each installations. It can also be due to signal coming from back lobes of the antennas if the installation is made in mountainous environment.

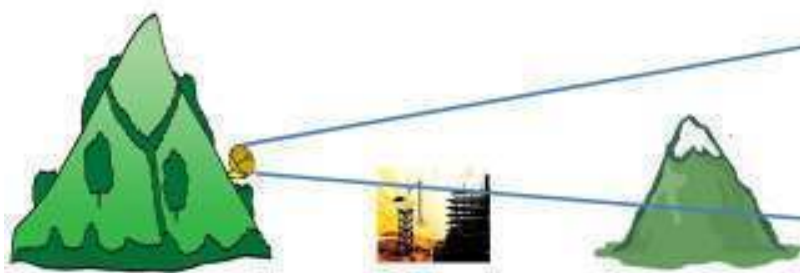


Figure 3.3 Different type of clutter for X-band mini weather radar.

Considering as example the radar installed in Turin, on the roof of Politecnico di Torino, and considering only echoes from ground observed in clear sky conditions it is

possible to identify three different areas of clutter returns (Figure 3.4)¹: “Urban Clutter” which can be observed considering the area highlighted in blue, “Hill Clutter” coming from areas highlighted in red and “Mountainous Clutter”, characterizing the green area.

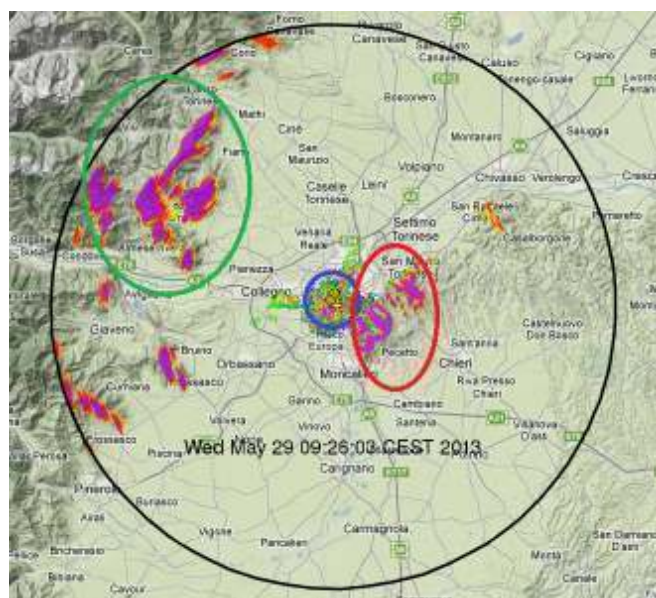


Figure 3.4. Example of instantaneous clutter map observed by the Turin radar.

3.2 Use of Ground Clutter Echoes to monitor the radar stability

In order to assure good performances in the rain monitoring and measurement, it is important to control the stability of the overall radar system components. These sub-systems may suffer for some degradations due to:

- external factors (e.g. temperature fluctuations, humidity)
- equipment related issues (e.g. frequency drift of the magnetron, de-tuning of the receiver filter).

To monitor the radar system stability it is possible to use ground clutter data, which are echoes coming from terrain scattering effects normally present in a large number of radar bins, acquired during clear sky days. In fact as already presented with

¹S. Bertoldo, R. Notarpietro, M. Branca, G. Dassano, C. Lucianaz, O. Rorato, M. Allegretti, *Characterization of the receiver filter of a X-band weather radar to improve the performance of an application to control the radar stability*, IEEE ICEAA 2013, Torino (ITA), 9-13 September 2013, pp. 935-938

the RCA (Relative Calibration Adjustment) algorithm described in the paper given by D.S. Silberstein² originally proposed for a S-band ground radar, the Probability Distribution Function (PDF) of the clutter echoes and, consequently, the corresponding Cumulative Distribution Function (CDF), should significantly change only if modifications on the radar systems occurred. Therefore clutter echoes acquired during clear sky days can be used to control the radar stability also for X-band mini weather radar. Since clutter echoes are coming from the same targets, differences in the probability distributions may only be due to modifications occurred in the system parameters or in some system hardware component.

3.2.1 RCA (Relative Calibration Adjustment) Algorithm

The RCA (Relative Calibration Adjustment Algorithm) was proposed to check the absolute and day-to-day calibrations of radar sensitivity are of a radar installed on Kwajalein Atoll, in the Republic of Marshall Island, Pacific Ocean. The radar is necessary to provide a baseline calibration for the control of measurements of rainfall made by the Tropical Rainfall Measuring Mission.

The method to check the calibration of the radar uses echoes from a multiplicity of ground targets. The daily average clutter echoes at the lowest elevation scan have been found to be remarkably stable from hour to hour, day to day, and month to month within better than 1 dB. They vary significantly only after either deliberate system modifications, equipment failure, or other unknown causes. A Cumulative Distribution Function of combined precipitation and clutter reflectivity ($[Z] = \text{dBZ}$) is obtained on a daily basis, regardless of whether or not rain occurs over the clutter areas. The technique performs successfully if the average daily area mean precipitation echoes (over the area of the clutter echoes) do not exceed 45 dBZ, a condition that is satisfied in most locales. In comparison, reflectivities associated with the most intense clutter echoes can approach 70 dBZ. Thus, the level at which the CDF reaches 95% is affected only by the clutter and reflects variations only in the radar sensitivity. Daily

² D. S. Silberstein, D. B. Wolff, D. A. Marks, D. Atlas and J. L. Pippitt, *Ground Clutter as a Monitor of Radar Stability at Kwajalein, RMI*, Journal of Atmospheric and Oceanic Technology, Vol. 15, No. 11, pp 2037-2045, 2008.

The method has been found to be robust and may be applicable to other ground-based radars.

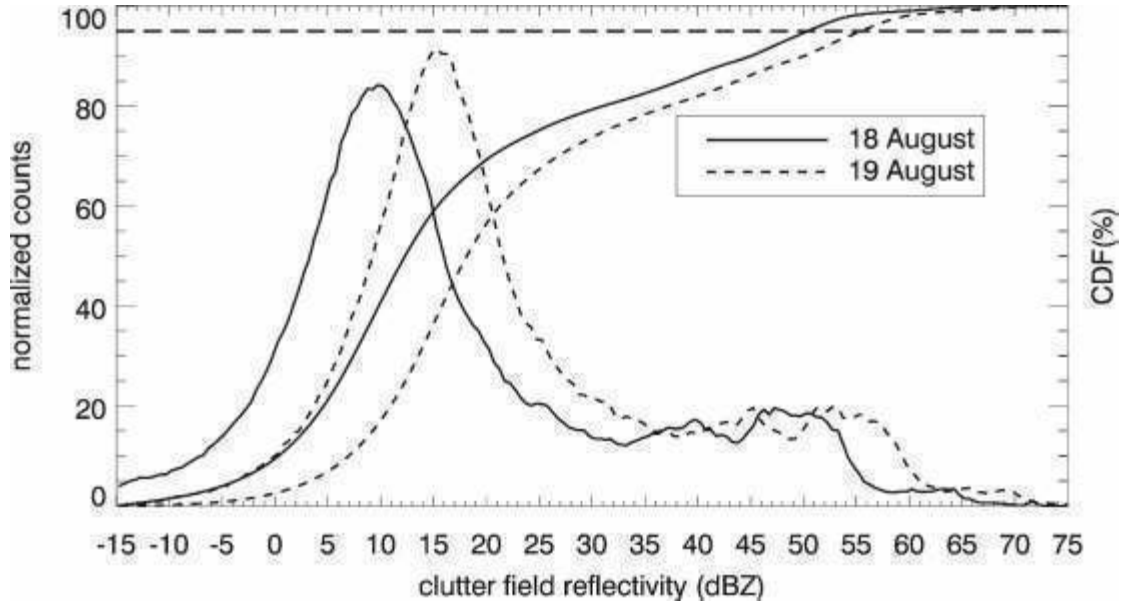


Figure 3.5. Comparison of two daily PDFs/CDFs from August 2003. The horizontal dashed line represents the 95th percentile of the CDFs. Failure of the CDF curves to converge at the upper percentiles of the reflectivity is an indication of a calibration shift (D. S. Silberstein, 2008).

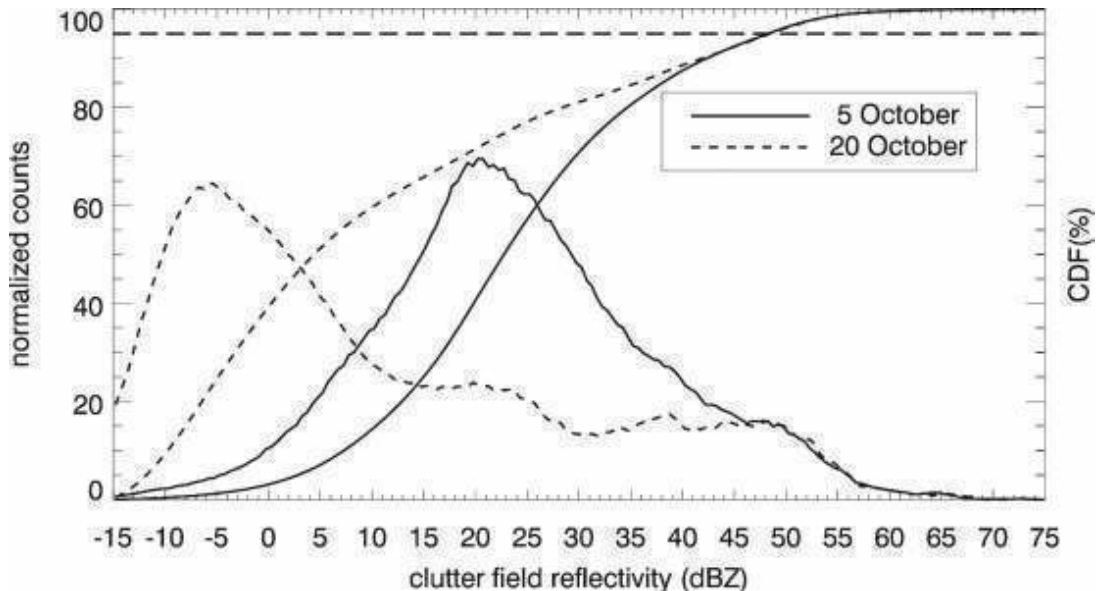


Figure 3.6. Comparison of two daily PDFs/CDFs from October 2001. The horizontal dashed line represents the 95th percentile of the CDFs. Distinctly different meteorological conditions exist on the two dates displayed, yet the CDF curves converge at the upper percentiles of the reflectivity, indicative of stable radar calibration (D. S. Silberstein, 2008).

The previous figures show how the RCA algorithm works: the PDF and corresponding cumulative distribution function (CDF) have been computed based on an entire day of data. Those for consecutive days from August 2003 are shown in **Figure 3.5**. The shift in the mode of the PDF between 18 August (solid curve) and 19 August (dashed) is the same as that throughout the entire CDF. It is worth noting that the meteorology on these two dates is quite similar with only widely scattered rainfall on both dates; however, the CDFs for these two consecutive dates differ considerably at higher reflectivities, indicating a change in CDF. Independent engineering logs provided by 3D Research Corporation (3DRC) reveal that this particular change is related to the replacement of a directional coupler on 19 August.

On the other hand, considering **Figure 3.6** is related on 2001. In the second half of the year, it was generally accepted that the radar was operating in a relatively stable mode as determined by engineering logs. The stability was confirmed analyzing the CDF where there are not any significant changes.

3.2.2 X-band mini weather radar ground clutter echoes

Based on the principles of RCA method, ground clutter echoes acquired during clear sky days can be used to control the radar stability also for X-band mini weather radar.

In order to realize an application to check the radar stability, it is necessary to define how it is possible to use PDF (or CDF) and to identify some useful indicators of the radar calibration. To do that it has been necessary to simulate some controlled failures and analyze the clutter probability distribution function.

The acquisition different set of ground clutter maps allow also to characterize the radar receiver filter. In fact, even if ground clutter echoes are mainly useful to control the system degradation, a fully characterization of the receiver filter is however necessary to improve the radar stability control algorithm definitions and its performances.

3.3 Definition of indicators to control the X-band mini weather radar stability and experimental results

The clutter analysis techniques were applied to ground clutter data acquired by the Turin's radar installation which is placed on the roof of the Polytechnic of Turin, near the city center. From this position, a quite high number of radar bins are contaminated by ground clutter echoes (**Figure 3.7**).

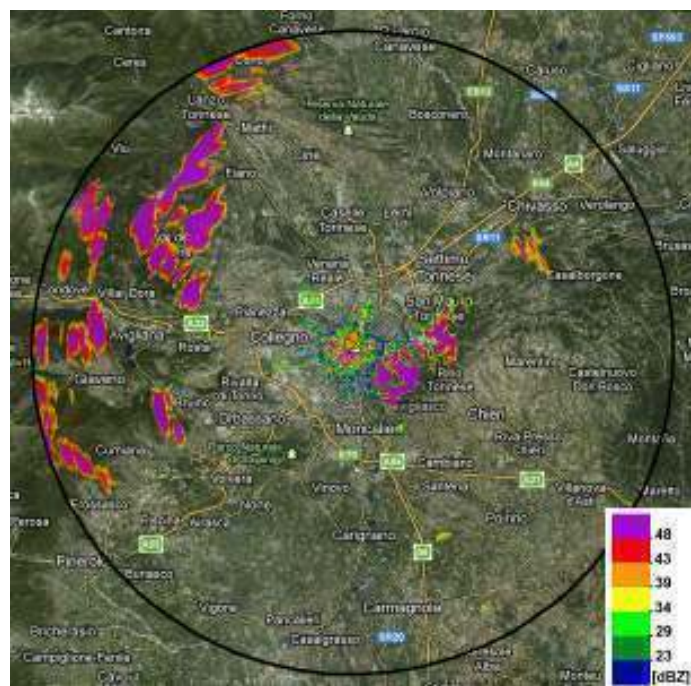


Figure 3.7. Example of clutter map acquired with the X-band mini radar installed in Turin and superimposed on a cartographic system.

The most simple operation to simulate a radar equipment failure is to intentionally “de-tune” the receiver filter. This can be made by software, since the receiver filter tuning is controlled by a 8-bit register (values from 0 to 255) which control each specific central frequency.

3.3.1 Evaluation of different indicators³

Considering that previous tests performed in our laboratories established that the optimum tuning of the filter corresponds to a configuration code number equals to 210, seven different clutter analysis have been obtained by intentionally varying that code number between 175 to 235 (**Figure 3.8 - left**).

For each code values of the receiver filter, radar observations are collected for a time period of approximately two hours during clear sky days: about 120 clutter maps have been acquired, considering that the radar provide a map every minute. All the maps have been acquired in the standard Cartesian format and with the anti-clutter filter disabled. The anti-clutter filter is one of the first post-processing step operatively run in the radar systems, which is able to “clean” rain maps from ground clutter effects. In fact The anti clutter filter implements the ad-hoc routine operatively used, which automatically reject clutter echoes unwanted if it is necessary to detect and measure rain.

Considering the standard radar acquisition mode, each maps contains Digital Numbers (DNs) from 0 to 255 already compensated for the distance. DN's can be related to reflectivity (Z) of ground clutter targets, and possibly to received power, using the standard relations, already reported and explained in **Chapter 2** where the whole data processing chain is described.

The CDFs have been computed on each set of radar clutter maps corresponding to a certain code filter value.

The following statistical indicators characterizing each CDF have been computed in order to find which of that shows the major sensitivity to the detection of radar calibration issues:

- 50 percentile (50^{th}), blue dots in **Figure 3.8 - right**;
- 90 percentile (90^{th}), red dots in **Figure 3.8 - right**;

³ The results presented in this paragraph have been published in: S. Bertoldo, L. Bracco, R. Notarpietro, M. Branca, M. Gabella, C. Lucianaz, O. Rorato, M. Allegretti, G. Perona, *Clutter analysis to monitor the stability of a portable X-band mini weather radar*, Urban Rain 2012 - 9th International Workshop on Precipitation in Urban Areas, pp. 171-176, St. Moritz, Switzerland, December 6th – 9th 2012.

- *Scatter (scatter)*, black crosses in *Figure 3.7 - right*: this is an indication of the “averaged” dispersion around the 50th percentile and it is evaluated as $(84^{th} + 16^{th})/2$;
- *84 percentile – 50 percentile* ($84^{th} - 50^{th}$), red crosses in **Figure 3.8 - right**;
- *50 percentile – 16 percentile* ($50^{th} - 16^{th}$), cyan crosses in **Figure 3.8 - right**: these last two indications allow to identify how asymmetric the dispersion around the 50th percentile is;
- *Asymmetry (asymmetry)*, green crosses in *Figure 3.7 – right*: it is evaluated as the difference between $(84^{th} - 50^{th})$ and $(50^{th} - 16^{th})$;
- *50th percentile – maximum 50th percentile* ($50^{th} - \max(50^{th})$), blue circles in **Figure 3.8 - right**;
- *90th percentile – maximum 90th percentile* ($90^{th} - \max(90^{th})$), red circles **Figure 3.8 - right**: these last two indicators shows the sensitivity to clutter intensities variations because of de-tuning.

The first analysis shows that among all the computed statistical indicators (**Figure 3.8 - right**) the most sensible with respect to the receiver filter detuning seems to be the 90th percentile (and the variation of 90th percentile with respect its maximum value observed when the filter is synchronized with the transmitted signal frequency).

3. Use of ground clutter echoes to monitor the X-band mini weather radar stability

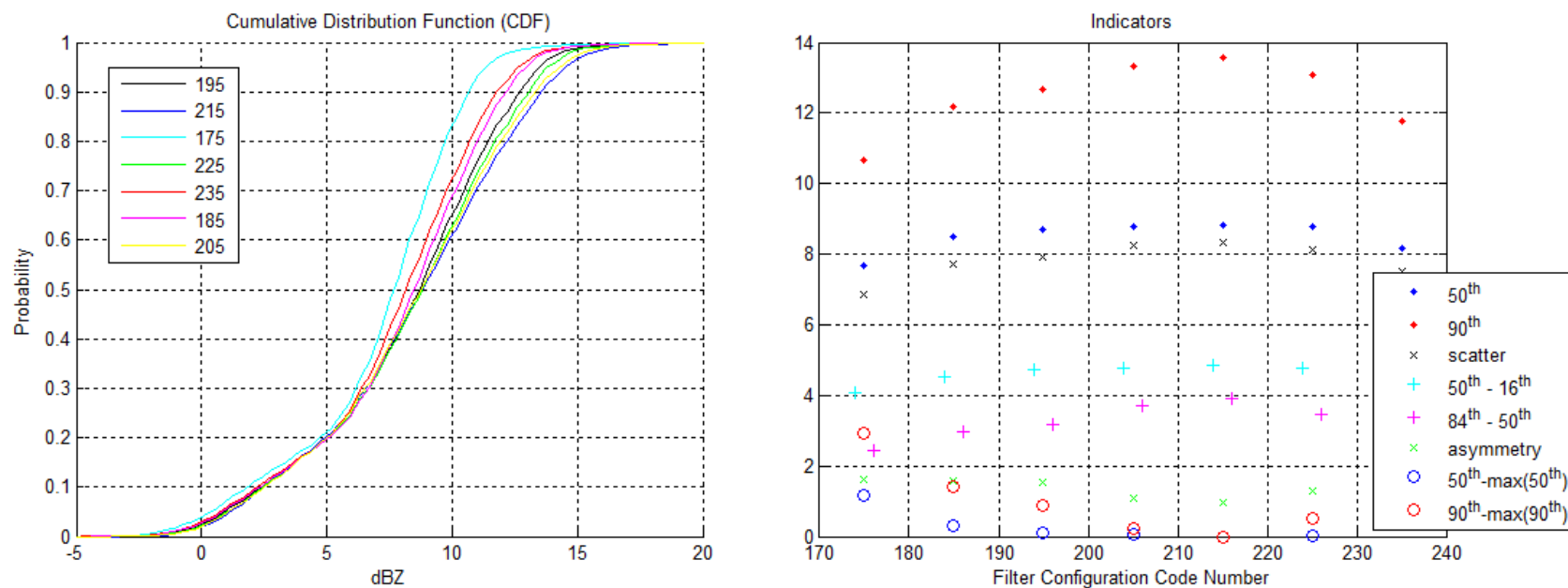


Figure 3.8. CDF for different values of filter configuration code (on the left) and different statistical indicators (on the right).

3.3.2 More detailed analysis on clutter maps and characterization of the radar receiver filter using ground clutter echoes⁴

Even if ground clutter echoes are useful to control the system degradation, a more detailed statistical analysis of ground clutter echoes and a fully characterization of the receiver filter are however necessary to improve the radar stability control algorithm performances. In particular it is necessary to know what is the connection between a single encoder value and the corresponding filter frequency shift. Moreover it is necessary to identify the most suitable clutter type for the analysis acquired by a single radar (e.g hills clutter, mountains clutter, urban clutter...) and then to map the filter response in relation to the encoder value.

The analysis was performed to ground clutter data acquired by the Turin's radar where a quite high number of radar bins are contaminated by ground clutter echoes. Three areas were selected for the statistical analysis of clutter returns (**Figure 3.4**): "Urban Clutter" which can be observed considering the area highlighted in blue, "Hill Clutter" coming from areas highlighted in red and "Mountainous Clutter", characterizing the green area.

Remembering that optimum tuning of the filter corresponds to a configuration code number equals to 210, eleven different analysis were performed, intentionally varying the register code number between 160 to 255 and consequently detuning the radar receiver.

For each value of the encoder, radar observations are collected for a time period of approximately two hours: about 120 different clutter maps are using in the non-standard acquisition mode for raw Cartesian format thus allowing more details in each maps and avoiding any processing steps. In fact a Cartesian map is made by 4096 rows corresponding to encoder positions and 2048 columns corresponding to radar bins.

⁴The results related to the characterization of the receiver filter using ground clutter echoes and the detailed statistical analysis are published in: S. Bertoldo, R. Notarpietro, M. Branca, G. Dassano, C. Lucianaz, O. Rorato, M. Allegretti, *Characterization of the receiver filter of a X-band weather radar to improve the performance of an application to control the radar stability*, IEEE ICEAA 2013, Torino (ITA), 9-13 September 2013, pp. 935-938

Each acquire map contains Digital Numbers (DN). The processing of each map of the dataset is the reported in the following.

- DN are transformed into received power exploiting the receiver law:

$$DN = \left(100 + P_r^{[dBm]} \right) \cdot 2.55 \quad (\text{eqn. 3.2})$$

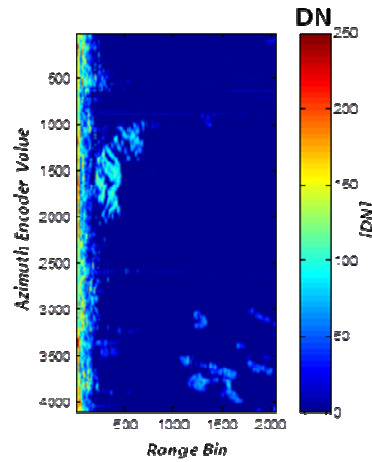


Figure 3.9. DN of an example of Cartesian radar clutter map acquired by the radar in Turin.

- Received power can be expressed considering the radar equation for meteorological target:

$$P_r = k \cdot \frac{Z}{R^2} \quad (\text{eqn. 3.3})$$

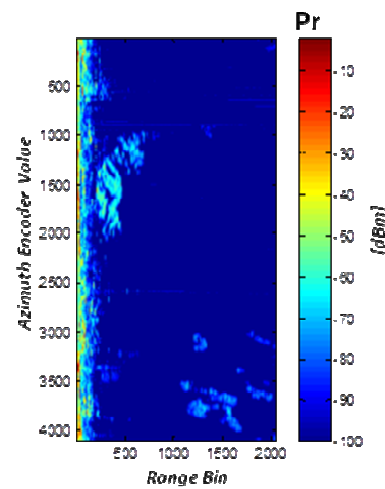


Figure 3.10. Transformation in received power (dBm) of an example of Cartesian radar clutter maps acquired by the radar in Turin.

- The backscattered power contribution (in dBm) coming from each ground clutter pixel is then compensated for space attenuation due to distance (R):

$$P_r + 20 \cdot \log_{10} R \quad (\text{eqn. 3.4})$$

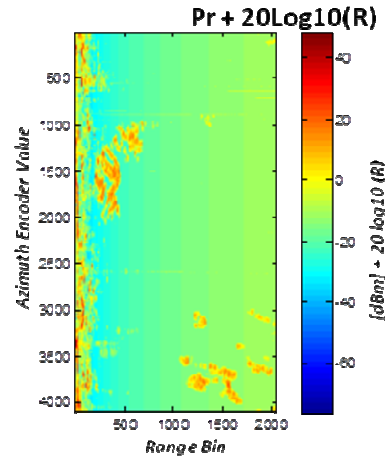


Figure 3.11. Example of Cartesian radar clutter maps acquired by the radar in Turin compensated for the attenuation due to the distance.

As already stated before, three clutter areas with different clutter type can be identified considering the radar installation in Turin: the “Urban Clutter” area, the “Hill Clutter”, the “Mountainous Clutter” area (Figure 3.4, Figure 3.12). They have been all selected for the statistical analysis of clutter returns.

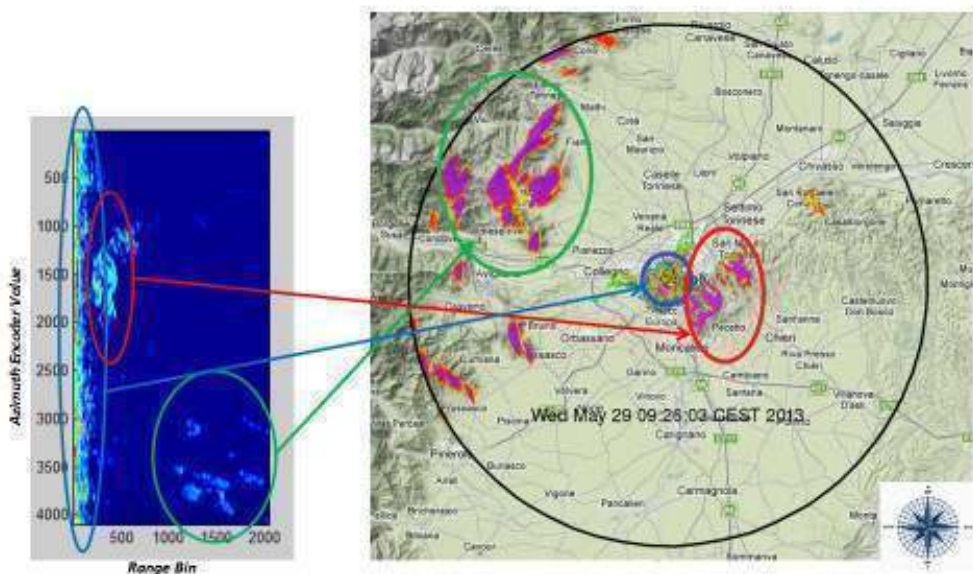
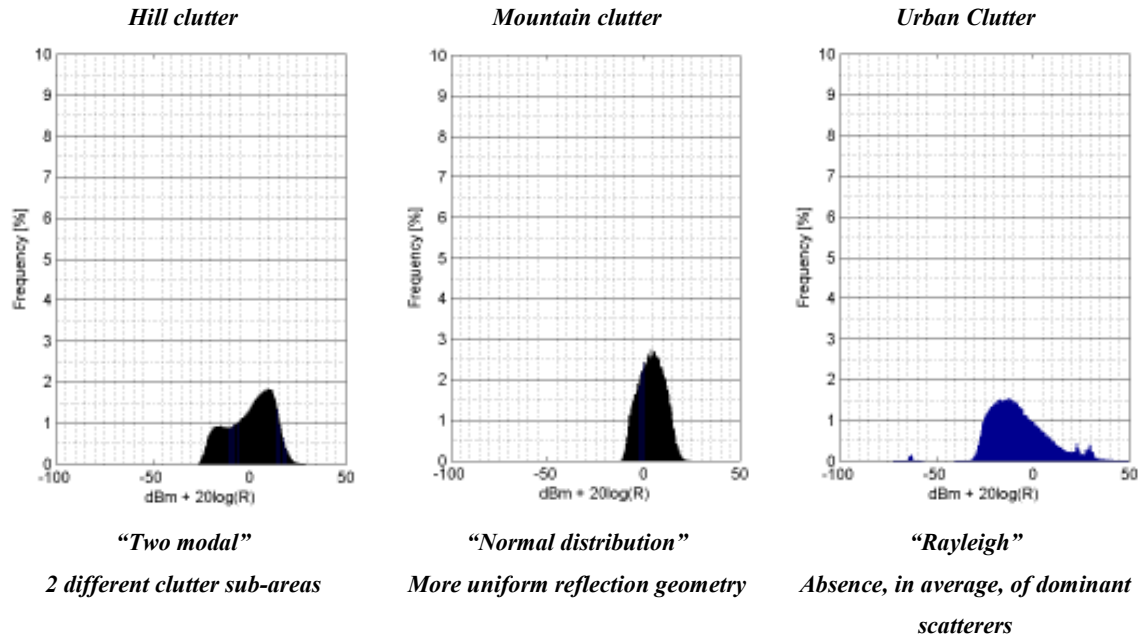


Figure 3.12. Clutter areas for Turin radar in both polar and Cartesian radar map.

Considering all the different receiver filter code values, the echoes power distribution have been computed.

Table 3.1. Clutter echoes power distribution for different types of clutter



Looking at those distributions (**Table 3.1**), some results can be highlighted: hill clutter power distribution is two-modal: this is probably because the area which characterize such clutter type includes two different clutter sub-areas. The closest one to the radar for which “back scattering” is more likely to happen, and a farthest one for which incidence is hardly normal, and lower backscattered power values are expected. The Urban clutter shows a distribution similar to the Rayleigh one (this is a reasonable distribution due to absence, in average, of dominant scatterers inside the analyzed area). Finally, a normal power distribution for the mountainous region (green area) is also reasonable, thanks to a more uniform reflection geometry which characterize such farthest clutter area.

The statistical indicators reported in the **section 3.3.1** are evaluated considering the overall distributions of power values coming from pixels belonging to the three areas (Urban, Hill, Mountainous). Each distribution is created considering the power received detuning the radar for each value of the encoder (ranging from 160 to 255,

with a step of 10 values), for a time period of about 2.5 hours. As already described among all the computed statistical indicators the most sensible with respect to the receiver filter detuning seems to be the 90th percentile.

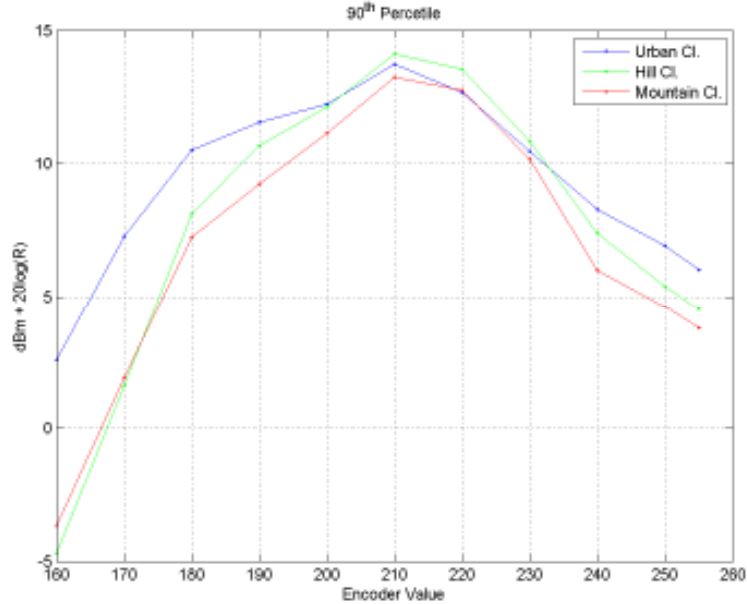


Figure 3.13. Variation of the clutter power 90th percentile indicator in function of the receiver filter code value. Urban/Hill/Mountainous Clutter types are shown using blue/red/green color codes.

In **Figure 3.13**, 90th percentile is shown for each encoder value. Considering each clutter type three plots are superimposed, considering the three different 45 minutes time intervals on which the entire dataset has been divided.

As it is clear from **Figure 3.13**, statistics are consistent for the three 45 minutes dataset. In what follows, only the last 45 minute time interval will be further considered. Moreover, the “filter” response of the radar receiver is also easily defined and, as it is possible to note, the encoder value for which the radar receiver is tuned is 210. It is also confirmed that the 90th percentile power level is quite sensitive to the clutter type, in particular when the radar is de-tuned. For Urban Clutter this is higher than for the other cases.

To better characterize the clutter statistics, a single parameter (the 90th percentile) could be not enough (in particular considering the distributions shown in **Table 3.1**). That is clear also plotting the CDFs evaluated considering different clutter

types and different encoder values. Such CDFs are shown in **Figure 3.14** for receiver filter code values from 160 to 210 and in Figure 3.15 for values from 210 to 255. Colour codes are “symmetric” with respect the one for which the radar is supposed to be tuned.

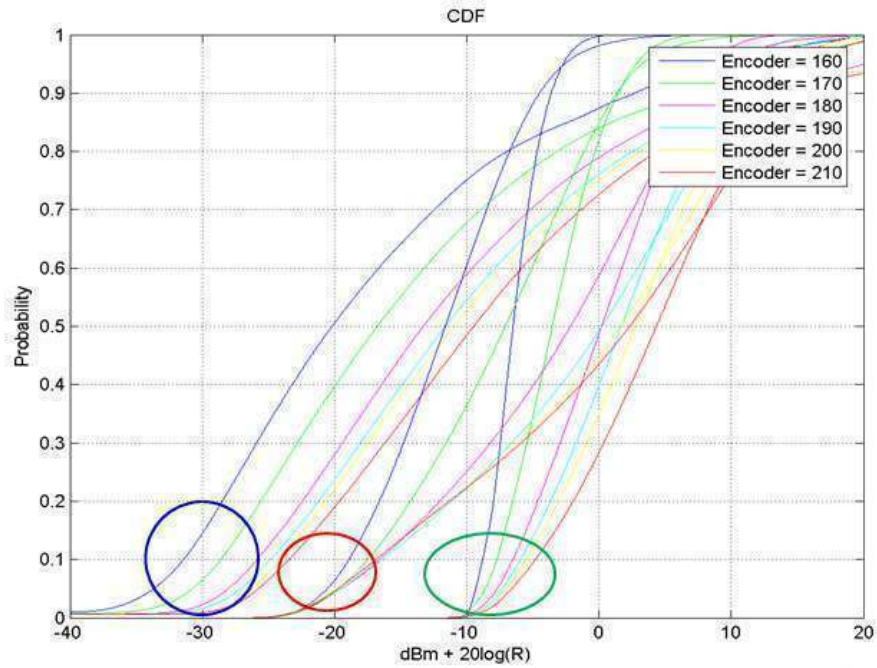


Figure 3.14. CDFs for receiver filter code value from 160 to 210.

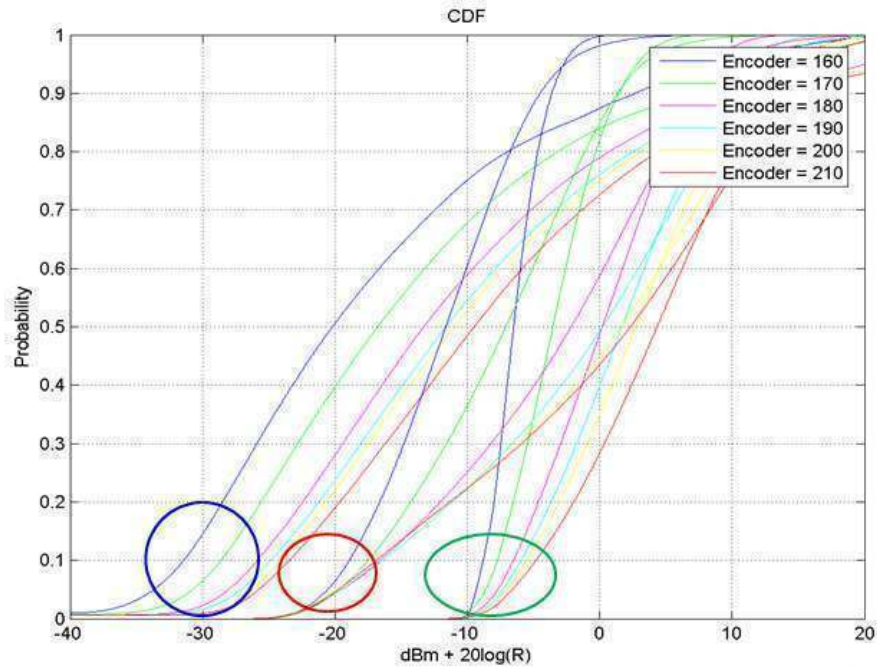


Figure 3.15. CDFs for receiver filter code value from 210 to 255.

The sensitivity of such CDFs to clutter type is clearly visible. Even if the 90th percentile is a good indicator to define the radar de-tuning, it is not enough to clearly separate the three clutter types. Other indicators, such as for instance, the *mean* and the *median*, seem to be more sensitive to clutter types.

The following **Figure 3.16** shows the *mean* and *median* power indicators in function of the encoder value, for the three clutter types. Taking into account for instance the mean value when radar is tuned it is possible to observed about 5 dB difference between mean power coming from Mountainous Clutter and Hill Clutter, and about 12 dB from Mountainous and Urban clutter. It is possible to plot the filter response with respect to the encoder value.

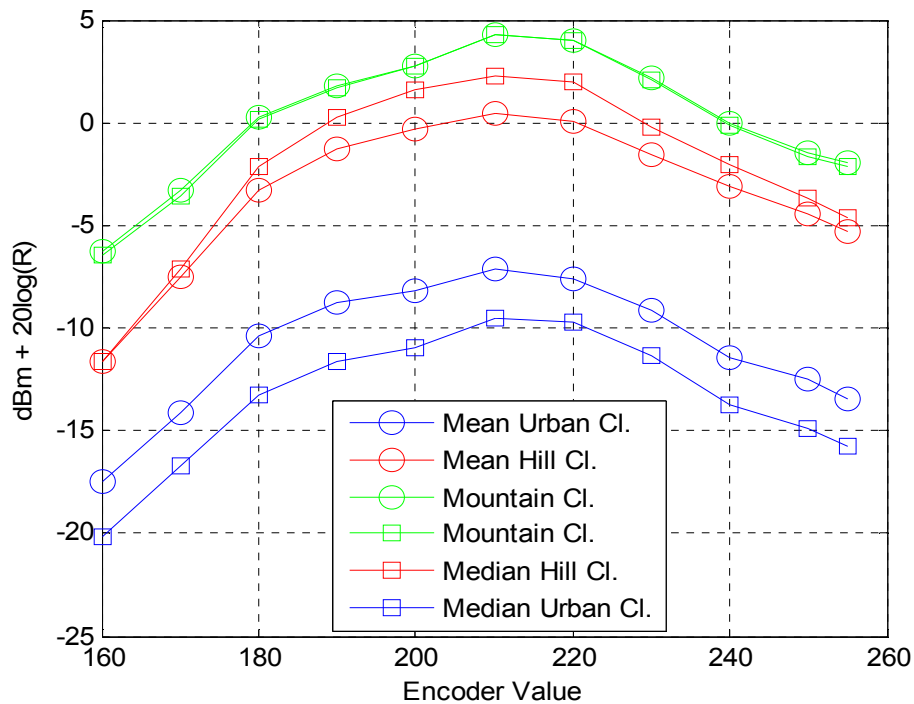


Figure 3.16. Mean and median for different clutter types with respect to different encoder values.

3.4 A standalone application to monitor the radar stability using ground clutter echoes

As already described in the previous section, clutter echoes together with some good statistical indicators can be used to monitor the radar stability. On the basis of the analysis of clutter maps, a standalone application to monitor the stability of the X-band weather radar developed by RSG has been developed⁵. It uses the ground clutter echoes coming from a large number of targets, acquired during clear sky day. Ground clutter maps are acquired by a radar system with anti-clutter filter disabled and are analyzed in the standard Cartesian format. The software analysis gives in output an indication of the overall calibration of the system and, if necessary, suggests a correction factor for the calibration of the weather radar.

The applications is run periodically by the expert user of the radar and it is made by two software modules:

- the clutter maps acquisition module
- the processing module.

At the end of each analysis, a web server installed on the radar control unit allows to display the results in a dedicated web page, accessible to authorized users by connecting directly on the IP address of the system. The results are also available on text files, useful for post processing.

As The X-band mini weather radar is completely maintenance free, the presented application allow users to control the radar stability without complex instruments. An authorized user can check the radar stability by only connecting to the radar control pc with a remote connection without altering the normal radar operation. In fact the control application can be run in a transparent way, in parallel with the standard operational software for rain estimation.

⁵ The description of the application have been presented at ICEAA 2012 in: S. Bertoldo, L. Bracco, R. Notarpietro, C. Lucianaz, O. Rorato, M. Allegretti, *A standalone application to monitor the radar stability of a low cost maintenance free X-band mini weather radar, using ground clutter echoes*, International Conference in Electromagnetics in Advanced Applications, pp. 1040-1043, Cape Town, South Africa, , September 2nd – 7th, 2012. The application has been developed before the detailed clutter analysis because its high configurability allow users to change the computed statistical indicator easily by simply modifying the configuration file.

Moreover the application is included in the standard radar package software and it is possible to automatically apply the eventual correction factor suggested by the application, directly on the rain maps acquired by the radar, by simply reboot the entire radar system at the end of the analysis.

3.4.1 Clutter maps acquisition module

The clutter maps acquisition module is very similar to the radar control software which is used to acquire the standard radar maps. As the application requires clutter echoes, the anti-clutter filters are disabled. Output of this first module is the clutter map, which is therefore acquired every minute. It is stored in a temporary folder waiting to be processed by the elaboration module.

Accordingly to the radar standard acquisition technique, it has to be noted that each pixel of the Cartesian map has a “virtual” dimension of 60×60 square meters: of course only the original physical range resolution is of the same order (approximately 90 m) while the average range resolution is much larger (at 30 km range it is approximately 1500 m). However, this is enough for the application presented in this work as well as for meteorological purposes related to environmental monitoring and natural hazard prevention, in particular for what concern civil protection, traffic monitoring and agro-meteorology.

A qualified user can set, trough a configuration file, how much time the clutter map acquisition module should run, in order to generate an acceptable number of clutter maps for further processing. For a good analysis this time interval must be set at least equal to 24 hours, thereby ensuring that all minor clutter fluctuations should have been detected.

3.4.2 Processing module

The core of the application to control the radar stability is the processing module. It starts to work when the acquisition of the clutter maps is completed. It processes all the maps stored in the temporary folder by the acquisition module, it gives in output a text

file containing the results, and, concerning long term period analysis, it evaluates the potential calibration coefficient.

The long term period analysis evaluates some statistics, and in particular the 90th percentile and the median values, of the clutter related to all the time interval set by the user. If the analysis has been already performed at least one time before, an indication of the correction factor needed by the radar for a potential calibration is given. The output file contains the clutter reflectivity Cumulate Distribution Function (CDF) values, the statistical indicators and gives an indication of the potential correction factor needed to keep the radar calibrated.

The first reference value is the 90th percentile clutter magnitude value evaluated immediately after the X-band radar installation, and the calibration coefficient is computed each time considering the difference between the last two mean values obtained from two consecutives long term analysis.

4.

Quantitative Precipitation Estimation (QPE)

4.1 Introduction to QPE

The present chapter presents some hourly radar-derived precipitation amounts as obtained from weather echoes aloft to be compared with point rainfall measurements acquired at the ground by rain gauges.

It is to point out that radars and gauges have different spatial resolution. In fact, as shown in **Figure 4.1**, a rain gauge perform a punctual measurement of the amount of rain fallen on the ground, while the radar perform a volumetric measurement of a quantity called *Radar Reflectivity* which is not only related to the drops inside a single volumetric cell monitored by the radar. The Radar Reflectivity is related to all the hydrometeors contained inside the volumetric cell including water, snow, hail etc. Moreover you have to consider that the radar monitored cell increase with the distance. As shown in **Figure 4.2**, at a distance of 15 km from the radar, the cell has a volume of 0.04 km^3 , which is much bigger if compared with the punctual measurement made by the gauge (over an area of almost 314 cm^2).

Aim of the QPE is to make the radar measure the rain fallen on the ground in the best way possible, because what is important for people, farmers, workers, civil protection institutions etc., is to have a good estimation of the rain on the ground, in order to plan their activities and perform monitoring operations.

In the cases presented here in the following, the scope of our QPE analysis is twofold:

- to evaluate from an hydrological point of view the radar ability in discriminating wet versus dry hours;
- to quantitative assess the radar accuracy in estimating hourly rain rates.

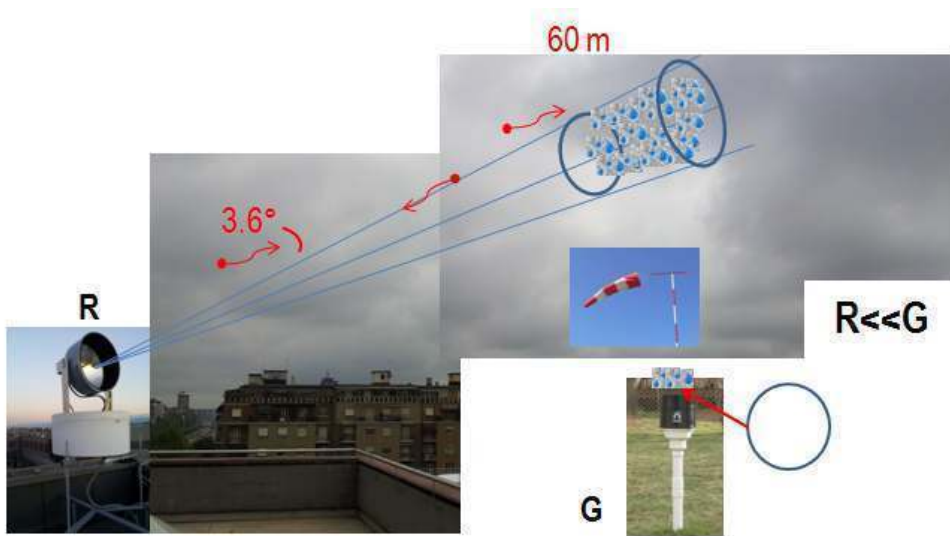


Figure 4.1. Differences between rain gauges and radar.

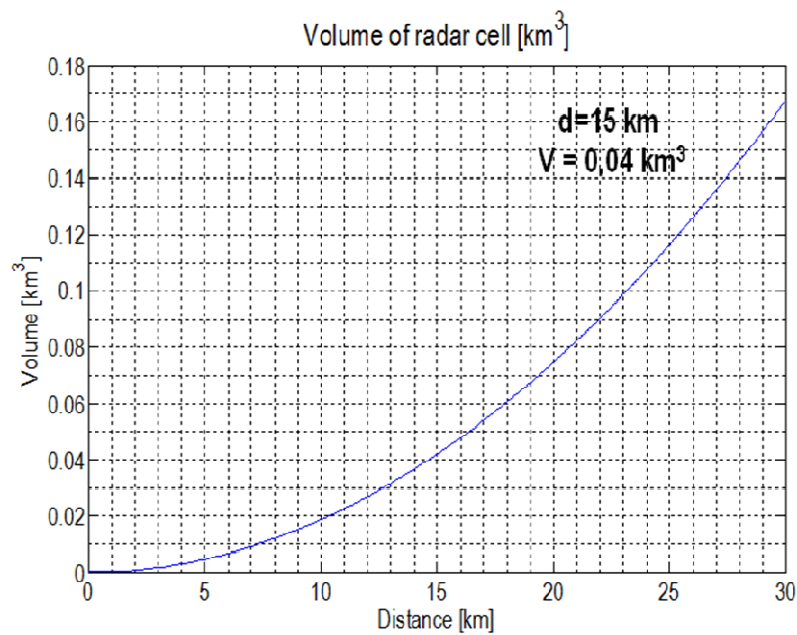


Figure 4.2. Volume of the radar cell in function of the distance from the radar.

In **Chapter 1** it is already reported the theoretical background and how it is possible to obtain the rain estimation using a radar ad measuring the reflectivity.

4.2 QPE with radars installed in Sicily Region¹

QPE techniques have been applied at first at the radars installed in the Sicily Region, in the southern part of Italy. In particular, in Sicily, the radar of Palermo and Bisacquino (PA) have been considered.

4.2.1 QPE evaluation based on the comparison between hourly radar and gauge rainfall amounts

Considering the first QPEs of the radar installed in Palermo and in Bisacquino (PA), the evaluation is based by looking at the average value and the dispersion of the errors (here the *error* is the disagreement between radar and gauge amounts). For such characterization, we define the two following parameters:

1. *Bias (in dB)*. The bias in dB is defined as the ratio between radar and gauge total precipitation amounts on a logarithmic (decibel, dB) scale. It describes the overall agreement between radar estimates and ground point measurements. It is averaged over the whole space–time window of the sample. A positive (negative) bias in dB denotes an overall radar overestimation (underestimation).
2. *Scatter (in dB)*. The definition of scatter is strictly connected to the selected error distribution from a hydrological (end-user) and radar meteorological (operational remotely sensed samples of the spatio-temporal variability of the precipitation field) perspective. The error distribution is expressed as the cumulative contribution to total rainfall (hydrologist point of view, y axis) as a function of the radar–gauge ratio (radar-meteorologist point of view, x axis). Most of the sources of error in radar precipitation estimates, in fact, have a multiplicative (rather than an additive) nature. An example of the error

¹The results reported here in the section 4.2 are published in the book chapter: M. Gabella, R. Notarpietro, S. Bertoldo, A. Prato, C. Lucianaz, O. Rorato, M. Allegretti, G. Perona, *A Network of Portable, Low-Cost, X-Band Radars*, in *Doppler Radar Observations - Weather Radar, Wind Profiler, Ionospheric Radar, and Other Advanced Applications*, Dr. Joan Bech (Ed.), InTec, 2012.

distribution is shown in a paper of Germann et al. presented in 2004². The scatter is defined as half the distance between the 16% and 84% percentiles of the error distribution. The scatter refers to the spread of radar–gauge ratios when pooling together all volumetric radar estimates aloft and point measurements at the ground.

From the radar-meteorological point of view the multiplicative nature of the error prevails with respect to the additive one. For example, water on the radome, a wrong calibration radar constant, or a bad estimate of the profile all result in a multiplicative error (i.e. a factor) rather than an additive error (i.e. a difference). This is why bias, error distribution and scatter are expressed as ratios in dB. A 3 dB scatter, for instance, means that radar–gauge ratios vary by a factor of 2. If bias is zero, it is interpreted as follows: the radar-derived estimate lies within a factor of 2 of the gauge estimate for 68% of rainfall while for the remaining 32% the uncertainty is larger. The scatter as defined above is a robust measure of the spread. It is insensitive to outliers for two reasons. First, each radar–gauge pair is weighted by its contribution to total rainfall (y axis of the cumulative error distribution). An ill-defined large ratio that results from two small values, e.g. 0.4 mm/2 mm ~ -7 dB, describes an irrelevant event from a hydrological point of view, and only gets little weight. Second, by taking the distance between the 16% and the 84% percentiles, the tails of the error distribution are not overrated. Another important advantage of the spread measure is that it is unaffected by the bias error, hence providing a complementary view of the error in the estimates. The above definition of the scatter is thus a better measure of the spread than the less resilient standard deviation.

4.2.2 QPE for the Palermo radar

The Palermo radar is located on a small hill next to the harbor of the capital of Sicily (blue triangle, **Figure 4.3**): its latitude is 38°.1139, its longitude is 13°.358 and its

²Germann U., Galli G., Boscacci M., Bolliger M., Gabella M., *Quantitative precipitation estimation in the Alps: where do we stand?*, Third European Conference on Radar meteorology ERAD2004, 2004, Visby, Sweden, pp. 2-6.

altitude is 45 m above Mean Sea Level (MSL) height. The radar has been installed in autumn 2010 and operative until July 2012.

Table 4.1. Palermo radar coordinates.

Radar	Lat. [°]	Long. [°]	Alt. [m slm]
Palermo	38.139	13.358	43

For the quantitative evaluation of the radar estimates, the most reasonable available rain gauge in terms of range and radar visibility is the one located in Altofonte. It is run by the Servizio Informativo Agrometeorologico Siciliano (SIAS). Its location is the red triangle in **Figure 4.3** which represents a 90 m resolution Digital Elevation Model of the region at two different scales: left picture domain is almost 540 by 540 km² while right picture is 90 by 90 km².

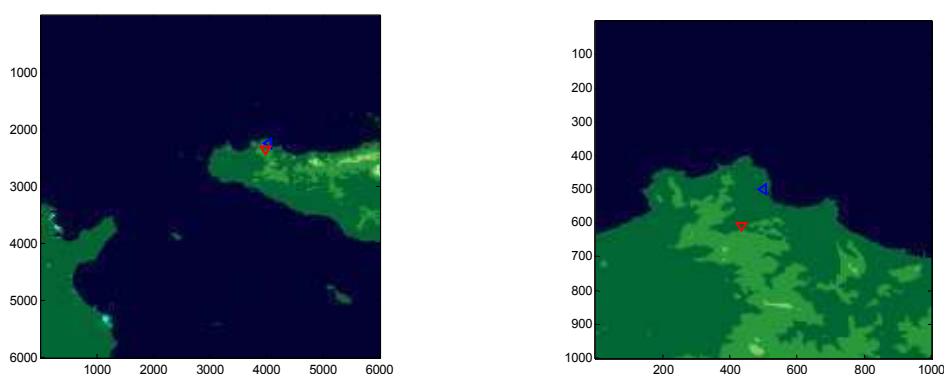


Figure 4.3. Digital Elevation Map of Sicily showing two different domains (pixel size is 90 m); the blue triangle shows the mini radar site next to Palermo down town. The red triangle shows the location of the most reasonable rain gauge in terms of range and radar visibility; this gauge (Altofonte, PA) has been used for the QPE evaluation.

The radar-gauge distance is 11.1 km; the rain gauge altitude is 370 m above MSL. **Figure 4.4** shows the radar-gauge profile as derived using the DEM shown in **Figure 4.3**. In addition to the terrain profile (black curve), the picture shows the mini-radar 3.6° HPBW by means of two blue lines. The radar beam axis, which divides such angular sector in two equal parts of 1.8°, has an angle of elevation equal to +3°. As it can be seen from **Figure 4.4**, the gauge location is not optimal: in fact in the last kilometer before the gauge, the 3 dB portion of the primary lobe hits the hilly terrain,

hence causing some power loss and ground clutter contamination. However, regarding this last problem, it is worth noting that the rain gauge location is behind the top of the hill: this means that Palermo radar echoes above the Altofonte gauge are practically ground-clutter-free; nevertheless, as stated, because of beam shielding, some radar underestimation above the gauge can be expected.

For what concerns QPE, 6 rainy days (144 hours) during the first 4 months of 2011 have been analyzed; these days are February 1, 23 and 28, March 5, April 26 and 27. During these 144 hours the Gauge (Radar) total amounts was 77.4 (62.7) mm, which corresponds to an “overall Bias” of -0.9 dB (radar underestimation). Out of 144 analyzed hours, in 48 (42) cases the Gauge (Radar) derived hourly rainfall amount was larger than 0.4 mm/h, which is the hydrological threshold adopted in this section for discriminating between “hydrologically speaking” wet and dry hours.

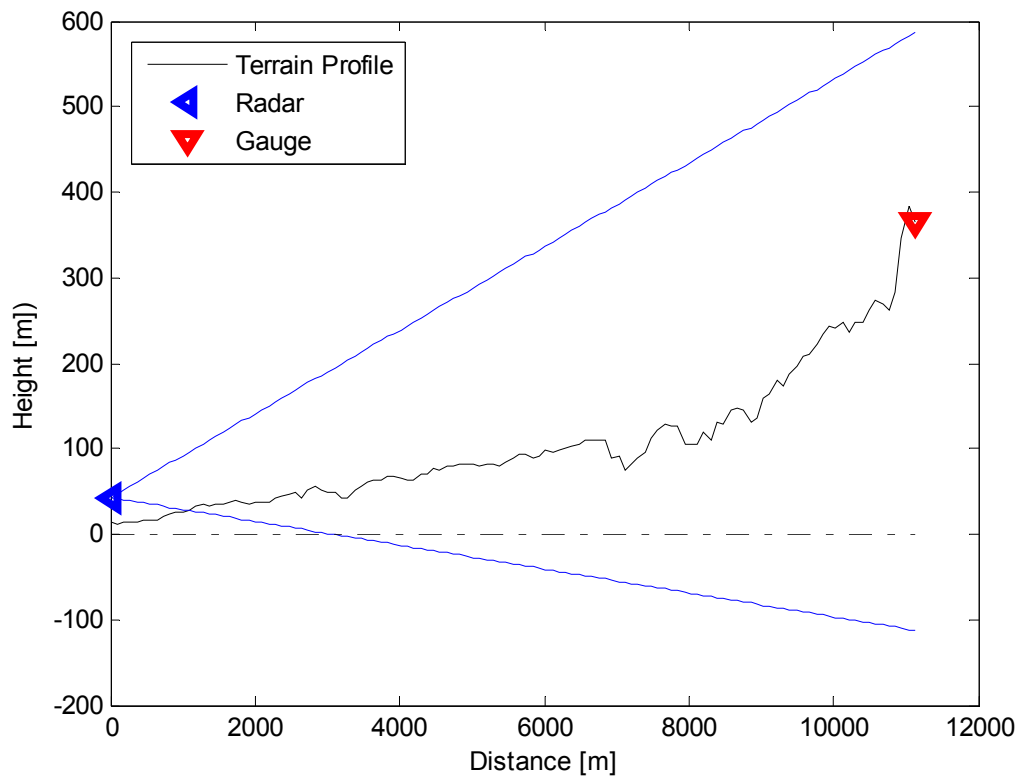


Figure 4.4. Vertical section of the terrain profile from the Palermo radar site to the Altofonte (PA) gauge. The blue lines indicate the boundaries of the radar antenna HPBW.

4.2.3 Wet versus dry hours discrimination according to radar echoes using the gauge as reference

The history of applying *contingency tables* (also called *error matrices* in the remote sensing field) for the verification of one set of observations against a reference set is a quite long one.

The dimension of the contingency tables can be as small as 2x2 (tetrachoric) or larger (polychoric) depending on the number of thresholds used in the classification scheme. Obviously, in our wet-versus-dry hourly values discrimination, we are dealing with tetrachoric tables, since just one discrete value (namely 0.4 mm/h) is used to divide the two categories. On the one hand, the properties of a set of observations can be condensed and clearly displayed through such tables; on the other hand, to satisfy needs of specific users, even for a simple tetrachoric table, several different scores have been introduced. Their analysis is out of the scope of the present work and they are not described here.

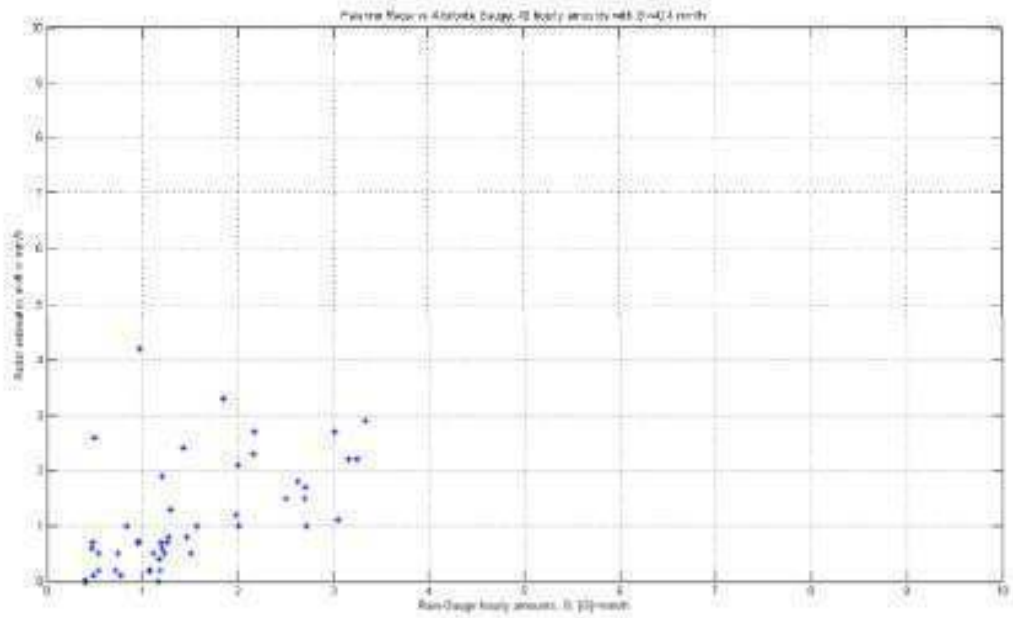


Figure 4.5. Scatter plot of 48 hours with Altofonte gauge amounts larger or equal than 0.4 mm/h and the corresponding Palermo radar estimates. The scale is linear and the maximum value is set to 10 mm/h.

Table 4.2. Contingency table between the Palermo radar estimates and the Altofonte (PA) rain gauge measurements.

	G ≥ 0.4 mm/h	G < 0.4 mm/h	
R ≥ 0.4 mm/h	38	4	42
R < 0.4 mm/h	10	92	102
	48	96	144

From **Table 4.2**, it is straightforward to derive the *Probability Of Detection* (POD) and the *False Alarm Ratio* (FAR):

- POD is $38/48 = 0.79$.
- FAR is $4/42 = 0.095$.

4.2.4 QPE for the Bisacquino (PA) radar

The Bisacquino radar is located in the central-western part of Sicily: latitude is $37^{\circ}.707$, longitude is $13^{\circ}.262$ and altitude is 780 m above Mean Sea Level (MSL) height. As for the Palermo radar it has been installed in autumn 2010 and operative since the beginning of 2012.

Table 4.3. Bisacquino (PA) radar coordinates.

Radar	Lat. [°]	Long. [°]	Alt. [m slm]
Bisacquino	37.707312	13.262147	776

For the quantitative evaluation of the radar estimates there is an optimal rain gauge run by the Servizio Informativo Agrometeorologico Siciliano (SIAS) and installed in the municipality of Giuliana, PA, (località Castellana). Its location with respect to the radar is shown in **Figure 4.6** together with the DEM of the area.

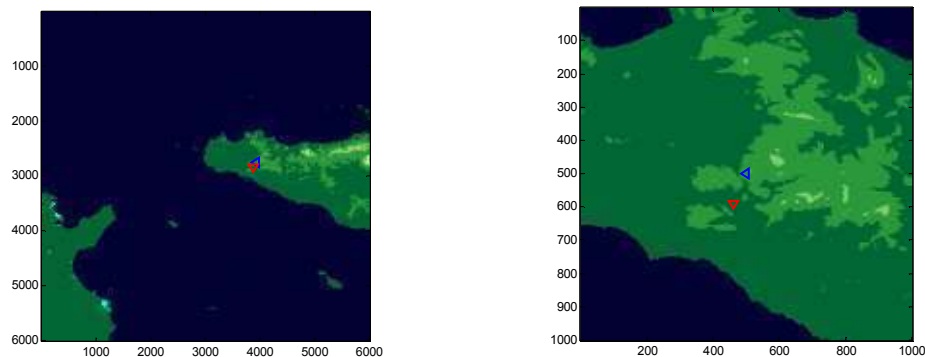


Figure 4.6. DEM of the western part of Sicily showing the Bisacquino (PA) radar site (red triangle) and the Giuliana (PA) rain gauge location (blue triangle).

The radar-gauge distance is 8.7 km; the rain gauge altitude is 250 m above MSL. The gauge location is optimal not only in terms of range, but most of all in terms of radar visibility: no partial beam shielding by relieves affects the mini radar 3.6° HPBW, which is delimited by the two blue lines in **Figure 4.7** (the radar beam axis has an angle of elevation set to 1°). Furthermore, the hill located at 3 km range from the radar, causes partial beam shielding of the remaining part of the primary lobe and total shielding of the secondary lobes in elevation; consequently, we can conclude that residual ground clutter contamination affecting radar echoes above the Giuliana (PA) rain gauge is negligible.

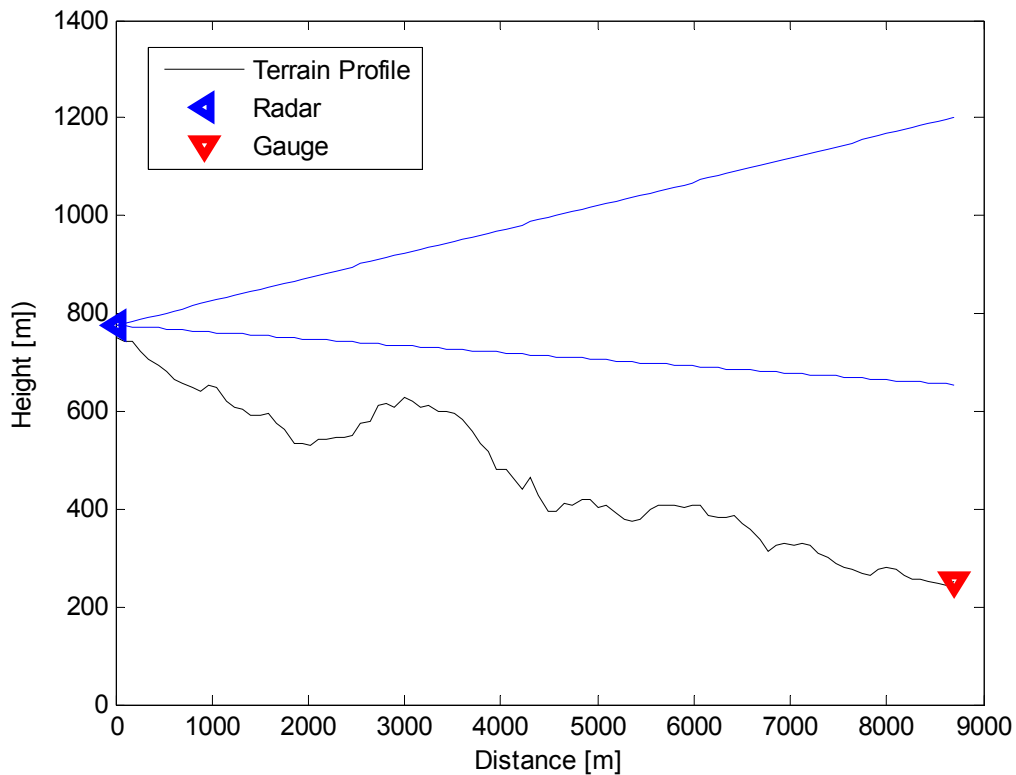


Figure 4.7. Vertical section of the terrain profile from the Bisacquino (PA) radar site to the Giuliana (PA) gauge. The blue lines indicate the boundaries of the radar antenna HPBW.

For what concerns QPE, 4 rainy days (96 hours) during the first 5 months of 2011 have been analyzed; these days are February 23, March 13, April 26 and May 22. During these 96 hours the Gauge (Radar) total amounts was 98.2 (77.7) mm, which corresponds to an “overall Bias” of -1.0 dB (radar underestimation).

Out of 96 analyzed hours, in 37 (34) cases the Gauge (Radar) derived hourly rainfall amount was larger than 0.4 mm/h.

Table 4.4. Contingency table between the Bisacquino (PA) radar estimates and the Giuliana (PA) rain gauge measurements.

	G ≥ 0.4 mm/h	G < 0.4 mm/h	
R ≥ 0.4 mm/h	29	5	34
R < 0.4 mm/h	8	54	62
	37	59	96

From **Table 4.4**, it is easy to see that in this case the POD is (29/37) 0.78 while the FAR is relatively high: (5/34) 0.15.

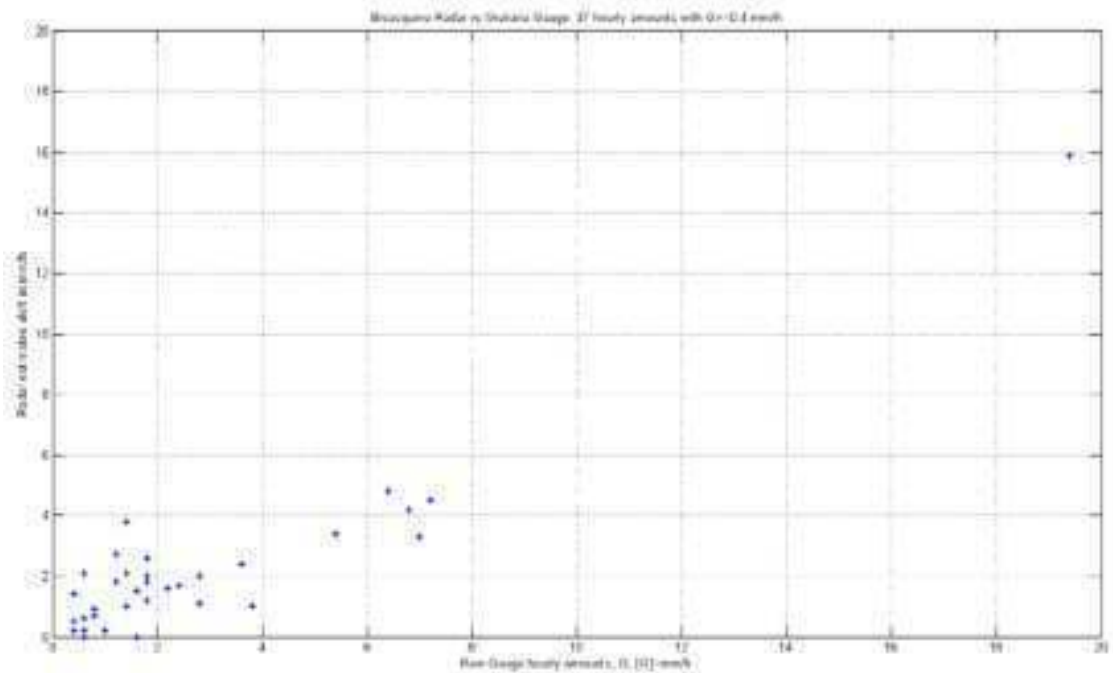


Figure 4.8. Scatter plot of 37 hours with Giuliana (PA) gauge amounts larger or equal than 0.4 mm/h and the corresponding Bisacquino (PA) radar estimates. It is worth noting that in this case the maximum value of the linear scale for the scatter plot is 20 mm/h.

4.2.5 QPE Summary in terms of Bias and Scatter in dB for Palermo and Bisacquino (PA)

For both the radar sites discussed in the previous paragraphs, **Table 4.5** provides a summary of the QPE evaluation in terms of Bias in dB (as a function of the number of considered hours). When all the wet and dry hours are considered, we have the so-called “overall” Bias: it includes False Alarm events (mainly caused by ground clutter contamination) and Missing Detection (caused by beam overshooting, in some cases, attenuation) events; it is certainly the most resistant and complete definition of Bias. It is obviously a measure of the mean error and says nothing about the error dispersion around the mean. For this purpose, there is the Scatter, which will be presented in the **Table 4.6**. While the “overall” Bias (1st column) includes both wet and dry periods, the other two Bias (2nd and 3rd column) are conditional upon rain: the “Wet-Gauge” Bias considers only hours where the gauge amounts are larger than 0.4 mm/h; finally, the definition of “wet-wet” Bias reduces further the number of hours used in the calculus: in such case, only hours with both radar and gauge amounts larger than 0.4 mm/h are used.

Table 4.5. QPE evaluation summary in terms of Bias for three mini-radar sites.

Site	“Overall” Bias	“Wet-Gauge” Bias	“Wet-Wet” Bias
Palermo radar	-0.9 dB (144 hours)	-1.1 dB (48 hours)	-0.7 dB (38 hours)
Bisacquino radar	-1.0 dB (96 hours)	-1.2 dB (37 hours)	-0.9 dB (29 hours)
Torino radar	-0.3 dB (126 hours)	-0.4 dB (63 hours)	+0.5 dB (41 hours)

Table 4.6 summarizes the dispersion of the radar-gauge errors using the hydrological-oriented score called *scatter*. The scatter is defined as a ratio between the Radar (the device under test) and the Gauge (the reference). Hence, dry hours cannot be considered in evaluating the Scatter (unless using some trick, like for instance adding a negligible amount...) Consequently, only “Wet-Gauge” hours or “wet-wet” hours are considered in **Table 4.6**.

Table 4.6. QPE evaluation summary in terms of scatter for Palermo and Bisacquino (PA) radar.

Site	“Wet-Gauge” Scatter	“Wet-Wet” Scatter
Palermo radar	2.38 dB (48 hours)	1.97 dB (38 hours)
Bisacquino radar	1.47 dB (37 hours)	1.31 dB (29 hours)
Torino radar	5.38 dB (63 hours)	3.73 dB (41 hours)

Observing the results above, it can be note that X-band radar are less reliable at low rain rates. By limiting the observations to hours with both radar and gauge amounts larger than 0.4 mm/h, the agreement improves not only in terms of bias, but most of all in terms of scatter. Finally, in the interpretation of these values of both bias and scatter, it is important to bear in mind the large intrinsically different sampling modes as well as mismatches in time of the radar and gauge devices³.

4.3 QPE with radar installed in Turin⁴

The radar installed in Turin is located in Piedmont, North Western part of Italy: its latitude is 45°.063033, its longitude is 7.658513 and its altitude is 253 m above Mean Sea Level (MSL) height. It is the first radar installation has been installed in autumn 2010 and it is still operative.

Table 4.7. Turin radar coordinates.

Radar	Lat. [°]	Long. [°]	Alt. [m slm]
Torino	45°.063033	7.658513	253

The QPE techniques have been applied considering a dataset of rainy events between October and December 2012 and both radar maps and rain gauges data have been acquired. The gauges were made available for free on internet by the service provided by Weather Underground (www.wunderground.com).

³ Zawadzki I., *On radar-raingage comparison*, J. Appl. Meteorol., 1975, Vol. 14, pp. 1430-1436.

⁴ The results presented in this section are published in the following conference proceeding: R. Notarpietro, M. Branca, E. Morin, A. Lokshin, M. Gabella, P. de Vita, B. Basso, D. Bonfil, S. Bertoldo, S. Shah, C. Lucianaz, O. Rorato, M. Allegretti, *Towards sustainable agricultural management using high-resolution X-band radar precipitation estimates*, IEEE ICEAA 2013, Torino (ITA), 9-13 September 2013, pp. 915-918.

Turin area is surrounded by hills. Severe ground clutter impacts on radar estimations. Even though a clutter rejection algorithm runs routinely in the on-board radar processing software (**Chapter 2**), we preferred to select only those rain gauges positioned in “quasi” clutter free areas. Considering also the quality check analysis only 7 rain gauges provided reasonably good rain data for the 13 storms we selected in our dataset. Averaged rain measured by the rain gauges during these 13 storms, both characterizing convective and stratiform events, ranges between 1.4 mm and 16.8 mm.

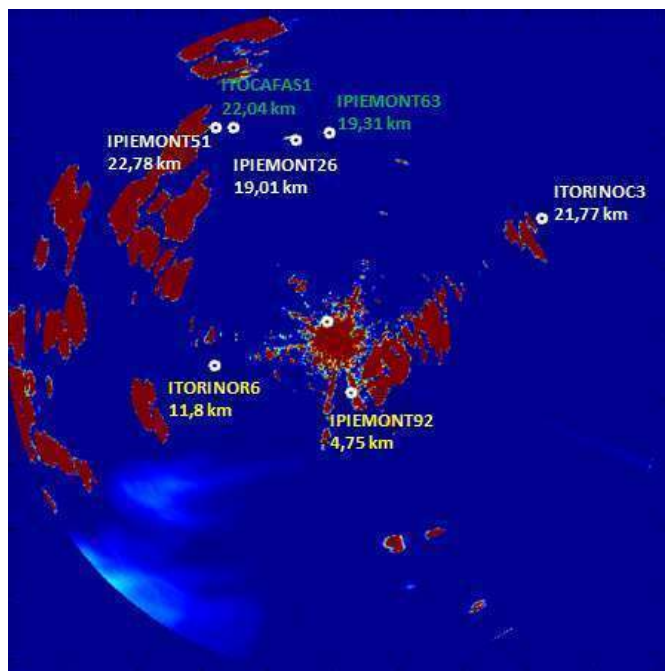


Figure 4.9. Example of a daily cumulated clutter map observed by the Turin radar with superimposed the positions of rain gauges used for the QPE analysis.

4.3.1 CALibration and VALidation procedure (CAL/VAL)

In order to try to improve radar rain estimates, we performed a CALibration analysis exploiting biases between R and G values evaluated on a portion of our dataset, followed by a VALidation analysis carried out considering the other dataset portion. For the Turin case we selected (R, G) CAL couples observed in 4 “control points” (green and yellow points in **Figure 4.9**). In such areas, ground clutter contamination was the minimum one and the radar visibility was pretty good.

The CAL couples for Turin were selected considering all the storms available in the dataset, also including couples for which R or G were equals to 0: 13 storms were considered corresponding to 1872 couples considered; For the yellow control points in the Turin case, only (R, G) couples belonging to odd “hours” were included in the CALibration sub-set.

Considering the (R,G) CAL couples, for each radar we computed the overall bias as:

$$BA = \frac{\sum_{storms_CAL} \sum_{places_CAL} R}{\sum_{storms_CAL} \sum_{places_CAL} G} \quad (\text{eqn. 4.1})$$

Having defined the bias for the CAL sub-sets, we applied this “correction factor” (also called *Bulk Adjustment factor*) equal $1/BA$, to the R values observed by the radar in the remaining VAL sub-sets. These sub-sets, are formed by 5 “control points” (white and values evaluated considering only the “even” hours of the yellow places in **Figure 4.9**) and all the storms.

In order to evaluate the effectiveness of this *Bulk Adjustment* procedure, which is a classical way to provide a correction to radar rain estimates, the following statistical indicators were evaluated considering the couples (R_{BA} , G) of the VAL data-set:

- *residual bias* (which should be close to 0 dB);

$$bias = \frac{\sum_{storms_VAL} \sum_{places_VAL} R_{BA}}{\sum_{storms_VAL} \sum_{places_VAL} G} \quad (\text{eqn. 4.2})$$

- *correlation coefficient corr* between G and R_{BA} (which should be close to 1);

$$corr = \frac{cov(R_{BA}, G)}{\sigma_{R_{BA}} \sigma_G} \quad (\text{eqn. 4.3})$$

- root mean square difference *rmsd* of the $R_{BA} - G$ residuals (in mm/h; it should be as smaller as possible);

$$rmsd = \sqrt{\frac{\sum_{gauges} \sum_{storms} (G - R_{BA})^2}{N}} \quad (\text{eqn. 4.4})$$

- Probability of Detection *POD* and Missing detection *MISS* from the contingency tables.

4.3.2 CAL/VAL procedure results

The following bias (as defined using eqn. 4.1) has been estimated considering the CAL sub-sets: 7.62 (8.82 dB) for the Turin radar.

Complete results are shown respectively in **Table 4.8** for each rain gauge belonging to the VALidation data set. As it is expected, the applied Bulk Adjustment technique improve the residual bias. Of course, it cannot improve the correlation coefficients. Moreover, it has to be noted that CAL and VAL sub-sets are independent only for what concerns the choice of “control points”, and not independent at all for what concerns the storms, since data from all the storms are included in both sub-sets. If there are biases related to time/storms, these biases are present both in the calibration and the validation data sets.

Table 4.8. VAL results for the Turin case. For each gauge, statistical indicators before (first row) and after (second row) the Bulk Adjustment procedure are shown.

Gauge	corr	Bias [dB]	POD %	MISS %	rmsd [mm/h]
ipiemont26	0,79	-8,69	-0,86	-0,28	1,08
BA		0,14	-0,83	-0,22	
ipiemony51	0,70	-9,50	-0,86	-0,38	1,05
BA		-0,67	-0,84	-0,32	
itorinoC3	0,64	-10,06	-0,91	-0,43	1,01
BA		-1,37	-0,89	-0,40	
ipiemont92	0,75	-10,08	-0,55	-0,05	1,46
BA		-1,24	-0,49	-0,04	
itorinoR6	0,90	-7,51	-0,81	-0,17	0,61
BA		1,31	-0,80	-0,15	

Figure 4.10 and 4.11 show respectively the rain estimation before and after the application of the computed BA coefficient for the rain event relative to 28th November 2012. It can be shown a much more better estimation of the rain. That is a good results of improving radar rain estimations using QPE techniques.

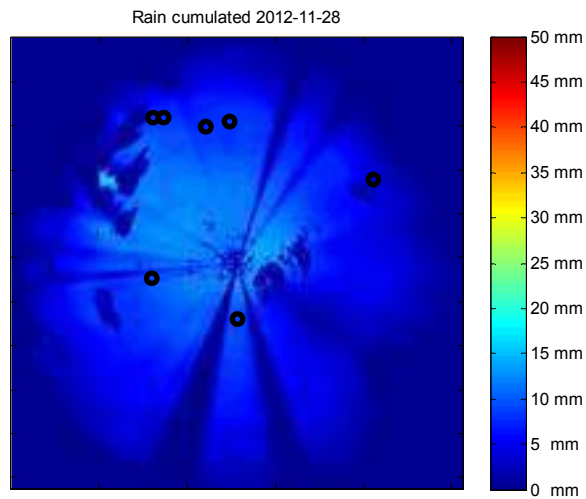


Figure 4.10. Rain cumulated related to 28th November 2012 BEFORE the application of the BA coefficient. Radar of Turin.

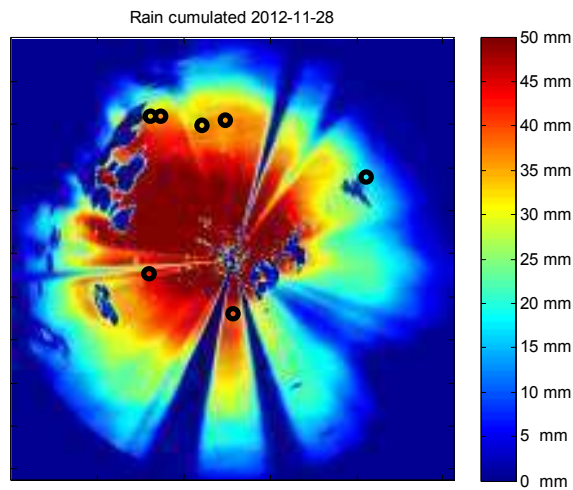


Figure 4.11. Rain cumulated related to 28th November 2012 AFTER the application of the BA coefficient. Radar of Turin.

As already done for the calibration of the radars in Sicily, **Figure 4.12** and **Figure 4.13** represents the scatter plot for the radar installed in Turin, before and after the CAL/VAL procedure.

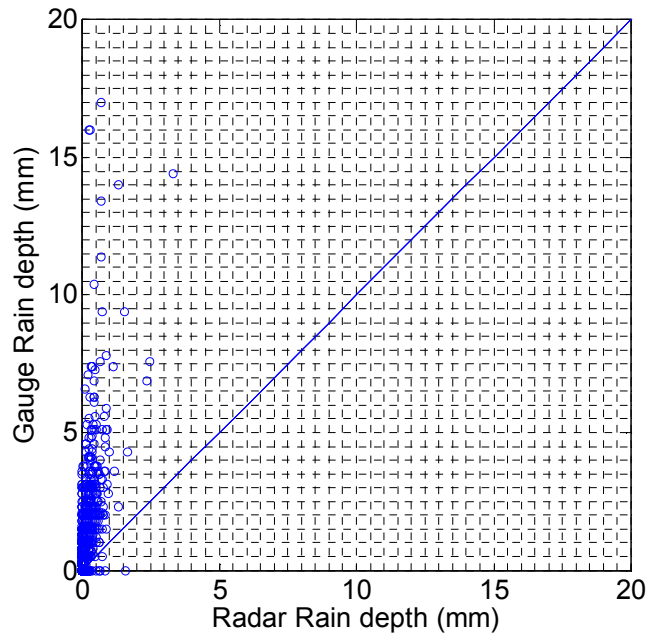


Figure 4.12. Scatter plot BEFORE the application of the BA coefficient. Radar of Turin.

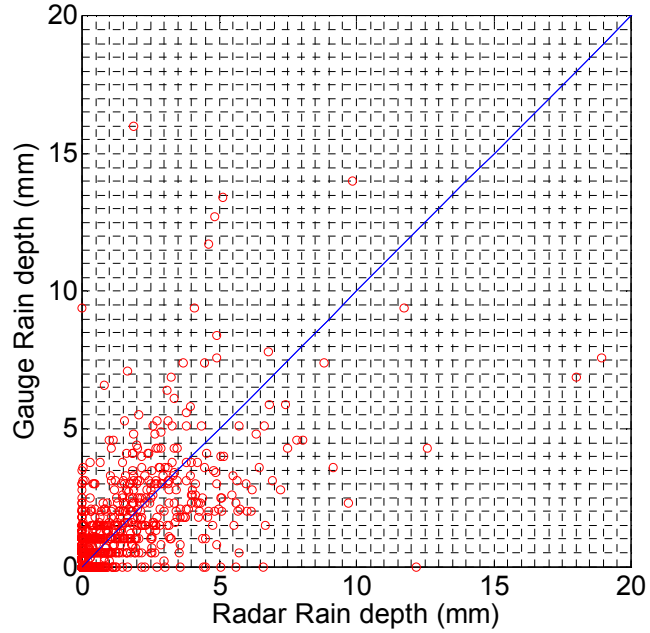


Figure 4.13. Scatter plot AFTER the application of the BA coefficient. Radar of Turin.

In order to show how the radar estimation of rain is improved using the BA coefficient **Table 4.9** shows the statistical indicators evaluated considering only the VAL subsets.

Table 4.9. Statistical indicators evaluated for VAL sub-sets.

corr	Bias [dB]	POD	MISS	rmsd [mm/h]
0,59	0,46	0,71	0,27	0,73

4.4 Some conclusion about QPE

A global analysis of the performances of three small X-band radar meteorological systems installed in different climatological regions (North and South Italy) has been performed. For each radar, biases with respect to independent rain measurements carried out by rain gauges have been evaluated. In particular for Turin radar a procedure named CAL/VAL procedure has been applied. Such procedure, namely Bulk Adjustment, compensates for the average systematic error between radar rain estimates and collocated gauge observations, and can be used to improve (on average) the high resolution rainy maps provided by such small radar systems. Such technique will be better addressed in the future when data from more storms will be available, maybe trying to provide different adjustment factors in function of season or other factors. In addition, the X-band rain induced attenuation has been individuated as a critical issue that should be better addressed. We recognized that its impact is critical in particular when strong events are observed and needs to be deeply studied and compensated (notice the apparent concentric circles in **Figure 4.11**).

5.

Use of X-band mini weather radar: qualitative case studies

5.1 Detecting precipitation inside narrow valley¹

At the beginning of November 2011 (from Nov. 3rd to Nov. 9th around noon) six days of continuous, wide-spread precipitation hit the north-western part of Italy (the Digital elevation map of the area is reported in **Figure 5.1**) In the south-western Alps and in the surrounding flatlands and hills, in fact, autumn is the season in which the longest and heaviest rainfalls occur. It can be explained as follows: in autumn the temperature over the Mediterranean Sea is still high, while cold air is already forming over the central-northern part of Europe. This has two effects: first of all, the thermal contrast facilitates the deepening of pressure low over the north-western part of the Mediterranean Sea; secondly, the warm air that arrives from the south, flowing over the Mediterranean, provides a ready source of moisture.

The enforced rising of this warm-humid “meta-stable” air, thanks to the Alpine barrier, causes extensive and heavy rainfall. One has the impression of being subject to

¹ The following example are reported also in the following book chapter: Gabella M., R. Notarpietro, S. Bertoldo, A. Prato, C. Lucianaz, O. Rorato, M. Allegretti and G. Perona, *A Network of Portable, Low-Cost, X-Band Radars*, Doppler Radar Observations - Weather Radar, Wind Profiler, Ionospheric Radar, and Other Advanced Applications, Ed. Dr. Joan Bech, Intech, 175-202, 2012

a long storm, but, in reality, it is the continuous formation of stormy cells over the same place.

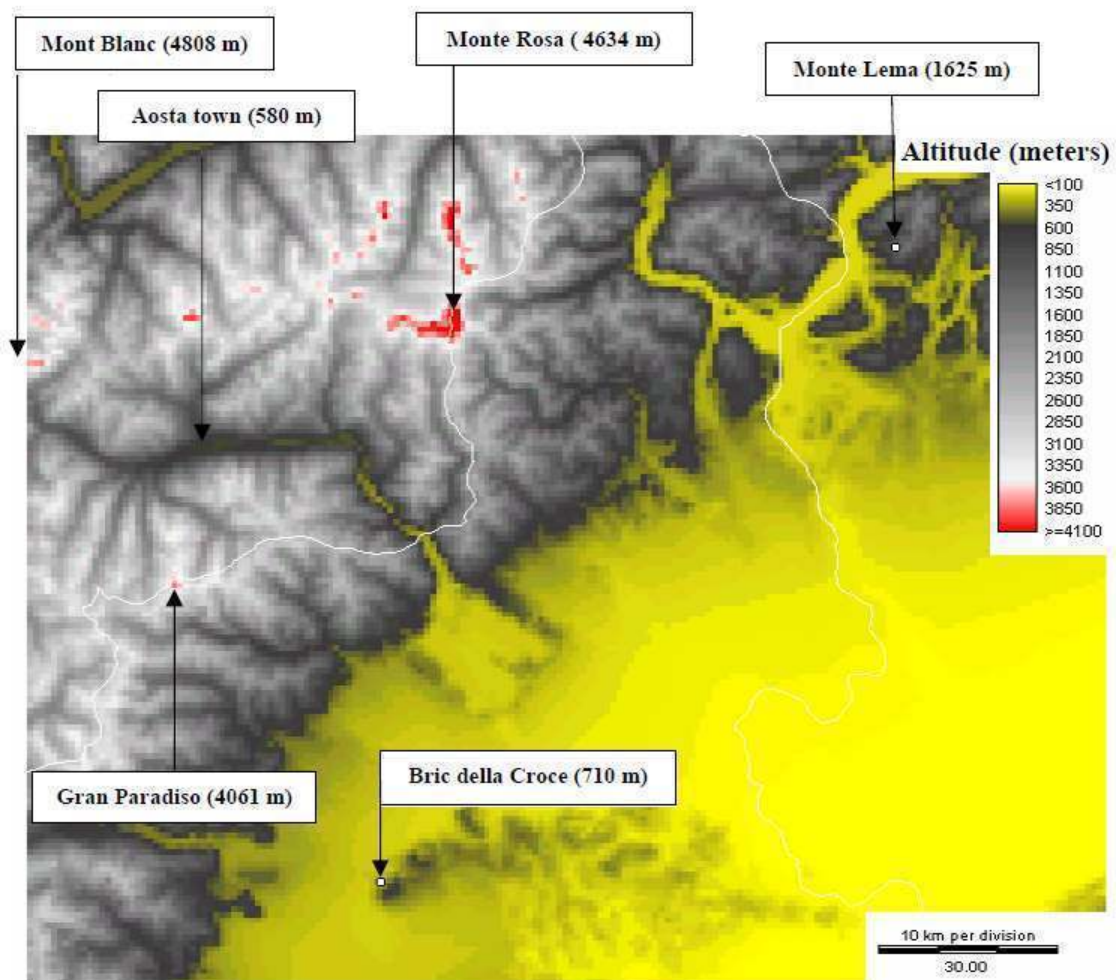


Figure 5.1 Digital Elevation Model of the North-Western part of Italy.

The study site here presented is located in north-western Italy in the “Aosta Valley”, which is the smallest region in Italy. It is set between the Graian and Pennine Alps, which are very steep. Among the more than “four-thousand” massifs, the most famous are: Mont Blanc, Monte Rosa, the Matterhorn and Gran Paradiso. The Dora Baltea river together with its tributaries have formed the tree-leaf-shape veining of the Valley.

Being surrounded by such high relieves (higher than 4000 m MSL), the deep Aosta Valley (lower than 500 m MSL) cannot be effectively monitored by any of the

surrounding weather radars (Dole and Monte Lema, respectively close to Geneva, and to Maggiore Lake owned by MeteoSwiss and Bric della Croce, close to Torino owned by ARPA Piemonte). Among these three radars, the one with “less worse” visibility is certainly Monte Lema, which was the only one able to detect some weak echoes during the 24-hour period shown in **Figure 5.2** (from 12 UTC of November 4 to 12 UTC of November 5). However, because of beam shielding by relieves combined with overshooting, the 24-hour radar-derived rainfall amounts above the central-western part of the Aosta Valley are heavily underestimated: for instance, above Aosta town, the Swiss weather radar network shows amounts smaller than 2 mm in 24 hours.

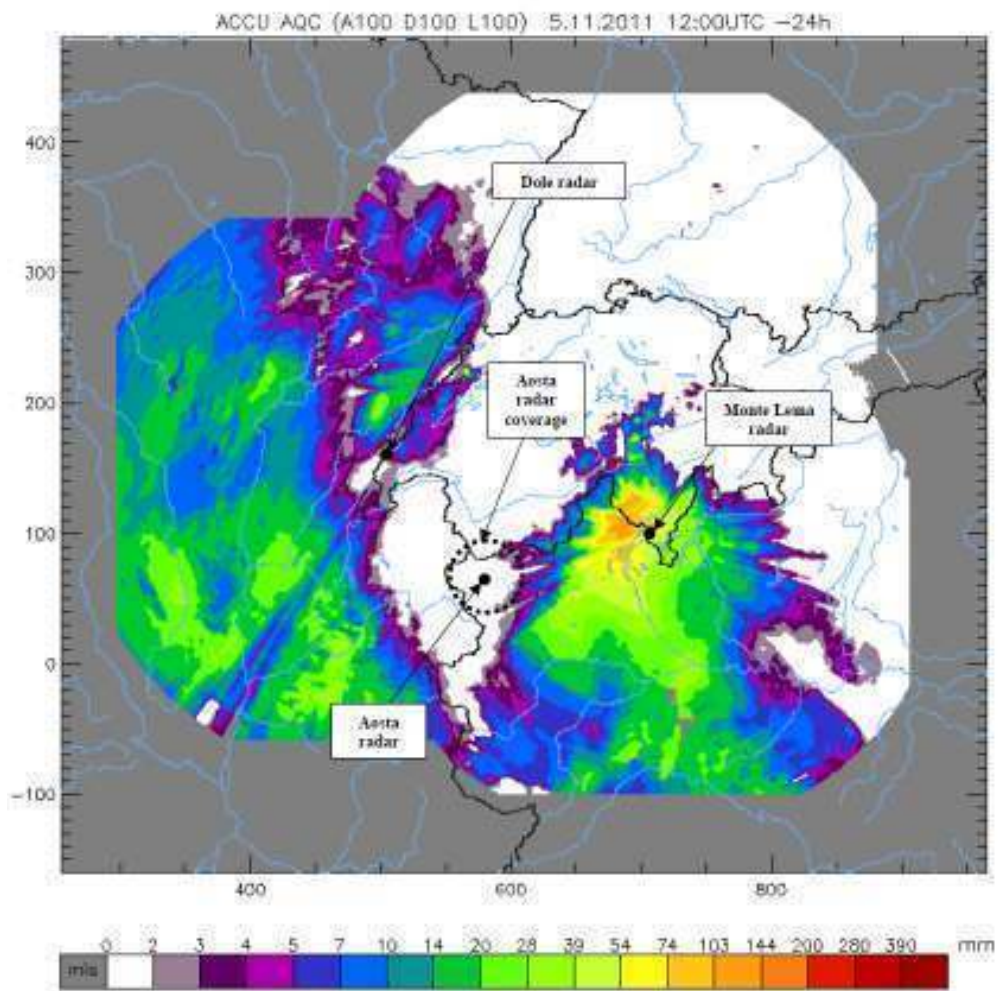


Figure 5.2. 24-hour cumulative rainfall amounts in the western Alps as seen by the Swiss weather radar network (from 12 UTC of November 4 to 12 UTC of November 5, 2011).

It is possible to supplement long-range weather radar information with precipitation fields derived at high spatio-temporal resolution by X-band radars of mini weather radar network. **Figure 5.3** shows what the low-cost X-band radar can detect, despite being deployed down deeply into the valley. As it can be seen, the 24-hour cumulative precipitation amounts surrounding Aosta town indicates values between 16 and 25 mm in 24 hours (yellow patch). According to rain gauges, such amount still represent about only 2 dB radar underestimation: from 12 UTC of November 4 to 12 UTC of November 5, in fact, the gauges “Aosta Piazza Plouves” (580 m MSL) and “Aosta St. Christophe” (550 m MSL) respectively measured 44.2 mm and 40.2 mm.

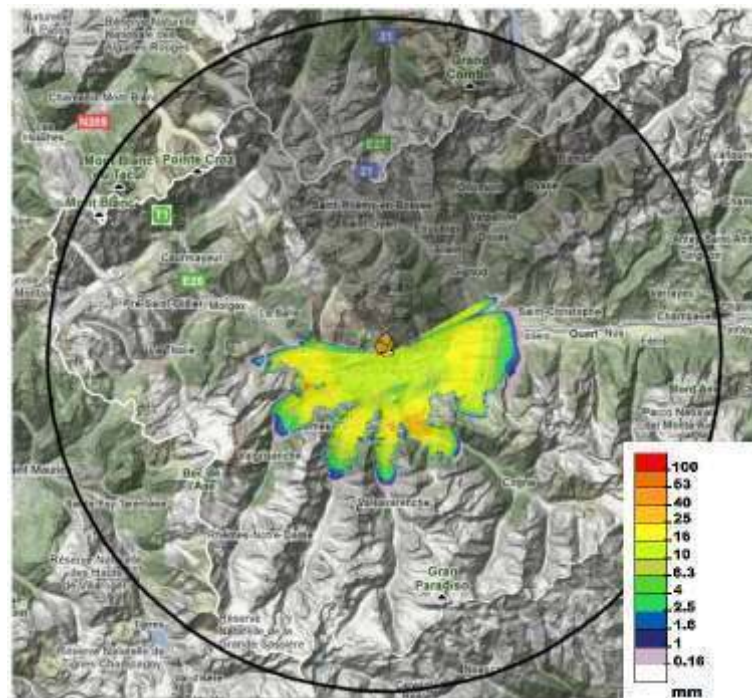


Figure 5.3. 24-hour cumulative rainfall amounts in the north-western part of Italy as seen by X-band mini weather radar located near the town of Aosta (from 12 UTC of November 4 to 12 UTC of November 5, 2011).

Finally, it is worth noting that the very complex orography causes severe beam shielding: the radar is practically blind at all ranges in the northern part of the circular surveillance area while in the southern half-circle weather echoes are only detected in approximately 10% of the 30 km range.

5.2 Detecting extreme rainfall events

The first example here presented shows a typical Mediterranean thunderstorm hitting the Palermo town in Sicily. The average hourly precipitation field on the evening of February 18th, 2011 in the northern part of a dry Mediterranean island (Sicily) is presented in the following **Figure 5.4**; it is worth noting the “wide precipitation band” shape and the high spatial variability of the field despite the averaging process used to derive hourly cumulated rainfall amounts. Each of the 6 consecutive pictures shows the average of 60 instantaneous maps of radar reflectivity (one per minute) transformed into equivalent rain rate using a fixed Z-R relationship. The first picture shows hourly accumulation rainfall amounts from 16 to 17 UTC; the last one from 21 to 22 UTC.

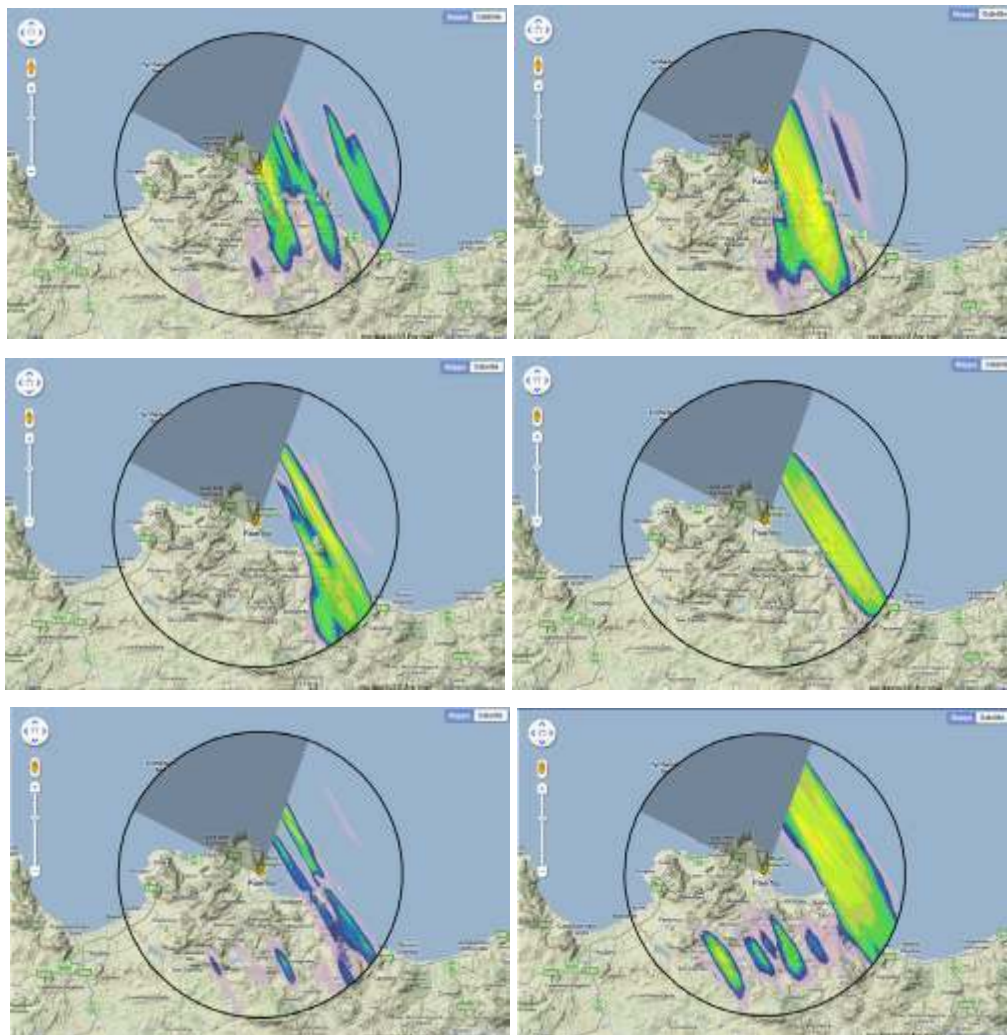
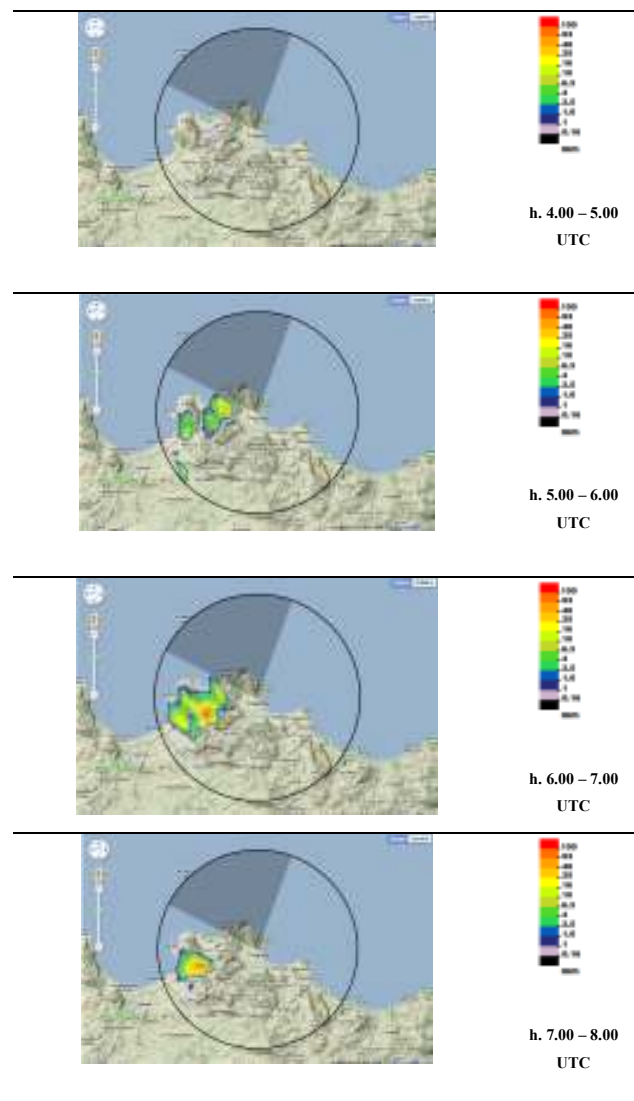


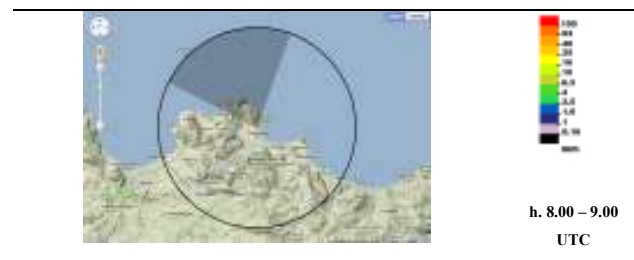
Figure 5.4. Hourly accumulated rain in Sicily, 11th February 2011.

The second example reported here is characterized by very intense rainfall, limited temporal duration and limited extension of the rain cell². Using the radar installed in Palermo it is possible to represent the hourly rainfall evolution, showing maps of accumulated rain, from 4:00 - 5:00 CET to 8:00 - 7:00 UTC of 18th February 2011 (**Table 5.1**).

Table 5.1. Hourly rain accumulation map between 4.00 CET to 9.00 UTC, 18th February 2011.



² The following examples are reported in: Allegretti M., S. Bertoldo, A. Prato, C. Lucianaz, O. Rorato, R. Notarpietro and M. Gabella, *X-Band Mini Radar for Observing and Monitoring Rainfall Events*, Atmospheric and Climat Sciences, Vol. 2, No. 3., pp. 290-297, 2012



The rainstorm had its maximum intensity between the 6.00 UTC and the 8.00 UTC where more than 60 mm of rain fell over an area less than 5 km² wide around Montelepre (PA), Italy. The rain events was extremely fixed and it did not move from its initial position until the end of the precipitation. This fact caused flooding and intense creep of water inside the town of Montelepre which is well documented by the following photo, reported in **Figure 5.5** taken, and kindly provided, by an operator of the Protezione Civile della Provincia Regionale di Palermo while he was moving to work.



Figure 5.5. Intense creep of water inside the town of Montelepre (PA).

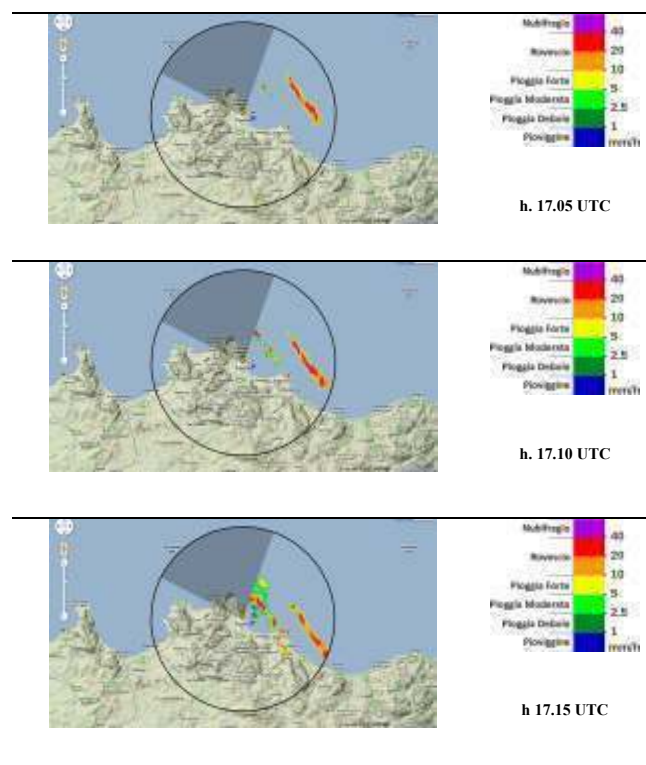
Considering a weather station installed in Carini (PA), Italy, at a distance of about 4.5 km from the center of Montelepre, a comparison between the rainfall amount measured by rain gauge and the one measured by radar was made in order show the spatial variability of rain fields. The rain gauge performs a measurement every 5 minutes and between 6.00 and 8.00 UTC of 18th February 2011 data have been provided with regularity. The comparison was performed comparing the gauge data with the

average rainfall measured by the radar on an area centered on the rain gauge with an extension of 1 km². It has been found that the rain gauge in Carini, between 6.00 UTC and 8.00 UTC, measured a maximum rainfall amount of only 6.5 mm, extremely low if compared with the one fallen over Montelepre measured by the radar which is more than 45 mm.

5.3 Detecting rain fields in rapid movement

Using the same X-band mini weather radar installed in Palermo an event with high temporal and spatial variability has been observed. The following **Table 5.2** reports the radar maps acquired by the radar during the late afternoon of 18th February 2011. In the North – East direction it is possible to identify a rain cell which is moving very quickly from North to South. It is to be noted that the radar acquires a map every minute while here a map every 5 minute is reported.

Table 5.2. Radar maps acquired by the radar in Palermo during the late afternoon of 18th February 2011.





In less than 15 minutes the intense rainfall events (a rate of more than 20 mm/h has been measured with the radar) moved at a very high velocity. X-band mini radars are able to detect such rain fields thanks to their high temporal resolution. This useful behavior can be applied both in observing precipitation when a particular event is already on (potentially even to control emergency procedure) and in post processing analysis to study the movement of the rain cells and to give statistical information. Of course rain fields movement can be observed with other instruments such as satellites, but the X-band radar are easy to install and provide for good quality maps and ease of use without requiring any particular skills.

PART 2

Other wireless sensor networks

6.

DGPS Wireless Sensor Network for landslide monitoring

6.1 Introduction

Wireless Sensor Networks (WSNs) are largely used for environmental monitoring purposes.

A first monitoring system based on a network of single frequency GNSS (Global Navigation Satellite System) receivers was installed on Grandes Jorasses serac in 2009 to trace its displacements¹. It was made by 3 sensor boards installed over the glacier to acquire GNSS data and 1 collector node to receive and process data installed in a more accessible place.

Due to the inaccessibility of the site and the severe environmental operative conditions, the developed sensors were able to transmit data through a wireless channel from the serac to the collector node, ensuring 24 hours a day and all weather conditions monitoring. High measurements accuracy is gained by exploiting the DGPS (Differential Global Positioning System) technique using local permanent GNSS stations.

¹C. Lucianaz, O. Rorato, M. Allegretti, M. Mamino, M. Roggero, F. Diotri, *Low cost DGPS wireless network*, IEEE-APS Topical Conference on Antennas and Propagation in Wireless Communications (APWC), 12-16 Sept. 2011, pp. 792-795, 2011.

The drawback of the installation was that the boards were unable to perform multitasking operations: contemporary acquisition of GNSS data and their transmission to the base node was not possible.

To overcome this limitation the network boards have been redesigned starting from a previous developed prototypal multipurpose board² and considering a more powerful microcontroller unit, more memory storage capacity and, moreover, adopting an open-source real time operative system to perform multitasking operations. Furthermore a custom wireless protocol has been implemented in order to achieve a more robust communication, and a triaxial analog accelerometer has been installed on the sensor board in order to track fast displacement. A data fusion operation between data collected by GNSS and accelerometers improves the monitoring capabilities of the entire system.



Figure 6.1. WSN multipurpose board.

To make the system more robust, a tool for automatically restart the electronic board in case of “dead lock” of the microcontroller has been included: a watchdog chip which continuously monitors the onboard microcontroller status.

Different sensor boards have been integrated and programmed in order to build a more robust DGPS wireless sensor network capable to operate, with a good reliability, 24 hours a day and 7 days a week. The WSN should be able to monitor a landslide, a glacier or a serac.

² O. Rorato, C. Lucianaz, S. Bertoldo, M. Allegretti, G. Perona, *A multipurpose node for low cost wireless sensor network*, IEEE APWC 2012, Cape Town, South Africa, 2-7 September 2012, pp. 247-250, 2012

6.2 Landslides monitoring phases

Considering the monitoring phase of a common landslide, it is possible to identify 3 different periods of intervention:

- *Training of the system*: the critical mass to be monitored is characterized during a period of about 5-10 days in order to define the speed of the various measuring points. Such training must be performed under standard monitoring conditions, when the landslide or glacier have a constant speed.
- *Standard monitoring*: during this phase, constant speeds of the measuring points are observed and a kind of "stability" of the landslide is detected. In such conditions is admitted a total system failure for a period of maximum 72 hours.
- *Pre-alert phase*: the geologist monitoring office establish a speed threshold. Specific procedures for early warning, aimed at increasing attention, and civil protection procedures (e.g. preparation of evacuation plans, information delivered to citizens, identification and realization of well marked escape routes) are implemented. In such a scenario, the system can tolerate failures of individual nodes on the total measurement and malfunctions on the complete system for a maximum of 24 hours.
- *Alert phase*: a second critical threshold for the landslide speed is reached. In this case it is assumed that the landslide mass is quite unstable and could accelerate until a total collapse. In this condition the failure of a single WSN node is admitted, but the WSN operability should be kept alive, together with the control PC or web server to access to the data and the information acquired by the sensors.

Based on previous experiences in landslides monitoring, the following landslide speed thresholds have been identified. They allow us to establish some specifications of the WSN network for landslide monitoring (**Table 6.1**).

Table 6.1. Landslide monitoring phase, landslide threshold speeds and admitted failures of the WSN.

	Standard monitoring	Pre-alert phase	Alert phase
Landslide speed	$\leq 3\text{-}5$ cm/day	> 9 cm/day	> 15 cm/day
Admitted failures	Entire WSN for 72 hours	Entire WSN for 24 hours	Only some nodes but not the entire WSN

A landslide can accelerate at certain times and exceed the warning threshold. Then it can return in conditions of ordinary "stability". The reasons may be different, usually due to meteorological events: heavy rainfall, high amount of water in the soil, lots of snow and so on.

When the landslide instability situation continues for long time, the landslide itself can accelerate to finally arrive to the total collapse.

In order to establish the WSN required accuracy for landslide monitoring let us consider the following data and demonstrations:

- A standard landslide can reach a common speed of 4-5 cm/day.
- A common pre-alert threshold is set at 9 cm/day ($V_{\max} = 9$).
- An initial position is estimated as $d_0 \pm \varepsilon$ con ε position measurement error.
- A second position is estimated as $d_1 \pm \varepsilon$ with a landslide speed of 5 cm/day.
- The speed of the landslide should be $V < V_{\max}$.
- $V = (d_1 \pm \varepsilon) - (d_0 \pm \varepsilon) \rightarrow V = 5 + 2\varepsilon < 9$ cm.
- $\varepsilon < 2$ cm.

As demonstrated, in standard conditions the entire WSN should have a maximum error of 2 cm in the estimation of the position of the points where the sensor nodes are installed.

The target accuracy can be reached by using single frequency low cost GPS receivers on the nodes and then performing a post processing DGPS measurement on an

elaboration unit connected to the master node equipped with an ad-hoc realized software.

According to the introduction and the initial specifications the standard system is made up by three main section:

- *The measurement network (WSN)*: it is made up by a set of the PCB boards made equipped with a set of sensors and a RF link. They perform the measurements and send the data to the master node of the network which is connected to a control PC.
- *Data acquisition and transmission center*: a computer placed near the monitoring network nodes, in a "safe" place, receives data from the WSN, records them, formats them properly and retransmits them to a local server.
- *Server for data acquisition and processing*: the server store the data and allow to apply to the measurement the DGPS technique. It also store the data and finally provides some graphics of the measurement results and allow authorized users to visualize the data on a common web page.

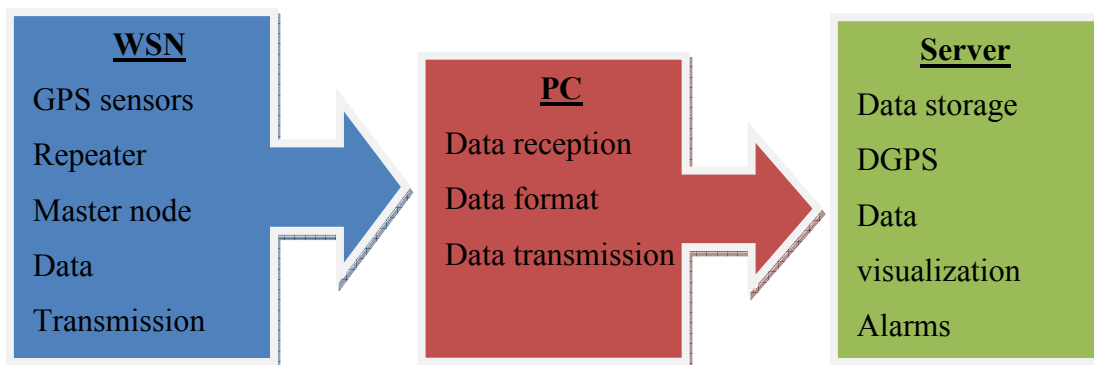


Figure 6.2. Different elements of the system to monitor the landslides, which include also the WSN.

6.3 WSN description

6.3.1 General description

The WSN for landslide monitoring has a star topology as shown in **Figure 6.3**.

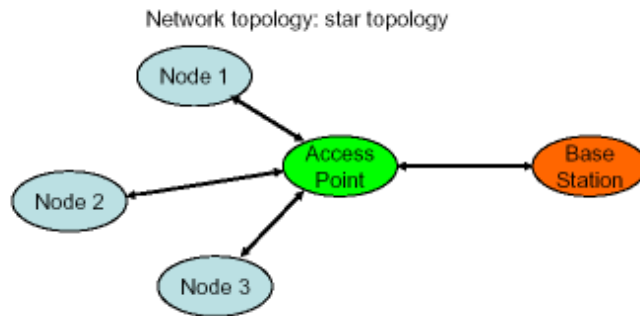


Figure 6.3. Star topology of the WSN for landslide monitoring.

Both “sensor nodes”, “access point” and “base station” node are equipped with the same hardware and the different behavior of the electronic boards is obtained by only varying the firmware, in order to reduce the costs as much as possible.

In particular, the functions of each network element are the following:

- *Sensor board* or *sensor node*: properly interfaced with a set of sensors, it is able to acquire environmental data and manage the data transmission to the access point;
- *Access Point board* (AP): it is an intermediate wireless network card that interrogates the sensor board and manages the data received through an ad hoc developed communication protocol;
- *Base Station board* is received from the radio data collection and transfers them via a serial connection to a computer.

The requirements for the installations of the WSN in star topology are the following:

- Conditions of visibility between nodes: LOS (line of sight).
- Radio links : point-to-point communication up to 300 meters.
- Bit rate: greater than 10 Kbit/s (proportional to the number of nodes).

6.3.2 Electronic board hardware description³

The system consists of four separate sections:

- Analog/digital sensors;
- Radiofrequency section;
- Microcontroller Unit and memory;
- Power supply stages.

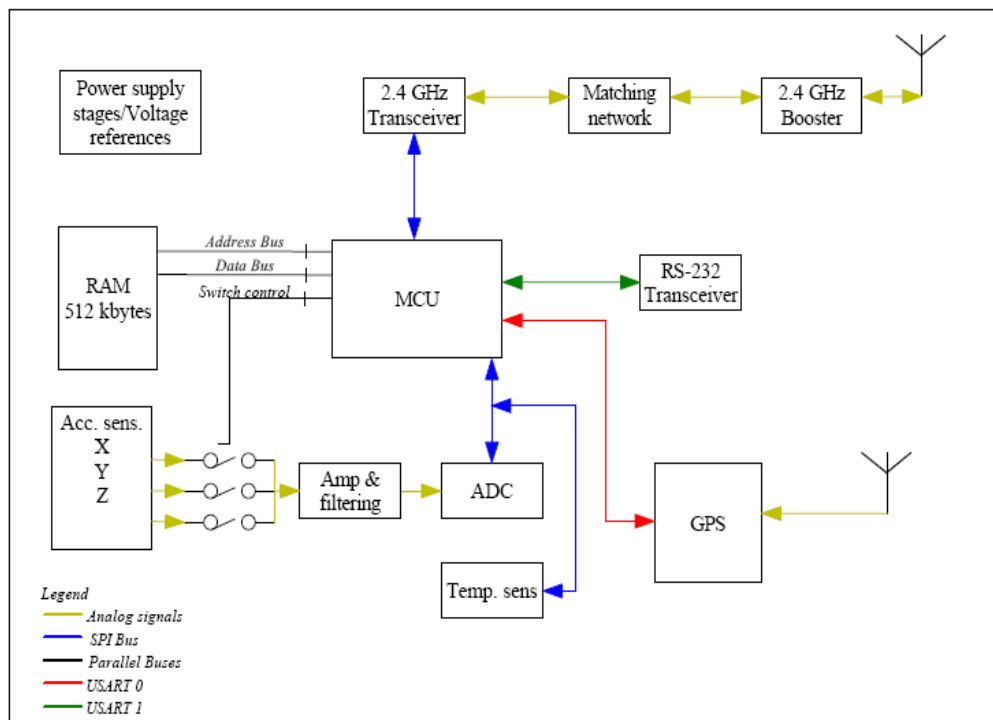


Figure 6.4. Block diagram of the WSN board.

Figure 6.4 shows the complete block diagram of the electronic board. Its stack-up is a four layers in FR4 substrate. During the layout design phase, particular attention was dedicated to the design of proper RF section (controlled impedance routes, via holes modeling) and to the routing of analog/digital mixed signal section (proper analog/digital grounding techniques, power supply plane).

³ The following description of the WSN electronic board has been published in: Rorato O., Lucianaz C., Vittaz E., Bertoldo S., Allegretti M., Notarpietro R., *A Wireless Sensor Network Board for Environmental Monitoring Using GNSS and Analog Triaxial Accelerometer*, International Journal of Embedded Systems and Applications, Vol. 2, N. 4, pp. 35-43, 2012.

6.3.2.1. Analog/digital sensors section

Since its prototypal multipurpose version, the WSN board has been designed to be provided with different types of sensors (e.g. accelerometers, temperature sensors, GNSS, photodiodes). The configuration for the presented WSN board is composed by a GNSS module, a triaxial analog accelerometer and a temperature sensor. Sensors communications are performed via USART or SPI bus.

The used *accelerometer* is a 16 pin LFCSP package, an analog sensor built with MEMS technology; it has three voltage outputs, one for each coordinate axis and each output has been connected to a conditioning circuit in order to match the input voltage range of the ADC converter. Conditioned outputs are then sent to a 3-ways multiplexer which allow proper selection of each channels during sensor readout.

The *GNSS module* is a U-Blox LEA-6T. It is configured directly by the WSN board at the start up, acquires satellite data and sends raw data every time a query is performed by the embedded control unit. Data are sampled every 15 seconds (~5 MB/day) but the sampling period can be changed in real time remotely sending the appropriate command to the board.

The *temperature sensor* is fully digital and is used to monitor board's temperature to prevent dangerous overheating.

In order to design the electronic circuits, their interfaces and connections, and to chose the best chip, some simulations have been performed using the software P-Spice®.

The accelerometer has been modeled according to the factory specifications reported on the datasheet (**Figure 6.5**) of the component because the model is unavailable on Analog Devices web site.

A set of simulations (DC sweep, AC, noise, Monte Carlo, worst case, advanced P-Spice sensitivity) have been performed to design the conditioning circuit: a non-inverting op-amp based amplifier that ensures very high input impedance that avoid sensor loading. The operational amplifier has been chosen taking into account the noise contributions, and its rail-to-rail output capability. OPA211 has been chose and to reach its best performance it has been powered with dual supply (+/- 12V).

Since the accelerometer presents three output analog signals coming from each axis, a switch is needed in order to collect data separately from each output. The choice of the TS3A4751 switch is based on the lowest leakage currents criterion.

Parameter	Conditions	Min	Typ	Max	Unit
SENSOR INPUT					
Measurement Range	Each axis	±2	±2.5		g
Nonlinearity	Percent of full scale		±0.2		%
Package Alignment Error			±1		Degrees
Interaxis Alignment Error			±0.1		Degrees
Cross Axis Sensitivity ¹				±1	
SENSITIVITY (RATIOMETRIC)²					
Sensitivity at X_{out} , Y_{out} , Z_{out}	Each axis $V_S = 3\text{ V}$	378	420	462	mV/g
Sensitivity Change Due to Temperature ³	$V_S = 3\text{ V}$		±0.01		%/°C
ZERO g BIAS LEVEL (RATIOMETRIC)					
0 g Voltage at X_{out} , Y_{out}	$V_S = 3\text{ V}$	1.3	1.5	1.7	V
0 g Voltage at Z_{out}	$V_S = 3\text{ V}$	1.2	1.5	1.8	V
0 g Offset vs. Temperature			±1		mg/°C
NOISE PERFORMANCE					
Noise Density X_{out} , Y_{out} , Z_{out}			250		µg/√Hz rms
FREQUENCY RESPONSE⁴					
Bandwidth X_{out} , Y_{out} ⁵	No external filter		1600		Hz
Bandwidth Z_{out} ⁵	No external filter		550		Hz
R_{int} Tolerance			32 ± 15%		kΩ
Sensor Resonant Frequency			5.5		kHz

Figure 6.5. Accelerometer specifications (extract from datasheet)

The signals acquired by ADC converter presents a very low frequency (some tens of hertz). To chose the best converter the most important parameters are the static specification like INL, DNL and offset error: the ADS7279 has been chosen.

To maximize ADC performance, the R-C filter in front of its analog input has been redesigned. In fact the performances of the ADC relate to its internal capacitor that presents a non-linear behavior related to voltage and sampling frequency: to compensate these unwanted behavior we designed an external RC filter [5].

The ADS7279 needs an external voltage reference: REF5050 has been chosen for its high temperature stability and for its very low noise characteristics.

6.3.2.2. Radiofrequency Section

Each WSN board is equipped with the CC2500 wireless transceiver. It is a low-cost 2.4 GHz transceiver designed for very low power wireless applications. The main operating

parameters and the 64-byte transmit/receive FIFOs of CC2500 are controlled via the SPI interface as already mentioned for the analog and digital sensors.

The other component of the RF section is the CC2591, used both as a low noise amplifier and a power amplifier. The matching between CC2500 and CC2591 has been done according to the following steps:

- using Agilent-ADS® software, the match between CC2500 differential output and the 50 Ohm line has been established;
- the “balun” used in the Texas Instruments CC2591 reference design guide has been used to match the 50 Ohm line to the CC2591 input impedance;
- the same matching design showed in the Texas Instruments CC2591 reference design guide has been used to match the CC2591 output impedance to the 50 Ohm Antenna.

6.3.2.3. Microcontroller Unit - Memory

This section of the board presents the core of the system: the microcontroller MSP430F2619. It manages the following components: analog to digital converter, switches, temperature sensor, RF transceivers, memory, GNSS and accelerometer. The MCU also allow the wireless network protocol to run properly.

This type of microcontroller has been chosen due to its low power consumption: when it is used in active mode its current consumption is equal to approximately 8 mA.

The board is equipped with a 512 kB SRAM for data storage and buffering. It is managed as a circular buffer to support multitasking operations. In fact, especially when a radio communication is performed, it is important to continue sensors acquisition in order to avoid data losses.

6.3.2.4. Power supply stages

The board is powered by a buck switching power supply (TPS54357), which is able to convert the 12V positive supply in an output voltage of 5V. This component has been chosen because it does not require additional external switches and guarantees very low

ripple noise, if properly designed. The software SwitcherPRO® is used as an aid to dimension the few external components needed.

The 5 Volt supply is used to feed two LDO (Low Drop Out) regulators, providing 3V (TPS73730) and 3.3V supplies (TPS73733), needed by different components placed on the board. This components have been chosen for their very low quiescent current and very low noise performance.

6.3.2.5. Serial Transceiver

The master node is connected to a control PC. The communication between the master node and the embedded PC is managed exploiting the RS-232 protocol. This protocol is robust and simply and is one of the industrial standard. Since the voltage levels of the RS-232 protocol are not compatible with the voltage levels of the microcontroller, a levels shifter is used.

To increase the robustness of the communication was chosen cable UTP category-6 double-shielded and therefore more immune to external disturbances, according to the specifications in **Table 6.2**.

Table 6.2

RS232 cable length according to Texas Instruments

Baud rate	Maximum cable length (ft)
19200	50
9600	500
4800	1000
2400	3000
1200	6000

6.3.3 PC to control the network and process data

The control PC must is responsible of the management of the local network (between the access point and the base station). The PC has been chosen paying particular attention to robustness and low power consumption. The tasks that the PC performs are:

- To receive of serial strings from the master node;
- To learn the initial composition of the network (number of nodes and initial measurements);

- To send SMS when a possible alarm situation is detected;
- To periodically send a log file to the remote server in order to know the network status;
- To periodically send a positions measurement files to the remote server already converted to the GPS exchange format RINEX and ready to be processed with DGPS techniques
- To periodically send a log files of the measurements made through the accelerometer.

In order to perform the described operations, the PC is equipped with Linux as operating system (Ubuntu distribution), and open source software.

In the standard configuration, the communication between the PC and the remote server is based on GPRS, because even if GPRS has a lower bit rate with respect to UMTS, it is more widespread in the area and has superior stability characteristics. Especially in remote installations the probability to have a GPRS coverage is higher since it can be guaranteed by a transmitter higher in range but which requires lower power, if compared to UMTS.

In order to exploit the GPRS connectivity, a GPRS commercial router is connected to the control PC.

6.3.4 Remote server

The remote server is capable to receive data from the monitoring site, to perform the necessary processing operation and presenting the results to the authorized users. The server is reachable in internet with a static IP addressing.

The server must host the following services:

- *SSH server*: to allow authorized users to access all the features of the server remotely, in particular for inspection and maintenance purposes;
- *FTP server*: to receive data from remote installations and allow authorized users to download them, if needed;
- *WEB server*: to show the measurements and the processing results on the web interface;

- *PHP service*: to implement web services using the scripting language PHS that allows you to create dynamic pages;
- *CRONTAB*: a specific service to run scripts at specific time and intervals.

The server is also equipped with specific libraries to implement the DGPS techniques using data acquired also from the permanent stations.

6.4 Firmware and software implementation

6.4.1 General WSN firmware description

The WSN is managed by an ad-hoc realized hand shake protocol.

As soon as the network is turn on for the first time the standard initialization routine is performed: the AP will query the network to detect the presence of nodes. The same operation is then repeated frequently, a specific interval of time, to keep trace WSN situation and composition. To do this, the AP then sends a packet with broadcast address with a request of *INQUIRING*. Each slave node sends back to the AP a packet containing information about its status. In order to avoid collisions, before the transmission, checks if the communication channel is free and sends its packet only if no other nodes are already transmitting. Otherwise the node waits for a random interval to perform a new check if the channel is free and to perform a transmission. The AP waits for a specified period of time within which all nodes must respond. After the specific time interval the AP dynamically and locally saves the status information of the network in such a way that it is always possible to know which are the node connected to the network.

The AP will then request data coming from each sensor node by scanning them in an specific order and asking data packets from the various sensors. Each addressed node answers with the requested data.

The communication protocol have also a counter of the packet that allow to check if some of them are lost during the communication.

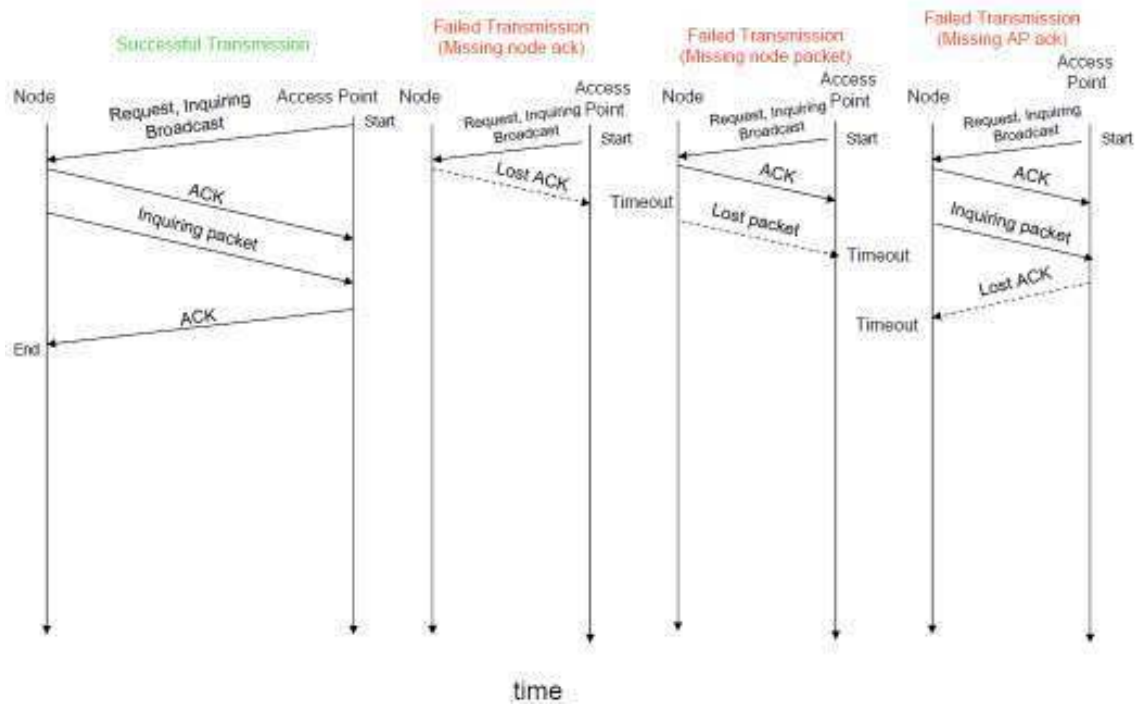


Figure 6.6. Network transaction. Broadcast Inquiring.

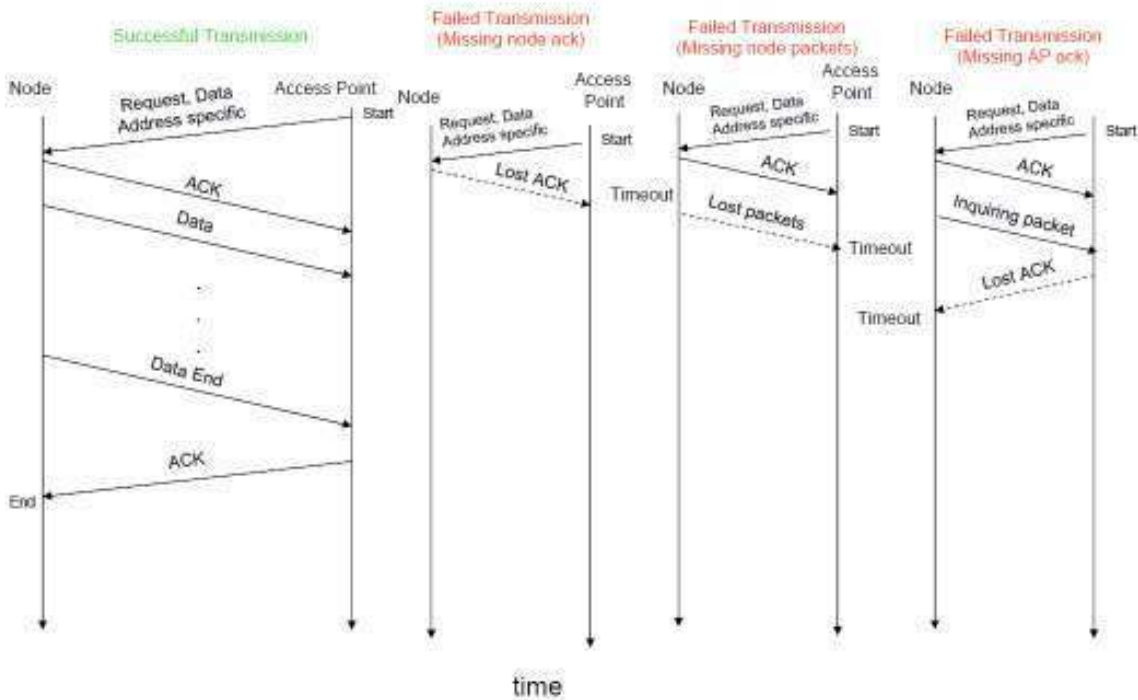


Figure 6.7. Network transaction. Data Request.

6.4.1.1 The real time operating system

The first version of the GNSS network realized in 2009 was not able to collect GNSS data and transmit them from the sensor to the collector node at the same time: the board did not perform multitasking operations.

In order to make the sensor nodes able to perform various operations at the same time without losing GNSS and accelerometer data, the boards needed to be equipped with a software or a firmware able to operate in a multitasking context.

In particular, the sensor board must perform the following operations:

- Acquire GNSS data;
- Acquire accelerometer data;
- Store GNSS data in RAM;
- Store accelerometer data in RAM;
- Acquire data from temperature sensor for board status monitoring;
- Radio data transmission;
- Wireless network management.

As the MCU has a single core architecture it is not possible to perform a hardware multitasking.

A Real Time Operative System is one of the best way to perform all the tasks in quasi-real time. The open source FreeRTOS® was chosen due to its good performance and due to its open source philosophy and it has been appropriately modified to operate on the board with a proper “porting” operations.

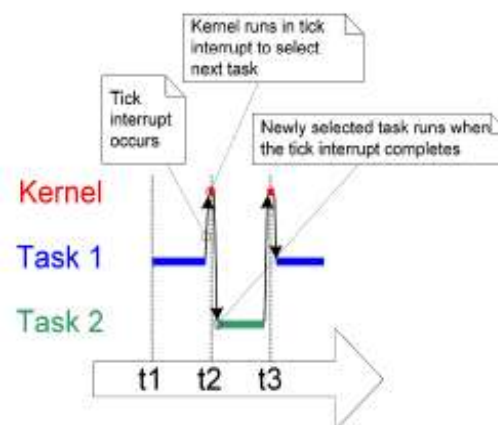


Figure 6.8. Principle of real time operating system.

The firmware has been properly realized according to the specifications of the real time operative system and implementing a specific state machine.

6.4.1.2 A custom boot loader realization

The *bootloader* is a program on the flash memory of the MCU. It has been designed to communicate through the WSN communication protocol in order to update the firmware on the sensor node.

In fact, when the boards are in the field, severe environmental conditions and their position difficult to reach do not allow to perform ordinary maintenance operations. For instance a firmware update usually performed with the RS232 interface (the common bootloader installed on the MSP430F2619 microcontroller) cannot be done if the boards are installed at more than 4000 m on a serac to monitor its displacement or on a dangerous landslide.

Therefore a new type of wireless bootloader has been realized and has been installed on each sensor board.

In order to update the firmware on the WSN boards the following steps are necessary:

1. Compiling the new firmware in order to obtain an image file in the Texas Instrument proprietary format called “ti-txt”;
2. Connect a pc to the access point (which is installed in an accessible place) and send its a command to enable the reception of the new firmware from the pc;
3. The access point sends a request to each sensor nodes in order to put them in “bootloader” mode waiting for its acknowledgement response;
4. The access point sends the “ti-txt” file to the sensor nodes;
5. After the complete reception of the new firmware version the sensor nodes reboot themselves in order to run the new firmware.

6.4.2 Control PC: software to control the WSN, receive and store data

In order to be processed, the GPS data acquired by the network nodes must be converted from the original proprietary format UBX-RXM-RAW to the standard format RINEX (Receiver Independent Exchange Format). To perform the conversion, at first it

is necessary to create an intermediate RAW binary files containing the strings sent by the GPS sensor nodes to the AP.

The software realized for the control PC creates the specified binary files that will be processed by other module and five other log files necessary to monitor the network status. All the files are written with a proper function within the main processing cycle which is made by two steps:

- *Packet acquisition* on the serial port which link the AP to the control PC;
- *Packet processing*.

6.4.2.1 Packet acquisition

The function devoted to acquire the packet incoming on the serial port fills a vector of characters with a packet (GPS, temperature or inquiring) sent from a specific sensor board to the AP. The structure of this function is based on a loop acquisition that lasts until the entire packet has been received.

6.4.2.2 Packet processing

The function devoted to process the packets parses the packets incoming on the serial port, update the log files (RAW binary files included), and maintains the list of active network nodes. The sequence of operations the following:

- Initialization of the list of nodes if the network has been turned on for the first time;
- To manage the packets received from the different network nodes;
- To add a new sensor node if it is added to an already operative WSN;
- To set the proper flag when a specific network node transmits for the first time a GPS packet;
- To write the entire GPS packet in the file *packetsfile.log*;
- To update the file *statistics.log* (related to WSN statistics) if GPS data or temperature packets are received;
- To update the file *temperature.log* when a temperature packet is received;

- To update the file *networkstatus.log* and the file *logger.log* when it is received a packet confirming that a specific node is still connected to the WSN;
- To switch of *packetsfile.log* files and RAW files every hour. There are two packet files and two RAW files (*packetsfileA.log* e *packetsfileB.log*) that are exchanged every hour. This solution is necessary to allow other software to work on older files while new GPS are still coming to the AP from the sensor nodes of the WSN.

In all the log files mentioned above, except than *packetsfile.log*, date and time of the acquisition of a specific information is reported at the beginning of each line. All the created files are stored in well defined file system archive, in order to keep all the data for backup reasons.

The final obtained files in UBX-RXM-RAW format are than ready to be converted to RINEX file. The remote server acquires such files at specific interval with an ad-hoc script using an FTP connection.

6.5 Implemented services and to the data on the remote server

On the remote server, each file containing GPS data is converted into the universal interchange format RINEX (Receiver Independent Exchange Format). They are used together with the data acquired from permanent stations located in the area, to assess the position exploiting the DGPS techniques.

To perform such operations, the remote server has been equipped with set of bash scripts that are executed automatically on the Linux server, according to a well defined timing diagram. The post-processing system then takes care of the following operations:

- To download of the RINEX files from the permanent stations through an FTP;
- To download data from the Control PC of the WSN;
- To compute the *baseline* (i.e. the distance between each nodes of the WSN and the permanent station) through a differential calculus of coordinates;

- To create a report file;
- To create a chart of the baselines as a function of time slots at which they are computed;

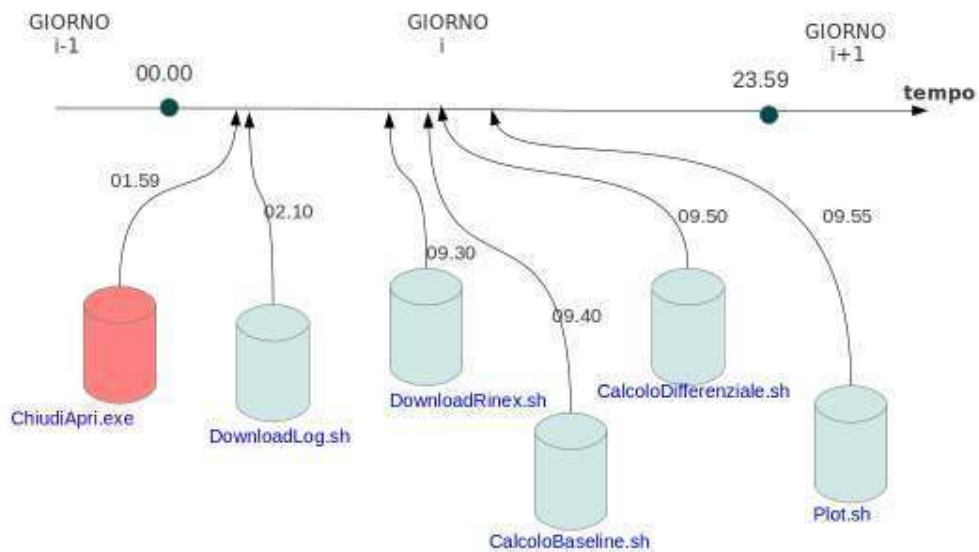


Figure 6.9. Time diagram of the activities of the remote server.

As stated before, the output of the WSN control PC is a file format UBX-RXM-RAW which contain the GPS data acquired by each sensor node. In order to process these data it is necessary to convert them to the format standard RINEX (Receiver Independent Exchange Format). The standard RINEX fact allows the storage and exchange of data regardless the used receiver used to perform the measurement. In this way it is possible to process data using third-party software that does not require compliance with standard specifications owners, often closed. The conversion of the file to UBX-RXM-RAW and RINEX data processing is performed using the open source library *Rtklib v.2.4.1*.

The DGPS computation service allow authorized to access the data on a web site where all the data can be browsed and downloaded. Moreover, data related to a specific

landslide are reported on a common cartographic system together with some graphs and reports showing the measurements in function of the time.



Figure 6.10. Example of a landslide represented over a common cartographic system.

The page containing the graphs of a specific DGPS WSN allow user to know also the status of the network and if some of the nodes are suffering from some failure.



Figure 6.11. Graphs web page during the test phase.

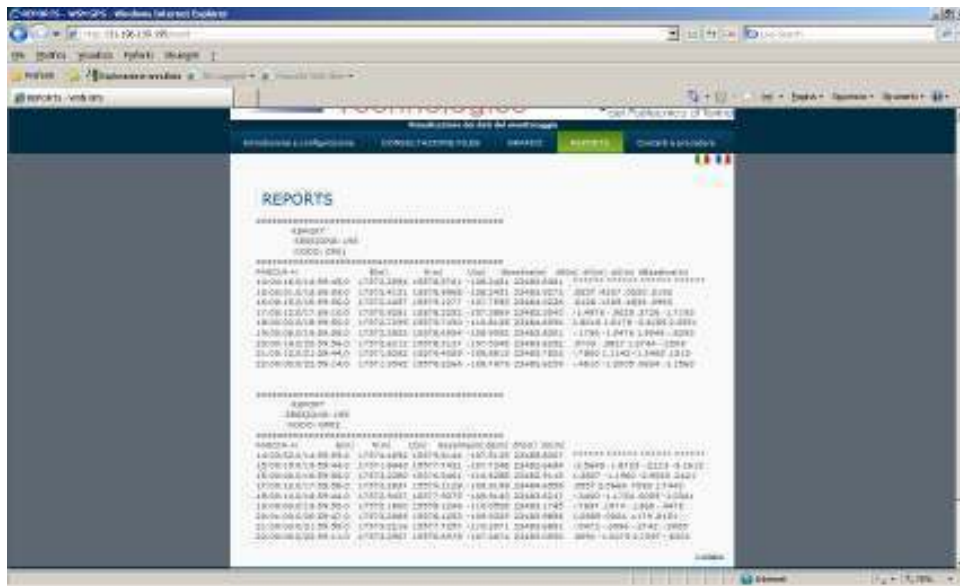


Figure 6.12. Report page of the web site during the test phase.

Other services that will be realized in the future are:

- Implementation of a specific SMS alert to a list of specific phone numbers;
- Implementation of a tool to communicate by e-mail a possible alarm related to a landslide.

6.6 Test results

A first prototype of the network have been realized and some test have been performed in order to check the proper function of each boards and of the entire WSN. Preliminary tests in laboratory show that all the sensors (temperature, accelerometer, GPS) worked good and it was possible to test the entire network after the set up of an experimental installation.

6.6.1 Experimental installations

The first experimental WSN was made by two sensor nodes in the Aosta Valley in order to use the permanent station identified by the name FOND and located in Courmayeur (AO).

The tests took place during different sessions. Among them the most significant has duration of 9 days, which is a good time interval to simulate the behavior of the WSN.

6.6.1.1 Permanent Station (FOND)

A permanent station is a fixed GPS installation built with a geodesic receiver and geodesic antenna. It continuously acquires the GPS signals emitted by the visible satellites. These signals are available in the standard RINEX for post processing DGPS measurements.

The RINEX data used for the experimental tests of the WSN are provided by the GNSS permanent station located at “Fondazione Montagna Sicura” (FOND) in Courmayeur (AO), Italy.

According to the official station monograph, the coordinates of FOND are:

- Latitude: 45°49'12.35107” N
- Longitude: 6°57'49.34960” E
- Altitude: 1505.3202 m.



**Figure 6.13. Antenna of the permanent station FOND
(the receiver is inside the building of Fondazione Montagna Sicura).**

The station data are available through an FTP server. The RINEX files are closed every day at 24:00 GMT and forwarded to the ftp server. The RINEX files of the station FOND are sampled at 1 Hz so they can reach the size of 30 MB. Given the size of the file, and the consequent latency time to transfer them to the WSN remote server, the differential calculations are performed at the completion of the reception of the daily RINEX file.

6.6.1.2 GPS sensor nodes (GP01 and GP02)

Two GPS sensor nodes have been installed not so distant from each other: the distance between them is only 15 m. In particular the GP02 was installed in a place with visibility of less than 180° above the horizon and with an elevation greater than 15° . In this way it was possible to evaluate the multipath effect due to vertical wall near the installations (with error larger than 10 cm between two consecutive measurements). For this reasons, in the following only the results related to GP01 are considered.

In **Figure 6.14** and **Figure 6.15** it is possible to note that each network node, in an operative configuration, is not only made up by the electronic board. A battery, a charge regulator, and the electronic board are fixed inside a waterproof box outside which both GPS and RF antennas are mounted. The node is powered also by a solar panel in order to simulate a real installation of the WSN.



Figure 6.14. Experimental installation of the first GPS network node GP01.



Figure 6.15. Experimental installation of the first GPS network node GP02.

6.6.2 Coordinates systems

The results are available with two different coordinate systems:

- The first is a geocentric Cartesian coordinate system. The geocentric triad XYZ is fixed to the Earth, and follow it in its movement: the systems is called ECEF (Earth Centered Earth Fixed). ECEF coordinates are used in the GPS positioning system because they can represent both the state of the satellite and the state of the receiver.
- The second coordinate system is called ENU (East - North - Up) and it is a system of plane coordinates that allow to easier measure displacements and speeds. This coordinate system is suitable to describe the relative displacement between two GPS receivers in a Cartesian coordinate where the measurement unit is meters.

It is to remember that the goal of the WSN is the evaluation of the baseline. In the specific test, the baseline is evaluated between FOND (the permanent station), and GP01 and GP02 (the WSN GPS nodes). The baseline between FOND and GP01 and FOND and GP02 are long less than 50 m.

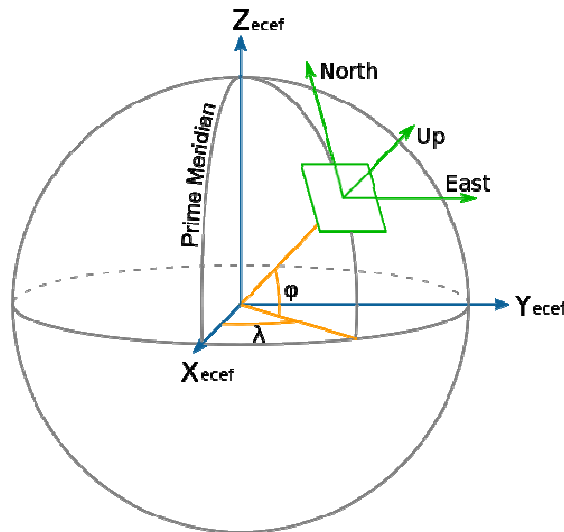


Figure 6.16. Relation between ECEF and ENU coordinates systems.

6.6.3 Results

The first results are related to the baseline (distance between GPS and permanent station). It is the same distance that is measured by a laser beam between the prism and landslides when a total station system is used.

During the 9 days of the test, the baseline was measured several times with a maximum difference between two values of 1.9 cm. It means that in case of a movement of a landslide body in the direction of a station or a hypothetical house, it would allow to obtain a good accuracy in the estimation of the speed of the landslide (according to what reported in the **paragraph 6.2**). **Table 6.3** reports the differences in the measurements of the baseline between two consecutive days (note that the day number is progressive since the beginning of the test).

Table 6.3. Differences in the measurements of the baseline between two consecutive days.

	Days 72 - 74	74 - 75	75 - 76	76 - 77	77 - 78	78 - 80	80 - 81
e	0.07 cm	0.08 cm	0.31 cm	0.31 cm	0.06 cm	0.06 cm	0.12 cm
n	0.14 cm	0.03 cm	0,19 cm	0.64 cm	0.62 cm	0.04 cm	0.08 cm
u	1.02 cm	0.48 cm	0.04 cm	0.78 cm	2.27 cm	1.41 cm	1.13 cm

Table 6.4 reports the daily mean measurement in ECEF coordinates and the same information are plotted in the 3D-plot in **Figure 6.17**.

Table 6.4. ECEF coordinates daily mean measurements.

	x (m)	y (m)	z (m)
72	4420869,92968333	539933,116683333	4552428,49325
74	4420869,93211818	539933,118163636	4552428,48835455
75	4420869,92418571	539933,115064286	4552428,48867143
76	4420869,92685556	539933,119744445	4552428,49008889
77	4420869,93604	539933,11675	4552428,48524
78	4420869,93026364	539933,116481818	4552428,48732727
80	4420869,93096	539933,11512	4552428,49303
81	4420869,92053333	539933,110483333	4552428,4889

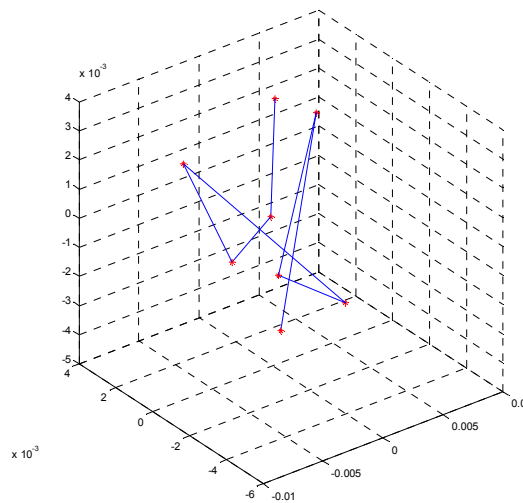


Figure 6.17. ECEF coordinates daily mean measurements: 3D-plot.

Considering the differences between the mean values of two consecutive days it is possible to note that they are lower than 1 cm (**Table 6.5**). It is a very good results and confirm that this WSN can be used to monitor landslide.

Table 6.5. Difference between the mean values of two consecutive days.

Day	Δx	Δy	Δz
74-72	0,0024	0,0014	-0,0048
75-74	-0,0079	-0,0030	0,0003
76-75	0,0026	0,0046	0,0014
77-76	0,0091	-0,0029	-0,0048
78-77	-0,0057	-0,0002	0,0020
80-78	0,0006	-0,0013	0,0057
81-80	-0,0104	-0,0046	-0,0041

6.6.4 Conclusions

The tests show that the low cost DGPS Wireless Sensor Network for landslide monitoring, entirely design for what concern both hardware, firmware and software has good performance and can be used in an operative situation. In particular it is possible to measure the speed of a landslide within the specification of a pre-alert phase using the ENU coordinates. It is also possible to monitor the state of a landslide in a situation of standard monitoring by simply measure the positions of the WSN nodes on a daily basis, using the DGPS technique and considering the measurement results within a ECEF coordinates system.

7.

Other application of Wireless Sensor Networks

7.1 WSN as anti theft alarm system for photovoltaic panels¹

The researches about alternative energy sources together with many government incentives have caused a substantial increase in the number of photovoltaic (PV) system installations. However stealing and damages to PV modules are increasing too.

For instance, in the solar power plant located in Serre Persano, in the province of Salerno, Italy, 7.000 of 60.000 installed panels have been stolen in less than one year²; an online newspaper reported that the theft of 140 panels during the New Year's Eve 2012 caused an economic damage of 150.000 €³.

A new low cost experimental and prototypal Wireless Sensor Network has been ad-hoc designed and tested to increase the PV protection implementing an ad-hoc communication protocol.

¹ The described work about the anti theft alarm system for PV panels, has been published as follow: Bertoldo S., Rorato O., Lucianaz C., Allegretti M. *A Wireless Sensor Network Ad-Hoc Designed as Anti-Theft Alarm System for Photovoltaic Panels*, Wireless Sensor Network, vol. 4 n. 4, pp. 107-112, 2012

² V. Gualerzi, "Ora il solare fa gola anche ai ladri, rubati all'ENEL migliaia di pannelli", <http://www.repubblica.it/2006/11/sezioni/ambiente/solare/furti-pannelli/furti-pannelli.html>, 2007.

³ "Maxi furto di pannelli fotovoltaici. Bottino da 150 mila euro", <http://www.arezzoweb.it/notizie/speciale.asp?idnotizia=72527>, 2012.

No already existent communication protocol has been used but a new one has been studied and implemented in order to completely design all the aspects of the system.

7.1.1 WSN general description

Accelerometers have been used in order to detect an alarm when a PV panel is removed from his installation point.

An electronic board equipped with such an accelerometer sensor has been designed to be installed below each PV string to detect movements and transmit to a central node the consequent alarm signal.

The entire WSN has been designed with a master-slave architecture and star topology. A central node, called master node or Access Point (AP), performs periodic monitoring and scanning operations of all the sensors and dialogues with an embedded control PC. It has to be noted that each slave nodes communicates only with the master node and not between each other. The control PC is a common commercial embedded PC connected to internet using a GPRS router, thus allowing the communication with a remote server and remote management operations.

Each slave node has an almost irrelevant current consumption and is fed up by an appropriate power network. This one, together with RS-232 serial cable that connects the master node with the embedded control PC are the only two wiring rows required by the WSN.

Each board comprises a solid state triaxial accelerometer connected to a microcontroller which can process data and potentially detect the alarms. The microcontroller generates messages and transmits through RF link to the master node using a proprietary protocol. The same AP communicates with the embedded PC control via RS-232 serial interface.

The AP performs a cyclical interrogation to each slave node of the WSN in order to monitor the network status. Such information are processed by the control PC and then sent to a remote server to be stored. When a sensor detects an alarm, a continuous signal is sent to the AP and, consequently, to the control PC which turn on all the alarm

signaling systems: SMS and/or e-mails are sent to a list of previously configured users, and a sound-light signaling system is activated.

The management of alarms generated by a sudden movement is made directly by the microcontroller. The acceleration values measured by each sensor on the three axis in terms of voltages, are sampled and converted to acceleration (in terms of g value). The algorithm operates directly on these acceleration values and triggers an alarm when a 5 degrees tilt variation is detected in at least one of the three directions.

To make the system more robust a tool of automatic restart for the electronic board in case of "lock" of the microcontroller has been included in the board firmware.

7.1.2 WSN designed hardware

The WSN is made up by several slave nodes and a single master node. All the electronics boards are entirely designed specifically for this application (**Figure 7.1**).

The electronic boards have been designed to perform both the sensor node functions and the access point functions by varying only the firmware. This choice greatly shortens development time and maintenance costs: a possible component fault could be the same for each node of the WSN.

All the boards power supply is equal to ± 12 V provided by a specific power network. On the +12V line the current consumption is approximately 50 mA in normal operative conditions and about 200 mA when the RF transmission is on. On the -12V line the current consumption is negligible. As each sensor board perform the RF transmission individually (thanks to the developed communication protocol between AP and slave nodes, see details in paragraph 4) and lasts a very short time interval, it can be said that the average current consumption of each board is slightly greater than 50 mA.

A single board is made up by several subsystems such as:

- Power supply stages;
- RAM memory;
- Sensors (with accelerometers) / Filters and Analog to Digital conversion chain;
- Microcontroller;
- RF radio circuits;

- RS-232 transceiver.



Figure 7.1. Sensor board used in the WSN designed as anti-theft alarm system for PV Panel.

7.1.2.1 Power voltage stage

Power voltage stage provides for different power values needed by the electronic components. In particular using an integrate switching controller (Texas Instrument TPS54357) a +5 V d.c. power supply is derived as needed by the ADC, while using two linear power regulators (Texas Instrument TPS73733 and Texas Instrument TPS73730) +3 V d.c. and +3.3 V d.c. values are derived as needed by microcontroller, other integrated components and accelerometers sensors.

7.1.2.2 SRAM memory

Each board is equipped with a SRAM memory of 512 kb. Its purpose should be to store the data acquired by the accelerometer in order to have at our disposal a sufficient time window for data processing. Memory access is performed with a 8-bit parallel data bus and a 19-bit parallel address bus both driven by the microcontroller. At the moment the SRAM memory is not used and it has been included on board to be used in the next firmware and WSN versions.

7.1.2.3 Sensors

The card is provided with two types of sensors: a solid state analog accelerometer (Analog Devices ADXL327) and a digital temperature sensor (Texas Instruments TMP121).

The temperature sensor is needed to compensate for the drift of the accelerometer due to the external temperature variations. The chosen sensor is fully digital and information on temperature are obtained by periodic queries performed by the microcontroller through the SPI bus.

The accelerometer sensor is an analog sensor built with MEMS technology; it has three voltage outputs, one for each axis, corresponding to values between -2g and +2g. Each output has to be connected to a specific circuit to force the usable bandwidth of the accelerometer⁴: for this application a 220 nF capacitor has been used in order to operate with a bandwidth of approximately 22.6 Hz, sufficient for detecting movements of human origin.

Accelerometer outputs are sent to a 3-ways multiplexer which allow to convert digital values with an ADC. Analog to digital conversion is driven by the microcontroller via SPI bus at regular intervals. The system performance allow to estimate the acceleration of each axis with a resolution of 3 mg, almost equal to the one measured with a seismograph.

7.1.2.4 Microcontroller

The microcontroller (Texas Instruments MSP430F2619) manage all the other chips installed on the board. It also process the data collected by the sensors in real time in order to send a potential alarm communication. The choice of this type of microcontroller was driven by its low power consumption: when it is used in active mode its current consumption is equal to approximately 8 mA.

The firmware is downloaded to the microcontroller through the TI programmer using the JTAG protocol.

7.1.2.5 RF circuits

The RF circuits are the part of the board which allows the sensors to communicate with the access point in a bidirectional way.

⁴ O. Rorato, *Studio e progettazione di sistemi elettronici per monitoraggio ambientale*, Politecnico di Torino, Torino, 2012.

The RF circuits are made up by a transceiver (Texas Instruments CC2500) and an amplifier (Texas Instruments CC2591) used in a dual manner: power amplifier in transmission and low noise amplifier in reception. A matching network has been designed between the transceiver and the amplifier in order to allow the maximum power transfer between the modules and to avoid the transmission of spurious frequency components. As the other components, the transceivers is also driven by the microcontroller though the SPI bus.

The chosen operating frequency for the WSN is 2.4 GHz in order to deal with small antennas. Data packets are transmitted with a FSK modulation and a baud-rate equal to 9600 bps.

7.1.2.6 RS-232 transceiver

The communication between the master node and the embedded PC is performed through the RS-232 standard. Since the voltage levels of the RS-232 protocol are not compatible with the voltage levels of the microcontroller a level shifter is used, in order to enable the dialogue between the microcontroller of the master node and the embedded PC.

As the distance between the control PC and the AP could be more than 100 meters, a baud-rate equal to 1200 bps has been chosen accordingly to Texas Instruments specification. Moreover to increase the robustness of the communication and external noise immunity a category-6 UTP cable has been chosen, since sensors will be installed outdoor.

7.1.3 Ad-hoc communication protocol

As the wireless communication between nodes is based on packets exchange it is necessary to describe the packets structure before explaining the ad-hoc communication protocol.

For toughness reasons a single packet type has been used in the network protocol. The packet structure is reported in **Table 7.1** with the size of each field.

Table 7.1. WSN packet structure.

Rec. Address	Sender Address	Status Byte	CRC1	CRC2
1 byte	1 byte	1 byte	1 byte	1 byte

The field *Rec. Address* contains the recipient address while the field *Sender Address* contains the information about the board which sends the packet. CRC1 and CRC2 are two fields automatically inserted by the radio transceiver in order to improve the communication performances: they allow to detect transmission errors which might always occur.

Three different values can be contained inside the field *Status Byte* and identify the type of a certain packet:

- ‘R’ value: it stands for a status request packet;
- ‘O’ value: it stands for an acknowledgment (ACK) packet;
- ‘A’ value: it stands for an alarm packet.

The master node queries each slave node every 8 seconds and send the received information to the embedded PC via serial interface. The transmission of a single packet between the AP and a slave node lasts about 8.3 ms, a negligible time compared to the time interval needed to complete an interrogation to a board.

A protocol transaction starts with a R packet sent by the AP. The interrogated slave node must answer within a timeout limit of 10 seconds. If within that time no response is received by the AP, no string is sent to the embedded PC where the serial data processing software (see paragraph 6 for details) will detect a possible alarm warning. If AP receives an O packet coming from the interrogated slave node it continues to query the other WSN boards until a complete interrogation cycle is performed (**Figure 7.**). At the end of each complete cycle a special string, containing the message “AP_ONLINE” is then sent to the control PC by the AP in order to report the regular WSN working.

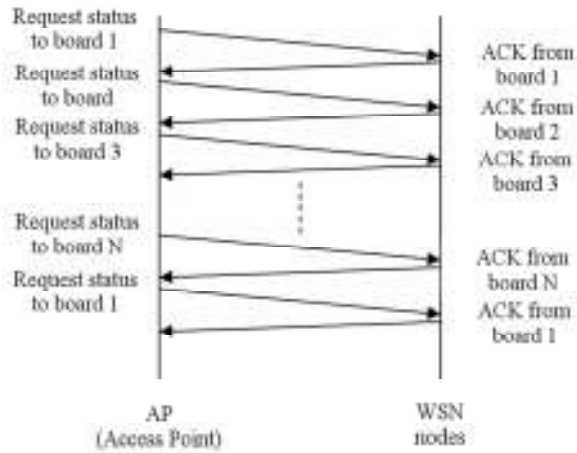


Figure 7.2. Example of a protocol transaction without alarm detection.

If one of the slave nodes detects an alarm, an A packet is sent immediately to the AP which interrupts the normal interrogation cycle and forward the alarm information to the control PC. The A packets are continuously sent by the node until a restart operation of the entire WSN is performed (Error! Reference source not found.).

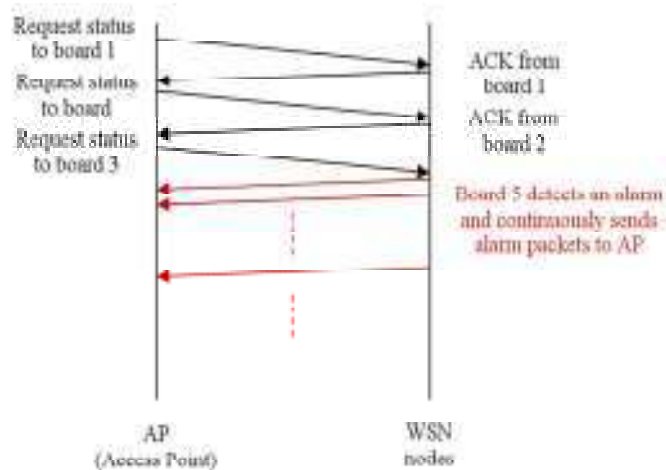


Figure 7.3. Example of a protocol transaction when a board detects an alarm.

7.1.4 Alarm detection procedure

A possible alarm event is triggered when a 5 degrees tilt variation is detected by a sensor board in at least one of the three coordinate directions. The alarm detection is performed directly by the firmware on each slave node. It has to be noted that the firmware for the slave nodes (exactly as well as the one for the AP) has been entirely developed ad-hoc for this WSN.

The slave nodes firmware has been developed to monitor PV panels position. As soon as the WSN is turned on each node acquires data from the three axis accelerometer for 30 seconds in order to establish with sufficient precision the operating position of the panel. At the end of this “learning phase” the proper processing of the accelerometer signals starts, in order to reveal potential alarms.

During the WSN normal working the accelerometer sampling frequency is equal to 100 Hz so it possible to immediately detect an alarm when a panel is moved from its steady position. To avoid false alarms due to accidental movements (e.g. vibrations due to the transit of heavy vehicles near the PV system) a time variant median filter has also been implemented.

The alarms detection is made by comparison between the values acquired by the accelerometer during the “learning phase” and the filtered instantaneous values. If the difference is greater than a well defined threshold (which corresponds to a 5 degree displacement) an alarm is detected and the A packet is immediately sent to the AP.

7.1.5 Processing software on the control PC

The processing software runs on the embedded control PC which is equipped with a Linux Operative System (at the moment, Debian 6.0 distribution) in order to reduce the WSN costs.

The software analyzes the data coming from the serial port of the PC where the WSN master node is connected.

The processing software is structured into two phases: “learning” and “running”. *Learning* operations are performed at each software start up and allow to learn the status of all the WSN boards when the power is turned on. The *running* phase works on the

basis of information acquired during the *learning* phase and runs until the PC is shut down or an alarm event is triggered. It records all the WSN information in some appropriate log files and once a day transfers them to the remote server to keep an historical archive of network behaviors.

In case of alarm detection, the software immediately activates the communication with the remote server, sends the emails to a list of preconfigured addresses, turns on the relay for the sound-light signaling device, and connects to a dedicated FTP server which provide for a service that sends SMS messages. Each WSN monitoring operation in progress is stopped in order to perform a sudden communication of the alarm. Four distinct alarm events can be triggered by the software on the control PC:

1. Receipt of an A packet. It means that a sensor sends a packet which contains an alarm detection corresponding to a possible movement of a PV panel from its steady position (see paragraph 5).
2. Receipt of wrong strings on the serial port. It means that the communication between master node, embedded PC and slave nodes is compromised. Some possible reasons could be board damages or even intentional jamming.
3. Lack of packets reception coming from a certain slave node. It means that such sensor was disconnected from the power supply or have been damaged.
4. Expiration of the serial port timeout; the software listens to serial port and if it does not receive data within a certain time interval (defined in the software settings) an alarm event is triggered. That is because the lack of data reception may be due to an intentional interruption of the serial cable.

Since it is necessary that the WSN is connected to internet with a GPRS modem to transfer file between control PC and remote server, to send e-mail and to connect to the FTP server for SMS, and to perform management operations, it is important to monitor the internet connectivity. This operation is executed by a script running on the server, which periodically ping the GPRS modem. If the WSN does not appear online for more than 2 consecutive interrogations a further alarm event is triggered by the

remote server. In this case no sound-light communication is turned on but only email and SMS are sent.

7.1.6 Sensors calibration

The alarm detection is made through the identification of a tilt variation of the panel strictly greater than 5 degrees on at least one of the three axis from its steady position. Sensors sensitivity and offset values are needed to evaluate the right acceleration values and the corresponding position. Datasheets report such nominal values but they are subject to slight variations within a tolerance interval. Hence to establish a correspondence between the accelerometers values (expressed in g acceleration) and the corresponding angular variation, an offline calibration procedure was performed.

Before calibrating all the sensors used in the WSN a particular firmware has been written to acquire data from the sensor boards without transmit any packet to the master node. The board is then forced to transmit all the acceleration measured values directly to a specific PC of the laboratory, used only for calibration (it has to be noted that only for debug and test purposes all the boards have been equipped with RS-232 interface, exactly as well as the master node which use such connection also to communicate with the control PC).

Two calibration algorithms have been investigated and implemented: the first proposed by P. Lukowicz et. al.⁵ and the second by I. Frosio et. al.⁶. Both algorithm give as output the offset and the sensitivity of a MEMS accelerometer sensor in each of the three direction. These values have been used to compute the angular position of a board in term tilt value.

A test board has been used to establish which one was the most useful for the sensors employed in the WSN. A large number of measure has been made for each algorithm and the results are reported in **Table 7.2** and

⁵P. Lukowicz, H. Junker, G. Troester, *Automatic calibration of body worn acceleration sensors*, Pervasive Computing, Vol. 3001/2004, pp. 176 – 181, 2004.

⁶I. Frosio, F. Pedersini, N. A. Borghese, *Autocalibration of MEMS Accelerometers*, IEEE Transaction on instrumentation and measurement, Vol. 58, N. 6, pp 2034 – 2041, 2009.

Table 7.3.

Lukowicz algorithm shows that the board is able to measure a tilt with less than 3 degrees accuracy, while using the Frosio one the accuracy for tilt measurement is less than 1.5 degrees. Hence the second algorithm has been chosen.

Each sensor board has been calibrated in the laboratory workbench before its installation in the anti-theft alarm system.

Table 7.2. Calibration procedure results for a test board: offset values.

	Nominal datasheet value	P. Lukowicz proposed algorithm	I. Frosio proposed algorithm
X offset	1.5	$1.4312 \pm 6 \cdot 10^{-4}$	$1.4285 \pm 5 \cdot 10^{-4}$
Y offset	1.5	$1.4686 \pm 4 \cdot 10^{-4}$	$1.4665 \pm 4 \cdot 10^{-4}$
Z offset	1.5	$1.4372 \pm 9 \cdot 10^{-4}$	$1.4370 \pm 7 \cdot 10^{-4}$

Table 7.3. Calibration procedure results for a test board: sensitivity values.

	Nominal datasheet value	P. Lukowicz proposed algorithm	I. Frosio proposed algorithm
X sensitivity	0.42	$0.4143 \pm 7 \cdot 10^{-4}$	$0.4100 \pm 9 \cdot 10^{-4}$
Y sensitivity	0.42	$0.4163 \pm 11 \cdot 10^{-4}$	$0.4235 \pm 5 \cdot 10^{-4}$
Z sensitivity	0.42	$0.4116 \pm 6 \cdot 10^{-4}$	$0.4120 \pm 7 \cdot 10^{-4}$

7.2 WSN for smart gas metering⁷

The Smart Grids, which are particular WSNs devoted to energy management, are emerging as a convergence of information technology and communication technology with power system engineering and metering technologies. A more detailed definition can explain better what are the “Smart Grid” today emphasizing their relevance. They can be defined as networks that can intelligently integrate the actions of all users connected to them using digital technologies. Basically their goal is a modernization of

⁷The described work about the WSN for smart gas metering, has been published as follow: O. Rorato, S. Bertoldo, C. Lucianaz, M. Allegretti, S. Bertoldo, R. Notarpietro *An Ad-Hoc Low Cost Wireless Sensor Network for Smart Gas Metering.*, Wireless Sensor Network, vol. 5, N. 3, pp. 61-66, 2013

already existing energy grids with ICT technologies, joining power-delivery systems and customers, and allowing a two-way communication between them. A paper of Panajotovic et. al.⁸, presents a very detailed description of the state of the art of the smart grid and their close relationship with ICT.

The Smart Grids will have a key role in the transformation of the current functionality of the energy distribution system, aiming both to offer a user-oriented service and to help energy distribution companies. They will help European countries to achieve the so called objectives "20/20/20" (Horizon 2020) the next European framework program for research and innovation.

It has to be noted that a Smart Grid should be able to provide one or more of the following new capabilities: self-healing, high reliability, energy management, and real-time pricing for every kind of energy sources [7]. Therefore, from a design perspective, a smart grids will incorporate new technologies as advanced metering, automation, communication, distributed generation, and distributed storage.

Usually the words "Smart Grid" are referred to the electrical distribution systems because the grids usually have strict power requirements. By using more modern technologies for WSN it is also possible to implement Smart Grids for different energy sources such as the gas energy.

A new experimental and prototypal Wireless Sensor Network has been completely designed, realized and tested as an ad-hoc smart grid for gas metering able to give to gas operators a simple and cheap tool to keep under control the costumers gas consumption.

7.2.1 General description of the grid for smart gas metering

The smart grid for gas metering has been designed with a master-slave architecture and star topology. A central node, called Master Node or Access Point (AP), receives data coming from all the peripheral nodes and dialogues with an embedded control PC. It has

⁸ B. Panajotovic, M. Jankovic, Odadzic, B, *ICT and smart grid*, 10th International Conference on Telecommunication in Modern Satellite Cable and Broadcasting Services (TELSIKS), 5-8 Oct. 2011, pp. 118-12.

to be noted that each slave nodes communicates only with the master node with a unidirectional link.

The control PC is a common commercial embedded PC which can be connected to internet using either a GPRS router or a wired internet connection. It allows both locally and remotely authorized users (e.g. the gas company which delivers the service) to control the gas consumption. Moreover the PC stores all the data coming from the sensor node in a dedicated database and can send SMS and e-mail alerts, if such functionalities are turned on. Both the control PC and AP node are connected to power lines because of their high computational load.

Each slave node is directly connected to a gas meter equipment, which is almost never connected to power lines. To ensure a life period of almost 10 years (avoiding a too frequent battery replacements by maintenance workers), the nodes' electronics have been designed to have an almost irrelevant current consumption and they can be fed up by a common 3.6 V lithium battery.

The sensor node has been designed in order to receive information coming from a commercial pulse transmitter. It is connected to a common commercial gas meter in order to count the pulses detected by its reed relay switch. In fact, even if some high resolution electronic gas meter systems have been experimentally realized, most gas meters used for residential purposes are still using mechanical diaphragms technology connected to reed pulse gas meter. The number of counted pulses are sent to the AP using the standard Wireless M-BUS protocol⁹. Knowing the correspondence between a single count and the gas consumption it will be possible to evaluate the gas consumption by each meter installed by the customers.

7.2.2 Sensor node description

The sensor node (**Figure 7.4**) is developed to perform the following tasks:

- Reading pulses from gas meter equipments;

⁹ N. Anglani, E. Bassi, F. Benzi, L. Frosini, T. Traino, *Energy smart meters integration in favor of the end user*, IEEE International Conference on Smart Measurements for Future Grids (*SMFG*), 14-16 Nov. 2011, pp.16-21

- Storing the temporary number of counted pulses on local memory waiting to send to the AP;
- Managing Wireless Meter Bus protocol for download data to the AP;
- Error handling.

The system on chip (SoC) used for the node of the smart grid is the Texas Instruments CC430F5135: it integrates in a single solution both the microcontroller and the radio, thus reducing costs and power consumption. The radio can operate in different frequency bands (300 - 348 MHz, 389 - 464 MHz, 779 - 928 MHz) with very little firmware and hardware modifications. The developed smart grid prototype operates a 868 MHz.



Figure 7.4. Realized electronic board for gas smart grid nodes.

The board power consumption depends on the chosen operating modes. In particular it is very sensitive to the selected output power (up to a maximum of 10 dBm) which cause a consumption to a few tens of milli-Amperes. In the described prototype, low power firmware techniques have been adopted in order to properly managed the board, reducing the power consumption, keeping the microcontroller in the so called “Low Power Mode” as long as possible, since in that condition the amount of absorbed current is equal to a few micro-Amperes. It is possible to achieve a theoretical durations of 10 years using commercial standard lithium batteries of 3.6 V.

7.2.3 Reading pulses from gas meter equipments

The electronic boards for the described smart grid have been completely designed: they have two interfaces to manage both open collector output than reed relay switches. For the smart grid, only the second interface has been used. (**Figure 7.5**).

The microcontroller acquires the pulse thanks to the right setting of the dedicated pin. The pulse trigger a software interrupt able to update the pulse count.



Figure 7.5. Example of common gas metering system. The black box is the commercial pulse transmitter which is connected to the sensor board of the smart grid shown in Figure 7.4.

7.2.4 Storing pulse on local memory

The pulses read by the electronic board are stored on the local flash memory of the microcontroller waiting to be send to the AP. The available memory size is enough for the purposes of the described smart grid.

7.2.5 The communication protocol

A detailed description of the wireless metering protocol state of art is reported in the scientific literature. Anyway the Meter Bus (M-BUS) protocol and the wireless version (Wireless M-BUS or WM-BUS) are the “de-facto” standard for all the smart metering grid.

The M-BUS protocol is the most common standard used for the so called Automatic Meter Reading (AMR) implementation, very useful for remote energy meter reading. It

is based on European standard EN 13757-2 (for physical and link layers) and EN 13757-3 (for application layer). The M-BUS can be used in different topologies of smart grids, including the star topology used for the presented network. When interrogated, the meter nodes (the slave nodes) send the data to a concentrator (the master node devoted to receive and manage data from each slave node) that can be also remotely placed if an internet connection is available.

The WM-BUS standard is another European standard defined in EN 13757-4 (for physical and data link layers) and in EN 13757-3 (for the application layer). It defines different possibilities of communication between remote meters and mobile devices, stationary receivers, and data collectors and storage devices¹⁰.

The WM-BUS standard is designed to give a long battery life for grid nodes powered with batteries, to avoid often battery replacements during the normal life time of a network node. Moreover it has to be noted that the presented smart grid for gas metering does not require the complete version of the WM-BUS protocol which has more complete and complex features¹¹. It is sufficient a limited version which is currently in use in a lot of experimental and prototypal grids and which can be freely downloaded from the web. It is only necessary to adapt such protocol to the system on chip used in the custom realized electronic boards, thus reducing the realization costs of the WSN.

Among the different modes available with WM-BUS protocol, the described network uses the Stationary Mode (S-Mode), which allows an unidirectional link between meter nodes and the AP. It is in fact only necessary that each sensor node sends its data to the central node, without waiting any acknowledgement answer.

The S-Mode defines a radio link type with the following characteristics:

- Manchester data coding;
- 32.768 kbaud typical;

¹⁰ K. Hariharasudhan, F. Colaianni, M. Sardo, S. Ramkumar, N. Kochhar, *Wireless M-Bus In Smart Grid Scenario*, Arrow Electronics.

¹¹ A. Sikora, D. Lill, *Design, Simulation, and Verification Techniques for Highly Portable and Flexible Wireless M-Bus Protocol Stacks*, International Journal of Smart Grid and Clean Energy, Vol. 1, No. 1, 2012, pp. 97-102

- 868 MHz \pm 100 kHz as operational frequency;
- typical receiver sensitivity of -105 dBm to ensure a BER of 10^{-2} .

All the described characteristics, including the packet length, suit very well with the proposed WSN solution for smart gas metering.

To handle the WM-BUS protocol, dedicated firmware functions have been developed and integrated on the microcontroller. A proprietary algorithm, based on the approach “listen before talk”, has been developed to manage and avoid the collision when more than one node want to transmits at the same time.

7.2.6 Error handling

The electronic board of each sensor node is able to handle any failure such as low battery, possible short-circuits on reading pin, quartz and clock problems. Its firmware is realized to switch on a specific led for different error or malfunctioning, and to stop sending data to the AP in case of failure. An authorized user connected to the smart grid web interface, or whose e-mail address or phone number is part of the list at which the AP sends e-mails and SMS, can thus note that a specific node is no longer active, and can program a maintenance field intervention in order to repair or substitute the damaged node. The specific failure is identified by the corresponding led turned on without performing difficult tests.

7.2.7 Central node description

The central node is made up by the Access Point (AP) node, which is directly connected to the embedded PC. The communication between the AP and the embedded PC is performed through the standard RS-232.

7.2.7.1 The Access Point node

To further reduce the production costs of the electronic boards, the hardware of the AP electronic board is the same of the one adopted for the meter nodes. In fact, even if the AP is the only node which uses the RS-232 standard, the interface has been placed on

all the node to serialize the board production. It possible to substitute each node of the smart grid with another by only modifying the firmware.

The AP receives WM-BUS packets coming from each nodes and forwards each packets to the embedded PC.

7.2.7.2 The embedded PC

The embedded PC performs four basic functions:

- reception of the information acquired from the AP;
- storage of node values in a coherent database, thus providing a database server;
- representation of the network status on the web interface, thus providing a web server.
- sending e-mails and SMS alerts if the dedicated functionalities are active.

All the functions are performed simultaneously while the PC is connected to internet through a GPRS router or a wired connection, if available.

The PC is equipped only with open source software and a LAMP platform is installed on it, in order to create an easy to use system, compliant with international standards. The LAMP platform includes Linux (Debian 6.0) as operative system, Apache as web server, MySQL as database server and PHP as scripting and programming language. This is one of the most globally used framework and allow the prototypal grid to be a base for a future more complex system development.

The reception of the information on RS-232 interface is managed by an ad-hoc developed C software which stores the read values coming from each node in the database. It uses open source libraries and checks if a node is still connected to the smart grid (a node is assumed to be disconnected or not active if does not transmit any data for 10 minutes). The same software creates a specific log file which allows to control the correct functioning of the network and the correct reception of the packet coming from the AP.

The web interface has been realized using both HTML and PHP languages. It is accessible only after an authentication procedure, and it is made up by two sections. The main section shows the last read values coming from each node, with the corresponding

timestamp, while a graphical indicator shows if a node is still active and connected to the smart grid (**Figure 7.6**). The second section shows the last 10 rows of the log file and allows to have an immediate indication in case of network problems (**Figure 7.7**).

Node	Date and Time	Value	Node Active
1	2012-11-23 15:00:21	2448	
2	2012-11-23 15:00:38	2456	
3	2012-11-23 15:00:25	1345	
4	2012-11-23 15:00:17	912	
5	2012-11-23 14:50:21	1927	

Figure 7.6. Example of web interface. It reports the information about each network node. In the reported situation node 5 is no longer connected to the smart grid.

LOG FILE

Wed Oct 31 16:06:57 2012 : Error during insert in db
 Wed Oct 31 16:07:29 2012 : Error during insert in db
 Wed Oct 31 16:08:01 2012 : Error during insert in db
 Mon Nov 5 12:19:15 2012 : Starting logger
 Mon Nov 5 12:19:15 2012 : Serial port connection open

Figure 7.7. Example of web interface. It reports the last information reported in the log file.

If a node becomes disconnected from the smart grid or some problems occur, e-mail or SMS alerts are also sent by the AP to a list of selected addresses or phone numbers. Such functionalities can be turned on or off using a configuration file editable by authorized users.

The database is made up by two tables: the first contains the information related to the smart grid nodes and the second contains the data related to the pulse detected by each sensor node and sent through radio channel to the central node (**Figure 7.8** shows the implemented structure).

The tables respect the referential integrity constraint. If a node is connected for the first time to the grid its insertion into the database is managed by well designed store procedures and triggers. Such triggers are activated before the record containing the data read by the node is stored into the right table of the database. It is thus possible to avoid writing specific C procedures to add a new node in the database, making the entire database more robust and efficient.

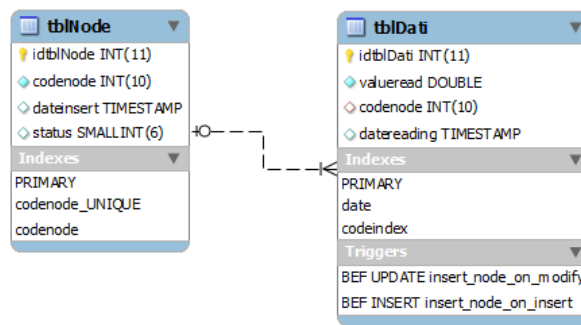


Figure 7.8. Entity-Relationship scheme for central node database.

7.2.8 Test results

A first experimental smart grid for gas metering, made by one AP connected to the embedded PC and 5 sensor nodes, have been tested in the laboratory achieving very good results. The WSN has proven to be “self-learning”, and each new node connected to smart grid has been correctly recognized and added into the database as soon as it has been turned on.

A massive stress test have been performed by connecting each sensor node to a tool able to simulate the pulses coming from the commercial pulse generator connected to the gas meter (**Figure 7.9**). The sampling time has been set to 1 minute, in order to have a large amount of data to be stored on the embedded PC of the central node. The simulated network has been kept “operational” for almost 14 consecutive days. Each

node sent to the AP an average of 18600 values (out of the theoretically expected 20152). Details about data transmitted by each node and correctly managed by the simulated network are shown in **Table 7.4**.

Sampling interval equal to 1 minute is definitely excessive in a real context of application of the smart grid for smart gas metering. It is more likely that each grid node will perform a sampling operation 4 times per day in order to allow the AP to receive 1460 packets per year. With 20152 packets received at the end of the test, a period of activity of the entire smart grid equal approximately to 14 years (actually 13.8 years) was estimated.



Figure 7.9. Smart grid node during the massive stress test connected to commercial pulse generator which will be connected to the gas meter in a real application.

Experimental current consumption was very low in 4 out of 5 test nodes, in accordance to datasheet information, allowing a life period of each node of almost 10 years, as decided in designing stage. The higher current absorption of the fifth node is due to imperfections in the realization of electronic boards (e.g. not perfect components welding).

Table 7.4. Percentage of correctly received packets from each node and managed by the entire smart.

	Received packets	Percentage of correctly received packet
Node 1	18801	94%
Node 2	18716	93%
Node 3	18878	94%
Node 4	17748	88%
Node 5	18862	94%
SMART GRID	93005	92%

7.2.9 Simulation of the network operational behavior

In the following a simulation of the network proper functioning is reported. The initial situation was with the entire network off, and the nodes' database completely empty. The access point has been turned on, and all the nodes were identified when they become operative. Moreover a situation where a node is disconnected from the WSN is simulated. The following Table 7.5 reports the actions performed during the simulation and the corresponding web page containing the situation of the network (the read value in this simulation is temperature, while in the fully operative network will be the gas consumption, as reported before).

Table 7.5. Actions performed during the simulation of the WSN operational behavior.

1) Access Point is turned on (AP)



The screenshot shows the 'Piceno GAS' web interface. At the top, there is a logo for 'CINFAL' and 'Piceno GAS'. Below the logo, the text 'DATI DAI SENSORI' is displayed in red. Underneath, it says 'Ultimo aggiornamento: 23 Nov 12 - 14:19:45'. A table with the following headers is shown: 'NODO', 'ULTIMA LETTURA', 'VALORE', and 'NODO ATTIVO'. The table is currently empty.

2) Node n° 3 is turned on and immediately identified by AP



The screenshot shows the 'Piceno GAS' web interface. At the top, there is a logo for 'CINFAL' and 'Piceno GAS'. Below the logo, the text 'DATI DAI SENSORI' is displayed in red. Underneath, it says 'Ultimo aggiornamento: 23 Nov 12 - 14:24:17'. A table with the following headers is shown: 'NODO', 'ULTIMA LETTURA', 'VALORE', and 'NODO ATTIVO'. The table contains one row of data:

NODO	ULTIMA LETTURA	VALORE	NODO ATTIVO
3	2012-11-23 14:24:08	22.059999	

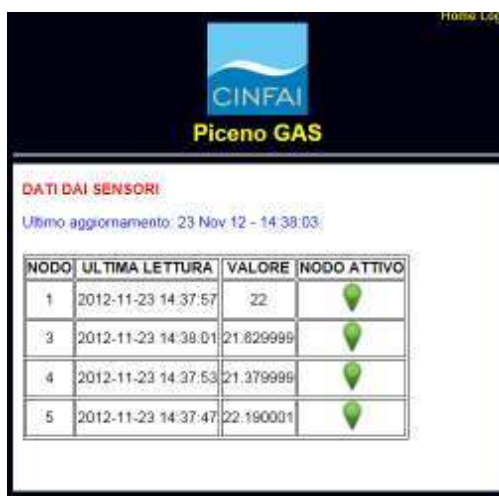
4) Node n° 1 and node n° 4 are turned on and immediately identified by AP



The screenshot shows the 'Piceno GAS' monitoring interface. At the top, there is a logo for 'CINFAI' and the text 'Piceno GAS'. Below this, the section is titled 'DATI DAI SENSORI' with a subtitle 'Ultimo aggiornamento: 23 Nov 12 - 14:32:00'. A table displays the following data:

NODO	ULTIMA LETTURA	VALORE	NODO ATTIVO
1	2012-11-23 14:31:30	22.129999	●
3	2012-11-23 14:31:34	21.809999	●
4	2012-11-23 14:30:25	21.5	●

5) Node n° 5 is turned on and immediately identified by AP



The screenshot shows the 'Piceno GAS' monitoring interface. At the top, there is a logo for 'CINFAI' and the text 'Piceno GAS'. Below this, the section is titled 'DATI DAI SENSORI' with a subtitle 'Ultimo aggiornamento: 23 Nov 12 - 14:38:03'. A table displays the following data:

NODO	ULTIMA LETTURA	VALORE	NODO ATTIVO
1	2012-11-23 14:37:57	22	●
3	2012-11-23 14:38:01	21.829999	●
4	2012-11-23 14:37:53	21.379999	●
5	2012-11-23 14:37:47	22.190001	●

5) Node n° 5 is turned off

6) Node n° 2 is turned on and immediately identified by AP



The screenshot shows the 'Piceno GAS' monitoring interface. At the top, there is a logo for 'CINFAI' and the text 'Piceno GAS'. Below this, the section 'DATI DAI SENSORI' is displayed, along with the last update time: 'Ultimo aggiornamento: 23 Nov 12 - 14:54:49'. A table with four columns: 'NODO', 'ULTIMA LETTURA', 'VALORE', and 'NODO ATTIVO' is shown. Node 2 is highlighted with a green dot, indicating it is active.

NODO	ULTIMA LETTURA	VALORE	NODO ATTIVO
1	2012-11-23 14:54:29	21.809999	●
2	2012-11-23 14:54:45	22.25	●
3	2012-11-23 14:54:33	21.5	●
4	2012-11-23 14:54:25	21.190001	●
5	2012-11-23 14:50:21	21.809999	●

7) After 10 minutes it is communicated that node n° 5 is disconnected from the network.



The screenshot shows the 'Piceno GAS' monitoring interface after 10 minutes. The last update time is now 'Ultimo aggiornamento: 23 Nov 12 - 15:00:40'. The table shows that Node 5 is now disconnected, indicated by a red dot in the 'NODO ATTIVO' column.

NODO	ULTIMA LETTURA	VALORE	NODO ATTIVO
1	2012-11-23 15:00:21	21.75	●
2	2012-11-23 15:00:38	21.5	●
3	2012-11-23 15:00:25	21.440001	●
4	2012-11-23 15:00:17	21.129999	●
5	2012-11-23 14:50:21	21.809999	●

8) Node n° 5 is turned on another time and immediately identified by AP



Home Log

CINFAI
Piceno GAS

DATI DAI SENSORI
Ultimo aggiornamento: 23 Nov 12 - 15:09:52

NODO	ULTIMA LETTURA	VALORE	NODO ATTIVO
1	2012-11-23 15:09:25	21.690001	●
2	2012-11-23 15:08:40	21.190001	●
3	2012-11-23 15:08:29	21.309999	●
4	2012-11-23 15:08:21	21.063	●
5	2012-11-23 15:08:34	21.559999	●

9) All the nodes are operative

Bibliography

- Atlas D., *Radar in meteorology*, American Meteorological Society, 1990.
- Battan L. J., *Radar Observation of the atmosphere*, University of Chicago Press, Chicago, 1973.
- Collier C. G., Chapuis M., *Weather Radar Networking*, Kluwer Academic Publishers, 1990.
- Collier C. G., *Applications of weather radar systems: a guide to uses of radar data in meteorology and hydrology*, Ellis Horwood, 1989.
- Rorato O., *Studio e progettazione di sistemi elettronici per monitoraggio ambientale*, Politecnico di Torino, Torino, 2012.
- Sauvageot H., *Radar Meteorology*, Artech House 1992.

All the papers cited in each chapter of the Thesis.